Universitat Autònoma de Barcelona

Centre Nacional de Microelectrònica IMB

Hybrid integration of MEMS technology and rapid - prototyping techniques: Design, fabrication and characterization of electrochemical devices and miniaturized microbial fuel cells.

Doctoral thesis dissertation submitted by David Sánchez Molas
to apply for the doctoral degree of electronic engineering

Dr. Francesc Xavier Muñoz Pascual and Dr. Francisco Javier del Campo García as thesis directors, and also Dr. Arantxa Uranga del Monte as thesis tutor certify that the thesis entitled: *Hybrid integration of MEMS technology and rapid - prototyping techniques: Design, fabrication and characterization of electrochemical devices and miniaturized microbial fuel cells* has been carried out by David Sánchez Molas at the Institute for Microelectronics of Barcelona (IMB-CNM, CSIC) under their supervision to apply for the degree of Doctor of Electronic Engineering at Universitat Autònoma de Barcelona.

Bellaterra, 2013.

Dr. Francesc Xavier Muñoz Pascual	Dr. Francisco Javier del Campo García	Dr. Arantxa Uranga del Monte	David Sánchez Molas

Contents

List of figures

List of tables

Symbols and abbreviatons

Table 1. List of symbols.

Symbol	Meaning	Units
A	Electrode area.	m^2
A_{dd}	Single domain area.	m^2
C_x	Concentration of the electroactive species.	mol
d	Distance between micropillar centers.	m
D_x	Diffussion coeficient.	$m^2 \cdot s^{-1}$
F	Faraday constant.	96485 $C \cdot mol^{-1}$
$h_{\mu Pill}$	Micropillar height.	m
i	Current.	A
i_p	Peak current.	A
j	Current density.	$A \cdot m^{-2}$
j_p	Peak current density.	$A \cdot m^{-2}$
k^o	Electron transfer rate constant.	$m \cdot s^{-1}$
m_T	Mass transport coefficient.	$m \cdot s^{-1}$
n	Number of electrons.	-
P	Electric power.	W
r_d	Micropillar radius domain.	m
$r_{\mu Pill}$	Micropillar radius.	m
R	Dimensionless micropillar radius domain.	-
R’	Ideal gas constant.	8.31 $J \cdot K^{-1} \cdot mol^{-1}$
t	Time.	s
T	Absolute temperature.	K
Z	Dimensionless micropillar height.	-
α	Charge transfer coefficient.	-
ΔE_p	Peak-to-peak potential separation.	V
υ	Scan rate.	$V \cdot s^{-1}$

Table 2. List of abbreviations.

Abbreviaton	Meaning
AMMT	Advanced MicroMachining Tools.
CAD	Computer Aided Design.
CNC	Computer Numerical Control.
CV	Cyclic Voltammetry.
CVD	Chemical Vapor Deposition.
DO	Dissolved Oxygen.
DOF	Degrees Of Freedom.
DRIE	Deep Reactive Ion Etching.
FC	Fuel Cell.
FEM	Finite Element Method.
FIB	Focused Ion Beam.
GC	Glassy Carbon.
GPIB	General Purpose Interface Bus.
HAR	High Aspect Ratio.
HOMO	Highest Occupied Molecular Orbital.
IMB - CNM	Instituto de Microelectrónica de Barcelona – Centro Nacional de Microelectrónica.
IC	Integrated Circuit.
LPCVD	Low Pressure Chemical Vapor Deposition.
LUMO	Lowest Unoccupied Molecular Orbital.
MEMS	MicroElectroMechanical Systems.
MFC	Microbial Fuel Cell.
MED	Mediator.
OCV	Open Circuit Voltage.
PECVD	Plasma Enhanced Chemical Vapor Deposition.
PEM	Polymer Elecrolyte Membrane .
PEMFC	Polymer Elecrolyte Membrane Fuel Cell.
PDE	Partial Differential Equation.
PDMS	Polydimethylsiloxane.
PMMA	Polymethylmethacrylate.
PPF	Pyrolyzed Photoresist Film.
ppb	One part per billion.
PSA	Pressure Sensitive Adhesive.
PVD	Physical Vapor Deposition.
RCA	Radio Corporation America.
RTP	Rapid Thermal Process.
SEM	Scanning Electron Microscope.

SWV	Square Wave Voltammetry.
TEA	Terminal Electron Acceptor.
TUB	Technische Universität Braunschweig.
UAB	Universitat Autònoma de Barcelona.
UV	UltraViolet.
WHO	World Health Organization.
WWF	World Wide Fund for Nature.

Motivation and objectives

The aim of this thesis is to improve the performance of miniaturized electrochemical devices, with an emphasis on microbial fuel cells and electrochemical sensors. To achieve this goal, this thesis focuses on the development of new electrode materials, new microelectrode geometries, and better fabrication and packaging processes. Design and fabrication tasks have involved diverse and multidisciplinary branches of science and technology such as silicon microfabrication, finite element simulations, rapid-prototyping techniques and electrochemical and bioelectrochemical characterization. Also collaborations with other academic institutions have been necessary for the success of this work.

An important drawback in the miniaturization of electrochemical devices lies in that the reduction of the active area of the electrodes results in smaller signals. On the other hand the choice of materials for a specific application poses further issues because incompatibilities between materials and/or the required experimental methods may exist. However, the introduction of silicon micromachining techniques such as photolithography, wet and dry etching, metal or dielectric coating by physical and chemical deposition or rapid thermal processes has become a realistic way to solve most problems facing the manufacturing of miniaturized electrochemical devices.

In addition to microfabrication, the use of computational tools based on finite element methods has helped extraordinarily in the design of these devices because both electrode kinetics and mass transport can be simulated and studied prior to fabrication. Moreover, the availability of commercial finite element method software has made it easier to develop electrochemical models because the boundary conditions and the most important expressions describing the main electrochemical phenomena may already be defined in modern commercial Finite Element Method (FEM) software.

This thesis covers several fields of science and technology, and it is divided in three parts containing a total of 4 chapters. The overall organization of this thesis is represented in Figure 1.

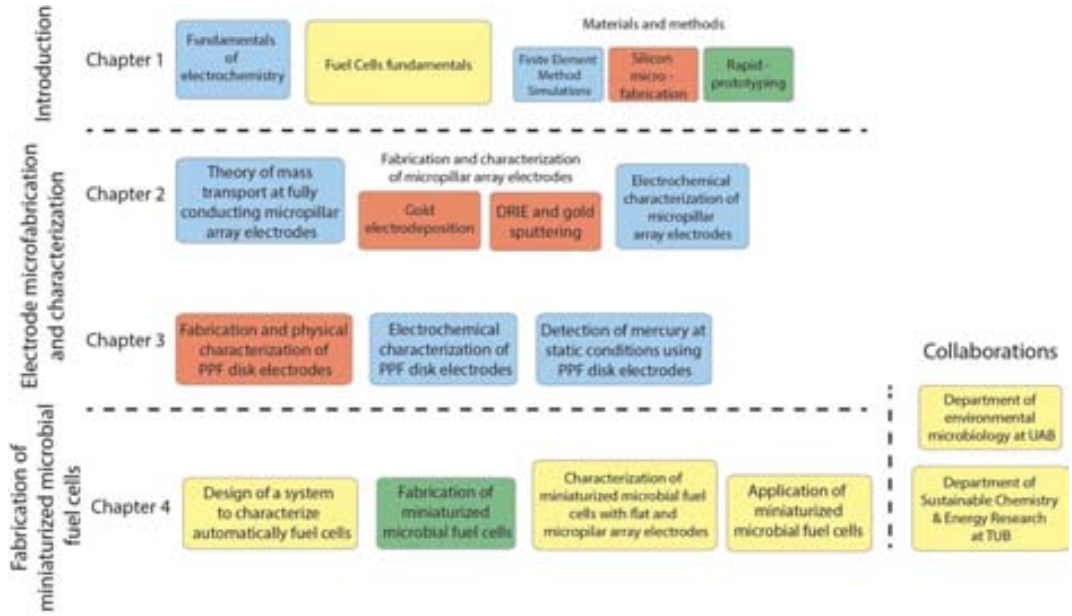

Figure 1. Graphic summary of this thesis.

Part one: Introduction

The first chapter is divided in three sections and covers the fundamentals of electrochemistry, design, fabrication and applications studied during this thesis. The first section explains three fundamental aspects of electrochemistry; they are electrode kinetics, mass transport phenomena and instrumental methods. The second section introduces fuel cells because this is the electrochemical device developed in chapter 4. Finally the last section covers the materials and methods used, including the microfabrication of the electrodes featured in chapters 2 and 3, and also the prototyping techniques used to fabricate the fuel cells presented in chapter 4.

Part two: Electrode microfabrication and characterization

Chapter two focuses on the development of fully-coducting micropillar array electrodes. The chapter begins with the theory of mass transport at fully-conducting micropillars. Following this, the computational model of a single domain of a fully-conducting micropillar is developed using COMSOL Multyphisics. This provides insights to the behavior of these structures prior to fabrication, which is tackled next. The fabrication of fully-conducting micropillar array electrodes was achieved by gold electrodeposition and also by a combination of dry etching and sputtered gold deposition. The chapter closes with the electrochemical characterization of both arrays, which allowed us to compare their response and found out which route was better.

Chapter three addresses the synthesis of Pyrolyzed Photoresist Films (PPF), and the fabrication of carbon disk electrodes to detect mercury in aqueous samples. The fabrication

of these electrodes combines photolithograpy and a rapid thermal process. Besides the active window of these electrodes was defined by the chemical deposition of dielectric layers, also the electrodes were physically and electrochemically characterized. Once these electrodes were completely studied they were used to detect mercury in a stagnant solution.

Part three: Fabrication of miniaturized microbial fuel cells

The last chapter focuses on finding an application for the fully-conducting micropillar array electrodes described in chapter 2. The application chosen was a miniaturized microbial fuel cell fabricated by rapid-prototyping techniques. Several miniaturized microbial fuel cells were fabricated using in each case a different geometry with the aim of find out if the use of micropillar array helps to improve the electrical performance of microbial fuel cells. In addition two collaborations were established before starting to develop these chapters. The first collaboration was with Professor Uwe Schröder who leads the sustainable chemistry & energy research group at Technische Universtität Braunschweig in Germany. Here, micropillar array electrodes were used to study the suitability of these micropatterned electrodes in microbial fuel cells. The second collaboration was with the department of environmental microbiology at Universitat Autònoma de Barcelona under the supervision of Professor Jordi Mas. Here a system to automatically characterize fuel cells was developed using Labview. Also, all the experiments on miniaturized microbial fuel cells were carried out in Professor Mas' laboratory.

Chapter 1. Introduction

This introduction aims to provide a broad overview of the fundamental principles of electrochemistry, the devices developed for this thesis and their applications, and finally the design and fabrication techniques needed to fabricate those devices. Because this thesis covers several scientific and engineering fields this introduction has been divided in three sections.

The first section is about electrochemistry, the physical phenomena it involves, and also the basic experiments connecting the theory with empirical observations. The second part focuses on the working fundamentals of the two devices that have been designed, fabricated, characterized and tested. Finally the last section explains the three tools used in this thesis to fabricate the devices: simulation, microfabrication and prototyping.

1.1. Fundamentals of electrochemistry

Electrochemistry is the branch of chemistry dealing with the study of the interrelation between electrical and chemical effects [1]. Electrochemistry studies the chemical changes at an electrode when an electrical current is applied and also the production of electricity by chemical reactions. Electrochemistry has become the base of knowledge for a wide range of devices and processes such as electrochemical sensors, batteries, fuel cells and metal plating to mention only four.

A metal electrode has a lattice with closely packed atoms. This short distance between atoms allows electrons to move freely because the overlapping of the atomic orbitals within this lattice create a continuous state of energy called the Fermi level [2]. The Fermi level holds at a constant energy value until an electrical potential is applied to the electrode, when the Fermi level can move up or down from its initial position [1-3].

When a negative potential is applied to the electrode the electrons increase their level of energy getting closer to the level of the Lowest Unoccupied Molecular Orbital (LUMO) of electroactive species in solution, favoring the electron transfer from the electrode to the solution. On the other hand if the applied potential is positive the energy of the electrons decrease getting closer in this case to the Highest Occupied Molecular Orbital (HOMO) of electroactive species in solution and favoring the transfer from the solution to the electrode.

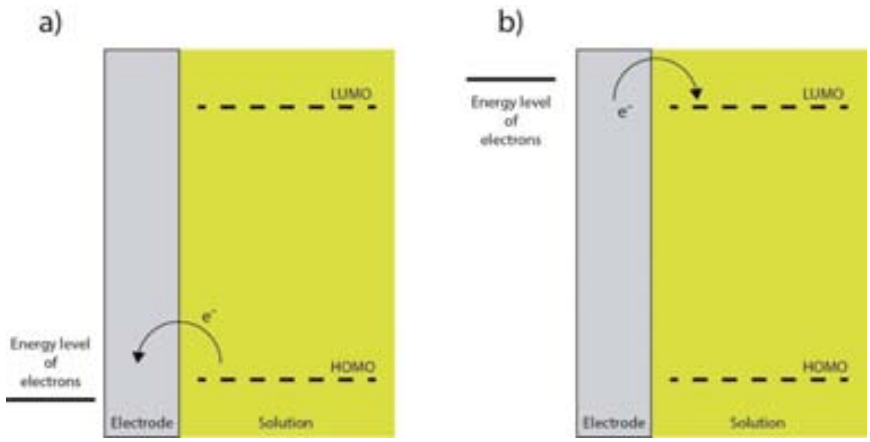

Figure 2. Energy levels and electron transfer favoring an oxidation a), and a reduction b).

Typically in an electrochemical process the transfer of charge between an electrically conductive electrode and a chemical species in solution is represented by equation (1).

$$O + ne^- \rightleftarrows R \tag{1}$$

Equation 1 represents an oxidized species *O* and a reduced species *R*. Species *O* is the species which gains 'n' electrons, in contrast to the species *R* which loses *n* electrons. Assuming rapid electron transfer, under equilibrium conditions the electrode potential follows the behavior described by Nernst's equation (2).

$$E_e = E^{o\prime} + \frac{RT}{nF} ln \frac{[O]_o}{[R]_o} \tag{2}$$

Where $E^{o'}$ is the formal potential of the reaction at equilibrium, $[O]_o$ and $[R]_o$ are the concentrations of the electroactive species in the solution, *F* is the Faraday constant, *R* the ideal gas constant and *T* is the temperature. In addition to this, the current density flux at the electrode (3) can be also expressed as a function of the concentrations of the electroactive species.

$$j = nF(k_{ox}[O]_o - k_{red}[R]_o) \tag{3}$$

Where k_{ox} and k_{red} are the electron transfer rate constant for the oxidation and the reduction processes, respectively.

1.1.1. Electrode kinetics

Electrode kinetics controls the electron transfer process between electrodes and chemical species in solution [2]. Kinetic rates can be adjusted by the potential applied to the electrode, and this section focuses on the relationship between the electron exchange rate and the electrode potential. Different theoretical models are available

to describe the way the rate of electron transfer can be controlled by the applied potential. These theories can be divided into microscopic, such as the Marcus theory [1, 4] and macroscopic, such as the Butler-Volmer model, which is based on empirical observation [1, 3].

The relation between electrode potentials and electron transfer rate can be described using the Gibbs free energy barrier [1, 2]. The theory of the Gibbs energy barrier says that a chemical reaction has to overcome a certain level of energy to take place, this minimum level of energy is called the standard free activation energy, ΔG^{++}. Figure 3 shows the usual transition state models for reduction and oxidation reactions.

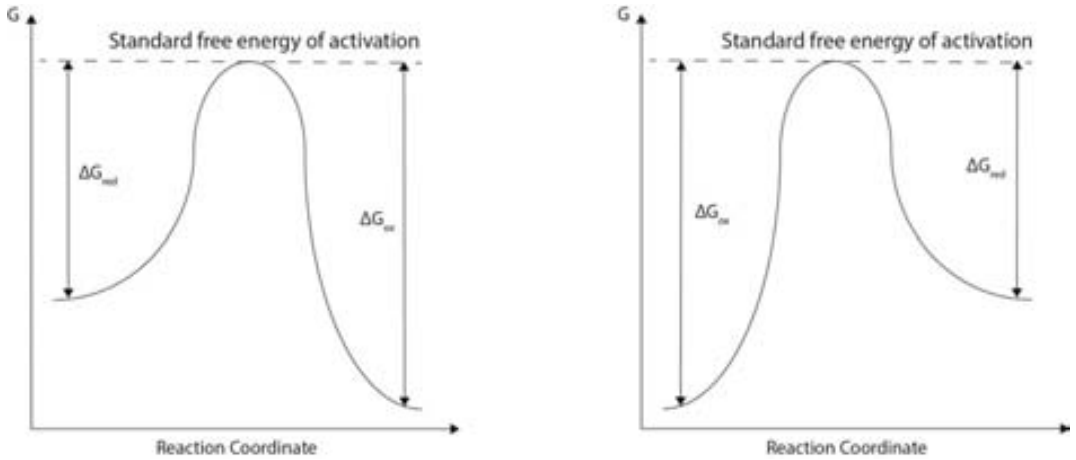

Figure 3. Transition state model for one electron reduction (left) and one electron oxidation (right).

The standard free activation energy can be described analytically. The expression of the standard free activation energy depends on whether the reaction is reductive (4) or oxidative (5).

$$\Delta G_{red} = \Delta G_o + \alpha nF(E_e - E^o) \tag{4}$$

$$\Delta G_{ox} = \Delta G_o - (1-\alpha)nF(E_e - E^o) \tag{5}$$

Where α is the charge transfer coefficient, which is related to the symmetry of the free energy barrier. The value of α is comprised between 0 and 1, but for metallic electrodes and outer-sphere electron transfer processes it takes a value around 0.5, ΔG_o is the free energy change accompanying the reaction when $E_e = E^o$.

At the equilibrium, and assuming α = 0.5 the standard free activation energy for the reduction and the oxidation of an electroactive species is the same ($\Delta G_{red} = \Delta G_{ox}$). However when an external potential is applied to the electrode, the standard free activation energy of any chemical reaction shifts, which indicates that the reaction can

be controlled by the potential favoring the oxidation or the reduction depending on the sign of the applied voltage. Using equations (4) and (5), the kinetic constants for the reduction (6) and the oxidation (7) of a chemical species can be written as follows:

$$k_{red} = A_{red} e^{-\Delta G_{red}/RT} e^{-\alpha n F(E-E_e)/RT} = k_{red}^{o} e^{-\alpha F\eta/RT} \tag{6}$$

$$k_{ox} = A_{ox} e^{-\Delta G_{ox}/RT} e^{(1-\alpha) n F(E-E_e)/RT} = k_{ox}^{o} e^{(1-\alpha) F\eta/RT} \tag{7}$$

Where A_{red} and A_{ox} are two variables which are related to the amount of collisions in an electrochemical process. Note also that a new expression is introduced here, it is called overpotential (8), and it describes the deviation of the applied potential from the value of the equilibrium potential [2].

$$\eta = E - E_e \tag{8}$$

Now the current flux (9) can be expressed as a function of the kinetic constants using (3), (6) and (7).

$$j = nF\left(k_{red}^{o} e^{-\alpha F\eta/RT}[O]_o - k_{ox}^{o} e^{(1-\alpha)F\eta/RT}[R]_o\right) \tag{9}$$

The net flux under equilibrium conditions is also known as the standard exchange current (10).

$$j_o = nFk^o [R]_{bulk}^{\alpha} [O]_{bulk}^{1-\alpha} \tag{10}$$

Where k^o is the electron transfer rate at equilibrium ($k_{red}^{o} = k_{ox}^{o} = k^o$), so the net current flux current can be expressed as follows:

$$j = j_o\left(\frac{[O]_o}{[O]_{bulk}} e^{-\alpha F\eta/RT} - \frac{[R]_o}{[R]_{bulk}} e^{(1-\alpha)F\eta/RT}\right) \tag{11}$$

Expression (11) is the Butler-Volmer equation, and it predicts how the observed current flux evolves as a function of overpotential and the charge transfer coefficient.

1.1.2. Mass transport

In order for electron transfer to occur, species in solution need to approach the electrode very closely. This is broadly known as mass transport and it can have three different forms, namely migration, convection and diffusion [2].

Migration

Migration is the movement of the ions caused by an external electric field. This occurs in electrochemical experiments as current flows between the working and counter electrodes. The corresponding electric field induces the movement of the ions in the solution by electrostatic forces from the solution to the electrode or viceversa. The movements caused by migration are proportional to the concentration of ions in the solution (C), the electric field gradient ($\partial\phi/\partial x$), and also to the ion mobility, μ. The mathematical expression describing the migration flux is (13).

$$j = -\mu C \frac{\partial \phi}{\partial x} \tag{13}$$

This component can be neglected when the concentration of electrolyte in the solution is high.

Convection

This transport is caused by the macroscopic movement of the solution. It may be due to a number of factors, but in general it is classified into two groups. The first one is called natural convection. Natural convection can be found in any solution and comes from thermal gradients or differences in the density of the solution. Natural convection becomes an important issue at macro electrodes and also because it is very difficult to predict as well [5-7]. The other form of convection is known as forced convection, and it is caused by external forces such as gas bubbling, stirring, or pumping. Mathematically, convective transport by convection is described by (12), where v_x is the velocity of the solution in movement.

$$j = -v_x \frac{\partial C}{\partial x} \tag{12}$$

Diffusion

Finally diffusion is the movement of species caused by concentration gradients. This phenomenon is described by Fick's laws. Fick's first law (14) describes the relationship between the concentration gradient and the flux density for any point and time.

$$-j_o(x,t) = \frac{i}{nFA} = D_o \frac{\partial C_o(x,t)}{\partial x} \tag{14}$$

Where n is the number of electrons, F is the Faraday constant, A is the area of the electrode and the current. This equation means that the flux is proportional to the concentration in a certain point for a given time. In addition to this, the second Fick's law (14) establishes that the concentration changes with time as:

$$\frac{\partial C_o(x,t)}{\partial t} = D_o \frac{\partial^2 C_o(x,t)}{\partial x^2} \rightarrow \frac{\partial C_o}{\partial t} = D_o \nabla^2 C_o \quad (15)$$

Where ∇^2 is the Laplacian operator, which depends on the geometry of the electrode used. Table 3 summarizes the Laplacian expressions for the most common geometries.

Table 3. The Laplacian operator for different geometries.

Type	Variables	Laplacian
Flat	x	$\partial^2/\partial x^2$
Sphere	r	$\partial^2/\partial r^2 + (2/r)(\partial/\partial r)$
Cylinder	r	$\partial^2/\partial r^2 + (1/r)(\partial/\partial r)$
Disk	r, z	$\partial^2/\partial r^2 + (1/r)(\partial/\partial r) + \partial^2/\partial z^2$
Band	x, z	$\partial^2/\partial x^2 + \partial^2/\partial z^2$

1.1.3. Instrumental methods

The main experimental set-up used in this thesis to study the electrochemical behavior of all the devices and materials developed is based on a three-electrode configuration as depicted in Figure 4 *a)*. These three electrodes are connected to a potentiostat. In this type of experiments the electrode under study is called working electrode, another electrode provides a potential reference, and it holds a constant potential in the solution where the working electrode is also immersed. The potentiostat imposes a potential difference between the working and the reference electrodes, and measures the current passing through the working and auxiliary electrodes. A potentiostat is an instrument that controls the potential difference between the working electrode – counter electrode pair and adjusts the voltage to keep the desired voltage potential difference between the working and reference electrodes by a function generator, which provides potential wave functions with different shapes. These waves describe the type of experiment used and serve to characterize different properties of the working electrode and the species in solution [1, 3].

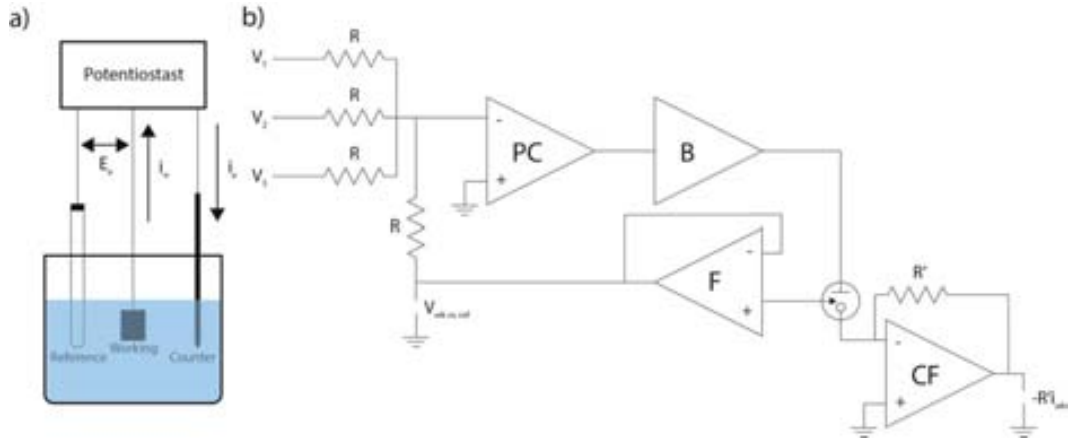

Figure 4. Schematic representation of a three electrode set-up for electrochemical experiments a), and electrical schematic of a potentistat b).

Figure 4 *b)* shows the electrical schematic of a potentiostat. The electronic design of a potenstiostat is basically composed by four parts; a potential control amplifier (PC) in adder configuration, a booster (B), a voltage follower (F) and a current follower (CF). The potential control amplifier stage amplifies a voltage input signal A_{oA} times, where A_{oA} is the open-loop gain of the operational amplifier. Note that the potential control amplifier is in adder configuration. This means that the input signal of the amplifier is an addition of different simple voltage waveforms permitting the creation of complex voltage signals. The potential control amplifier is connected to a booster amplifier. A booster amplifier is a noninverting amplifier whose open-loop gain (A_B) is lower than a normal amplifier, but which is capable of providing higher levels of voltage and current. The output of the booster is connected to the counter electrode. A voltage follower is inserted in the feedback loop of the potential control amplifier to avoid the pass of current to the reference electrode. Finally a current follower, whose noninverting input is connected to the working electrode, collects the current generated by the working electrode [1, 8, 9].

Different electrochemical experiments can be carried out depending on the shape of the waveform applied at the input of the potential control amplifier. Three types of experiments have been carried out in this thesis. These are based on the application of potential steps, potential sweeps and potential staircases [1, 2].

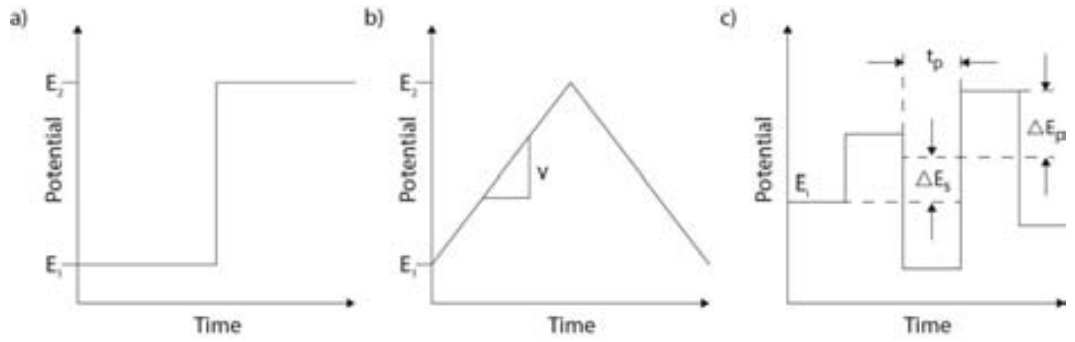

Figure 5. Graphical representation of the electrochemical experiments used in this thesis, a) chronoamperometry, b) cyclic voltammetry and c) square wave voltammetry.

Chronoamperometry

Chronoamperometry or potential step experiments, Figure 5 *a)*, represent the simplest electrochemical experiment offering a current transient response. The applied potential in chronoamperometry is stepped from a constant value where no reaction occurs (E_1), and as a consequence no electrons flow, to an another potential (E_2) where the oxidation or reduction of chemical species in solution is diffusion controlled. Mathematically, the Cottrel equation (16) describes the current response at a flat electrode as function of time.

$$|i| = nFAC\sqrt{D/\pi t} \tag{16}$$

Where n is the number of electrons, F is the Faraday constant, A is the area of the electrode, C is the concentration of the solution, D is the diffusion coefficient and t is the time. In the simplest case chronoamperometry is used to measure the concentration and diffusion coefficients of species in solution by analyzing the transient current response.

Cyclic voltammetry

In cyclic voltammetry (CV), Figure 5 *b)*, the potential is linearly scanned from a potential E_1 at which no current flows; that is, the chemical species under study is neither oxidized nor reduced. The potential from this point increases linearly with a slope, called scan rate (υ), up to a potential (E_2) where the oxidation or reduction of chemical species in solution is again mass-transport controlled. In addition to this last linear sweep potential the reverse scan is also done to complete the study and assess the reversibility of the process. This technique is very widely used and very useful as it offers complete kinetic and thermodynamic information. The key parameters are peak current (i_p), potential peak separation (ΔE_p) and their scan-rate dependence. The

Randles-Ševčík equation (17) predicts the peak current for a given scan rate at a flat electrode.

$$|i_p| = 0.4463nFAC\sqrt{{nFDv}/{RT}} \quad (17)$$

Where n is the number of electrons, F is the Faraday constant, A is the area of the electrode, C is the concentration of the solution, D is the diffusion coefficient and R is the ideal gas constant, T is the temperature and v is the scan rate.

Square wave voltammetry

In square wave voltammetry (SWV), Figure 5 *c)*, a train of pulses is superimposed over a linear potential ramp. A SWV experiment is defined by a series of parameters, the height of the pulse (ΔE_p), which can start at an initial potential (E_i), the duration of the pulse (t_p) and finally the staircase shift (ΔE_s) [1].

SWV is used in chapter 3 of this thesis. In this chapter stripping scans by square wave voltammetry have been used for the detection of mercury in aqueous solutions. Stripping analysis comprises two steps; the first one, called accumulation step, holds a constant voltage during a certain time to deposit the metals to be analyzed on the surface of the electrode. The second step is the stripping step where the metals are released from the electrode. The response of this type of experiment is a current peak which potential is characteristic of each metal.

The next section describes the working principle of fuel cells because they are key of electrochemical devices which have been designed, fabricated and characterized as final goal of this thesis.

1.2. Fundamentals of fuel cells

The section aims to explain the working principles of fuel cells, and particularly the microbial fuel cells that have been designed, fabricated and characterized in this thesis. This section also covers their current applications.

1.2.1. Energy generation in fuel cells

Batteries and fuel cells (FC) are electrochemical devices that convert chemical energy into electricity through the reduction and oxidation of chemical species [10]. When a battery or fuel cell is connected to an external circuit the electrons flow from the anode to the cathode through the external circuit, while ionic species carry the charge through the electrolyte.

The difference between a fuel cell and a battery is that while fuel cells work as long as a fuel is passed through them, batteries contain a fixed amount of charge and they no longer
work once this charge has been spent. From this point this thesis will only explain the generation of energy by fuel cells. To understand the operation of fuel cells, it is necessary to describe the architecture of these devices first. Mainly a fuel cell is formed by three parts:

1. Anode. This is the part of any fuel cell where the oxidation of the fuel takes place, so the electrons are delivered to the external circuit from here. The electrode in the anode must be made from a catalyst material such it can oxidize the fuel at the lowest possible potential. This material must also offer good electrical conductivity and stability.

2. Cathode. Electrons flow into the cathode from the anode through the external circuit. The material of cathode should be able to reduce the chemical species used as electron acceptor at the highest possible potential. The material used to fabricate the cathode has to share the same properties regarding the stability in contact with the electrolyte and the electrical conductivity as well.

3. Electrolyte. This is the medium where the ions move inside the battery or fuel cell from the anode to the cathode. The electrolyte must transfer the ions, but not the electrons because these must be transported through the external circuit. Another important feature of the electrolyte is that it does not react with any of the two electrodes.

1.2.2. Polymer electrolyte membrane fuel cells and their performance

The fuel cells studied in this thesis are Polymer Electrolyte Membrane Fuel Cells (PEMFC) [11-14]. PEMFCs employ a thin polymeric membrane as electrolyte, but it also serves to isolate the reactions on the anode and the cathode from each other [15].

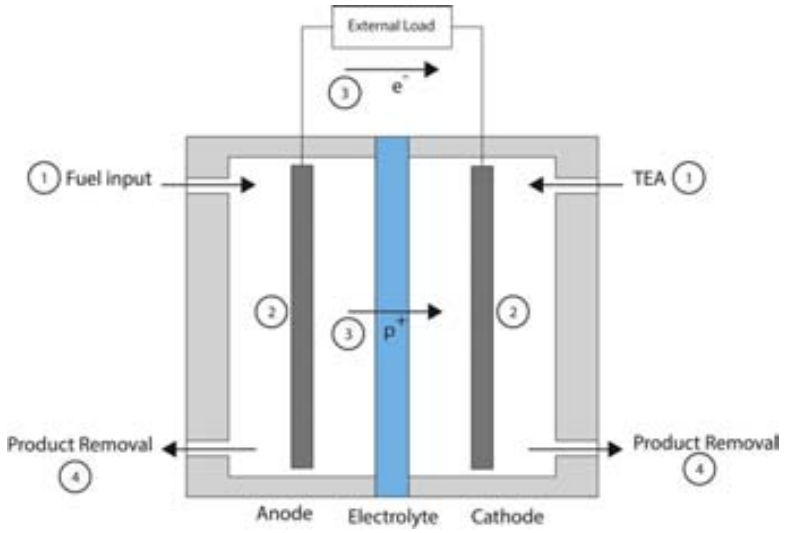

Figure 6. Cross section of a fuel cell showing the different parts and processes to generate current.

The generation of current in a PEMFC involves several steps, which are represented for convenience in the schematic view of a PEMFC showed in Figure 6.

1. Transport of the fuel and Terminal Electron Acceptor (TEA). First of all a fuel cell has to be constantly supplied with fuel in the anode to generate electrons. The fuel is pumped by an external source into the chamber where the anode is placed. In the cathode a Terminal Electron Acceptor (TEA) is also introduced to allow the transport of electrons from the anode to the cathode.

2. Electrode processes. At this step when the fuel, the TEA or a catalyst necessary for the right operation of a fuel cell are delivered to the anode and the cathode, an oxidation and/or reduction takes place. These reactions are totally necessary because without them the flow of charge from the anode to the cathode cannot occur. Sometimes a catalyst is added to increase the velocity and efficiency of a chemical reaction with the goal of improving the performance of the device [16].

3. Electronic and ionic conduction. The electrochemical reaction occurring at the anode produces electrons and ions. Both of them have to be consumed in the cathode to keep the charge balance. Electrons move from the anode to the cathode by an external circuit while ions travel to the cathode through an electrolyte membrane which only allows the pass of this type of electrical charge.

4. Product removal: The reactions at the anode and cathode produce undesired products which must be removed from the reaction chamber to avoid

depletion of the fuel cell and to allow the reaction on the electrodes of new fuel and the necessary chemical species.

The electrical performance of a fuel cell is described by three electrical parameters: the voltage between anode and cathode, the passing current, and the output power. These parameters are commonly plotted in a graph called current – voltage plot. One example of this type of graph is showed in Figure 7. This curve is essential to study the efficiency of a fuel cell because all the parameters that describe the electrical performance of a fuel cell are represented there.

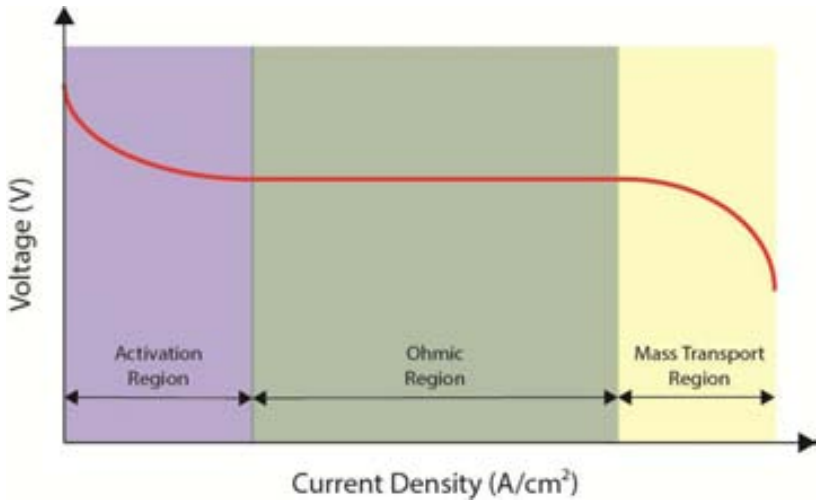

Figure 7. Example of a current - voltage graph and the work regions of fuel cells.

In addition to the maximum current that a fuel cell can generate, the design and fabrication have an important role in the performance of the final device. Bad design or wrong choice of materials can lead to important electrical losses. There are three main types of losses, each of them associated with one of the elements inside a fuel cell.

1. Activation losses come from the conditions under which reactions occur in the anode and in the cathode. The main source of activation losses is the electron transfer between the electrode surface and the fuel or the electron acceptor, which limits the amount of electrons generated by a fuel cell. Electron transfer depends on the material used to fabricate the electrodes, which choice has to be in agreement with the desirable output power. Ideally the most desirable material to fabricate the electrodes is that which has the highest electron transfer rate and the capacity of reducing the overpotential of the reaction. However this may not always be possible, in most cases due to cost reasons.

2. Ohmic losses are related to voltage drops between the anode and the cathode. In a fuel cell there are two types of charges: the electrons and the protons, but only the ionic transport presents difficulties due to their large mass in contrast

to the mass of the electron, so the transport of ions between the anode and the cathode is the factor which affects the ohmic losses. These losses affect the voltage of fuel cells according to Ohm's law, which establishes a relationship between the voltage and the electrical resistance ($V = I \cdot R$). Ohmic losses can be reduced using high conductivity solutions, materials with high conductivity to fabricate the electrodes, or also decreasing the distance between both electrodes. In addition to the design of the electrodes ohmic losses can also been reduced using electrolytes with low resistance.

3. Mass transport losses are caused by the slow movement of the reactants and/or the products needed and generated by a fuel cell. If the anode does not evacuate the exhausted fuel and replace it with fresh it will mean a reduction of the concentration of fresh fuel because the volume of the reactor is limited. Regarding the cathode if it does not evacuate the waste products it means that the concentration of TEA will not be the optimum. Allowing both issues will mean a lower electrical performance of the fuel cell. The only way to minimize these losses is the design of flow structure to facilitate as much as possible the flow of reactants in and out the fuel cell.

In addition to the voltage and current an extra electrical parameter, the output power density of a fuel cell, can be calculated using the expression (18) at any point of the i – V graph.

$$P = VI \tag{18}$$

Figure 8 shows an example of a current density – voltage and a current density – power plot. This plot also indicates the most important parameters to study the electrical response of any fuel cell. These parameters are the open circuit voltage (OCV), the maximum current density and the maximum power density.

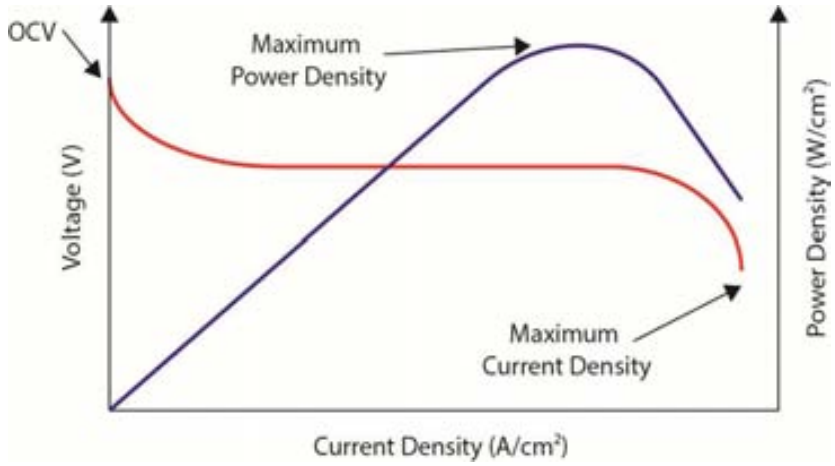

Figure 8. Example of a current - voltage (red) and a current - power (blue) graphs sharing the same plot with the three most important electrical parameters for describing a fuel cell.

The OCV is the voltage of a fuel cell when the current generated by it is zero. Also this voltage is the maximum voltage generated by a fuel cell. The maximum current density is the maximum current that a fuel cell can deliver, divided by the working electrode area. The maximum current density belongs to the point where the fuel cell voltage is zero. Finally the maximum power density is the maximum output power that a fuel cell can generate divided by the area of the electrode.

1.2.3. Bio – energy generation: Microbial fuel cells

A microbial fuel cell (MFC) is a type of fuel cell that uses microorganisms to produce electricity. These microorganisms oxidize organic fuel from an external source producing electrons inside them which travel from inside the microorganism by respiratory enzymes to the electrode where they are exchanged [17].

These electrons produced by the microorganism travel through an external circuit towards the cathode, where the corresponding TEA is supplied from outside the fuel cell. Protons, as in other fuel cells, travel from the anode to the cathode across the electrolyte.

As it was mentioned above, MFCs use special microorganisms able to deliver electrons to the anode [18]. These are called exoelectrogens, and there are two known mechanisms which can describe their electron transfer [19, 20].

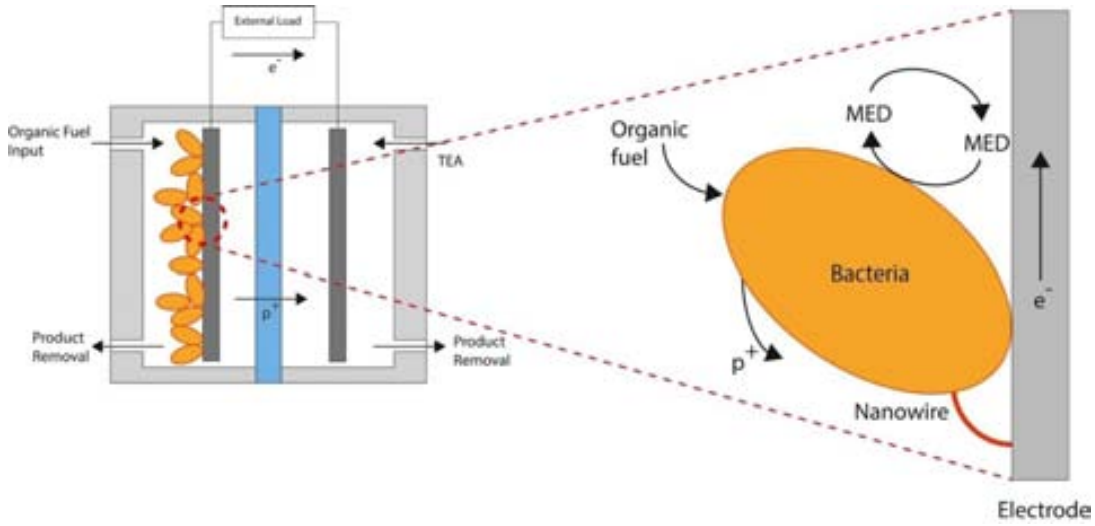

Figure 9. Schematic representation of a microbial fuel cell. On the left the different part which set-up a microbial fuel cell, and on the right a bacteria delivering electrons to an electrode by two different mechanisms.

The first of these mechanisms involves nanowires [21, 22]. Nanowires are thin conductive wires, which in the case of exoelectrogenic bacteria, carry electrons from inside the bacteria to an electrode. Some bacteria species such as *Geobacter* or *Shewanella* species transfer their electrons through nanowires. The second mechanism involves the transport of the electrons produced by the bacteria by self-produced mediators (MED) [23, 24]. The MED transport the electrons generated by the own metabolism of the bacteria to the surface of the electrode.

Due to their low output power density, MFCs [25-28] are not ideal as energy sources. However, they can be used as toxicity sensors [29-32], to improve the energy efficiency of wastewater treatment processes [33] and to generate high added value chemicals [34-37].

1.3. Materials and methods

This section covers the three main processes in the fabrication of the devices presented in this thesis; these are microfabrication, simulations and encapsulation. First of all the processes used for micromachining silicon and for pyrolyzing photoresist are briefly described. After this, the fundamentals of Finite Element Simulations (FEM) are explained. The last part of this chapter also describes some rapid-prototyping techniques that were used during this thesis.

1.3.1. Silicon microfabrication processes

Microelectrodes are fabricated using silicon microfabriation techniques inside a cleanroom. The main reason is that the fabrication environment (temperature,

humidity, and air flow) needs to be strictly controlled because the processes carried out in micro technology are strongly affected by slightly variations of the environment conditions inside a cleanroom [38-42]. Particle contamination is avoided in a cleanroom by two means. First, a positive pressure is kept inside the cleanroom relative to the outside. Second protective clothing is worn inside the cleanroom to prevent the staff from contaminating the work areas. Humidity and temperature are also under control to prevent changes arising from external factors that could otherwise affect the conditions of the different processes.

Figure 10. Different sections of the cleanroom of the Institute for Microelectronics of Barcelona.

The first step to fabricate a new microelectrode-based device is its design. The design requires a deep understanding of the final application, but also of the tools and processes involved in the fabrication. Once the application is understood, one may start defining the geometry of the device, the materials and processes involved in their fabrication and their sequence. This section provides an overview of the main clean room processes used in the microfabrication of electrodes.

Photolithography

Photolithography is the key process in any microfabrication plan, as it allows the transfer of structures to the substrate. Typically, a photocurable resist is exposed to UV-light thorough a photomask where the structures are defined. The patterns in a photomask are created using a layout editor, which is essentially a CAD software where 2D structures are drawn and assigned to different layers depending on the different materials and processes involved in the fabrication [43, 44]. Layers are drawn in a layout editor corresponding to separate lithographic steps to be followed by different processes. Alignment and test structures ensure the correct combination and

quality of fabrication steps, and enable the construction of more complex devices on a substrate.

In addition to the substrate, the main components of a photolithographic process are the photomask and the photoresist. Photomasks are commonly made in soda lime or quartz, although the use of high-resolution and high-density transparencies is becoming increasingly common even beyond the prototyping phase. In a conventional quartz or soda-lime glass photomask, the patterns to be transferred to the desired substrate (e.g.: a silicon chip or wafer) are defined in chromium, usually by laser lithography. When transparencies are defined in ink instead chromium. Depending on whether the patterns in the photomask are printed or transparent, the mask is "bright-field" or "dark-field", respectively. This is important because the photoresist and the process after the lithography will determine the polarity of the photomask.

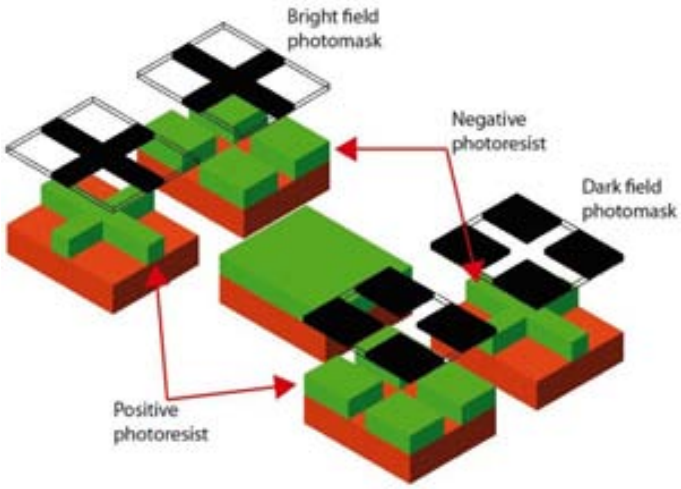

Figure 11. Differences between the polarization of photoresist and the two types of photomasks.

Photoresists can be either positive or negative, depending on their reaction to UV light. Positive resists become more soluble in the developing solvent after insolation, whereas negative photoresists present the opposite behaviour. That is, the unexposed regions are more soluble in developing solvent than exposed areas.

Thermal oxidation

The electronics industry uses silicon mainly due to its semiconducting properties, which allow the fabrication of complex integrated circuits. However, electroanalytical devices hardly ever take advantage of such properties. In fact, nearly all silicon-based microelectrodes use silicon merely as a substrate on which to create micro- and nano-electrode based devices. To avoid leakage and background currents, the electrodes need to be insulated from the silicon substrate by means of a dielectric layer [38, 40-42]. Although silicon presents a thin layer of native oxide, this can be too thin to

provide a complete isolation of the electrodes. Thicker and more robust oxide layers can be achieved by thermal oxidation of the silicon in an oxygen-rich atmosphere. Depending on the oxygen source, thermal oxidation may be wet or dry. Wet oxidation uses water vapor and dry oxidation is based on oxygen gas. Although both ways have advantages and disadvantages, dry oxidation leads to oxides with better properties, such as more homogeneity and better thickness control, but the process is slower than wet oxidation.

In the work presented in this thesis, one micron thick thermal oxide layer was grown on 4-inch silicon wafers. This layer is enough to provide a good electrical isolation between the electrodes, which have been explained in the chapters 2 and 3, and the silicon substrate to avoid leakage currents.

Rapid thermal processes

A Rapid Thermal Process (RTP) is that process which submits a silicon wafer to high temperatures for a short time [40, 41] using rapid heating lamps or lasers. RTP processes find many applications in silicon manufacturing processes such as metal silicide and nitride formation, ion implantation damage annealing and activation, dielectric formation and annealing, and the reflow of deposited oxides [45-48]. The cooling down process occurs at lower velocities to avoid thermal shock, and for this reason the temperature of the wafer is measured and monitored constantly.

The use of RTP processes has been extensively used in the chapter 3 of this thesis for the synthesis of Pyrolyzed Photoresist Films (PPF). The synthesis of PPF implies the use of high temperature ovens which can also ranges different values of temperature at different rates what converts RTP processes in the best choice to fabricate PPF electrodes with customized properties.

Etching

Etching processes allow the removal of material from a substrate. Typically, etching processes may be combined with lithography to define the regions to be etched. Etching processes can be divided in two process groups, namely wet and dry etching.

When etching takes place in a chemical bath, and therefore involves solvents and/or solutions, it is broadly known as wet etching. This type of etching commonly consists of three steps: (i) application of the etchant species, (ii) etching reaction with the unprotected substrate and (iii) removal of the etching solution. Although this type of etching presents many disadvantages, such as lack of control during the process,

presence of a large amount of particles, and high isotropy, it is still used to remove large amounts of a substrate due to its high selectivity.

Dry etching, or plasma etching, on the other hand, is based on the removal of material from a substrate by bombarding it with free ions produced by plasma and cast on it by an electromagnetic field. The impacting ions follow straight trajectories normal to the substrate, and result in highly anisotropic etching rates. In addition, dry etching is easier to control than wet etching. Reproducibility and anisotropy have become this type of etching the best choice to pattern the shape of any microelectrode in different substrates.

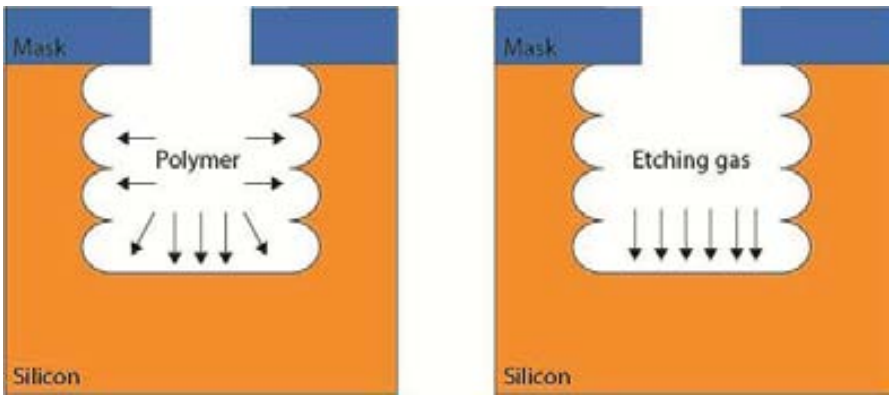

Figure 12. Both steps which forms the Bosch method for a DRIE etching, polymerization (left) and etching (right).

Although dry etching is superior to wet etching when anisotropic profiles are sought, it is important to bear in mind that dry etch profiles appear nearly isotropic when the depth of the etching is very large. To avoid this effect, time-multiplexing deep reactive ion etching techniques such as the Bosch process have been developed. [49, 50] The Bosch method alternates the etching of the substrate and a polymerization reaction on its surface as protection of the sidewalls of the previously etched substrate. This protection is achieved because the polymer at the bottom is removed much more easily than that on the side-walls, which are kept virtually intact. Both steps (etching and protection) are continuously repeated until the desire depth of the substrate is removed.

The Bosch method is one of the most important processes used in this thesis. With this process high aspect ratio vertical microstructures have been fabricated to develop and study a new type of microelectrode arrays which provide much larger density current than flat electrodes. For more details the fabrication parameters of the process which was carried out with Bosch method are explained in chapter 2.

Thin-film deposition

At some point, microfabrication involves the deposition of different materials on a substrate. Deposition processes may be divided in two main types: Physical Vapor Deposition (PVD) and Chemical Vapor Deposition (CVD) [51, 52].

PVD techniques can be used to deposit a wide range of materials, although they are mainly used to deposit metals, either by evaporation or sputtering. In evaporation, the material is subject to high temperatures and low pressures, which facilitates the vaporization of the material. Once vaporized, the material travels in a straight line to the substrate where it condenses into thin films. Sputtering is the other technique most broadly used for the deposition of metals (although other materials can also be deposited with this technique). Here the source of the material to be deposited, also called target, is polarized at a high negative potential while bombarded with positive argon ions. The target material is subsequently sputtered as neutral atoms by momentum transfer, travelling a short distance towards the substrate across a strong electromagnetic field. One of the main advantages of sputtering compared to evaporation is its ability to cover vertical walls. Sputtered films also present better adhesion and are more often used in industrial production settings. Evaporation, on the other hand, is preferred when substrate heating needs to be avoided. Thanks to this the micropillars fabricated by DRIE in the chapter 2 could be totally metallized with gold in spite of vertical walls.

The second family of deposition techniques is Chemical Vapor Deposition (CVD). In this case the deposited films arise from the reaction of the different constituents, all of them in gaseous phase. This technique is commonly used to deposit materials such as silicon dioxide, silicon nitride, or polysilicon. Depending on the specifications needed on the final device it is possible to deposit the material using different techniques. By Low Pressure Chemical Vapor Deposition, LPCVD, the uniformity of the material to be deposited will be the greater. On the other hand, if the deposition takes place in a plasma reactor, Plasma Enhanced Chemical Vapor Deposition, the temperature of the process is lower. In chapter 3 a passivation layer composed by SiO_2 and Si_3N_4 was deposited by CVD over a carbon substrate to define the active electrode areas, which is very important in electroanalysis.

Electroplating

Electroplating is an electrochemical technique that permits the coating of an electrically conductive surface with a metal [53-56]. To metallize an electrode by electroplating, an anode and, a cathode (electrode to be metallized) must be placed in an electrolytic cell and connected to a source of electrical current. When the anode is

connected to the positive terminal and the cathode to the negative the metal at the anode is oxidized to form cations that associate with the anions in the solution. These ions are reduced at the cathode, covering its surface.

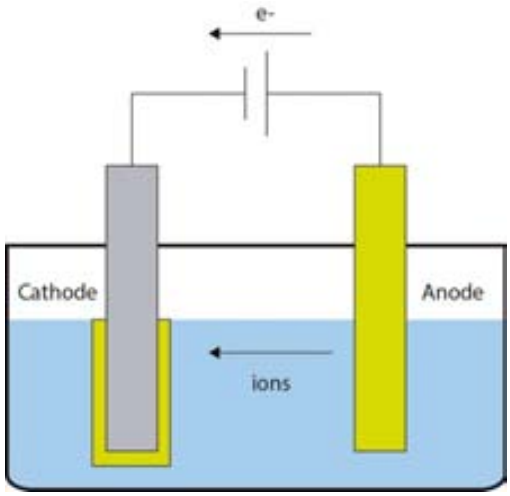

Figure 13. Graphical scheme of an electroplating process.

Electroplating has been long used in the electronics industry in different stages of it such as PCB protection, electromagnetic shielding or manufacturing processes [43]. In this thesis electroplating has been used in chapter 2 to grow fully-conducting micropillar array electrodes using gold as electrode metal.

Cleaning Techniques

Wafer contamination may have different sources: single particles or clusters of particles, adsorbed ions or elements and undesirable thin films. Cleaning techniques in microfabrication focus on material removal without damaging or modifying the characteristics of the materials and devices on the wafers [57]. Keeping wafers clean throughout the fabrication processes helps to increase the performance, yield and reliability of the devices.

Different cleaning techniques may be used to remove the contamination from a wafer substrate. Wet cleaning processes are based on using organic solvents, aqueous solutions, or a combination of both to eliminate the contamination on the surface of the wafers. Depending on the type of contaminant, the chemicals used can vary. For example, a mixture of HF and deionized water is used to remove thin films of silicon dioxide created under the exposure of the wafer to silanes used in the synthesis of silicon based materials such as SiO_2 or Si_3N_4.

Organic matter is removed by a binary process known as RCA (Radio Corporation America) cleanliness. RCA uses solutions which are composed by mixtures of H_2O, H_2O_2, HF, HCl and NH_4OH. This process comprises three steps, the first one removes

organic compounds, and also elements such as Cu, Au, Ag, Zn, Cd, Ni, Co, and Cr in a solution 1:1:5 of NH_4OH, H_2O_2 and H_20 respectively at 80 ºC for around 10 minutes. Note that this step forms a thin layer of SiO_2 that will be removed in the second step. The second step removes the SiO_2 soaking the wafers in a 1:50 solution of HF and H_2O at 25 ºC. The third step removes remaining traces of metallic contaminants, which were not removed during the first step, soaking the wafers in a 1:1:6 solution of HCl, H_2O_2 and H_2O. After finishing the last step the wafers must be rinsed and dried. Rinsing the wafers means cleaning with deionized water and under ultrasounds to eliminate remained reactants from the wet cleaning and after that the wafers must be dried to remove the water by different techniques: spinning, evaporation in a hot plate or purging N_2.

Dry cleaning removes the contamination physically, for instance by bombarding undesired films with plasma. This type of cleaning is commonly used to remove traces of deposited photoresist after lithography. This technique uses a plasma processor with O_2 or N_2 as reactive gases to remove the photoresist bombarding it. The choice of the gas to create the plasma is related to the ease of the substrate under the photoresist to oxidize. The main disadvantage of this technique lays in the need to control process time. Because dry etching is an aggressive process, excessive exposure of the substrate to plasma may result in damages to the structures in it, depending on the material in which they are made.

1.3.2. Finite Element Method (FEM) simulations

Finite element methods (FEM) comprise a range of numerical techniques to find an accurate solution of a continuous problem using an approximate view of it [58-60].

The first step to start to simulate a problem by FEM is the definition of the geometry of the domain. The domain is a delimited space where the user wants to study a problem. To find out the solution to a given problem any FEM algorithm split or discretize the domain in a finite number of individual components interconnected with their surroundings. The set of all of these individual components or elements is called mesh. The division of the domain permits to solve individually each one of the components to have an easier and also faster solution of the physical parameters which describe a component. The equations and parameters which describe all of these components are governed and described by partial differential equations (PDE) within a set of boundary conditions. The boundary conditions are the expressions whose function is to describe the nature of the problem. A problem can have one or more boundary conditions and these conditions can be described by the same or by different expressions. Besides, the choice of the right boundary condition at the right points where it must be placed depend on the knowledge and/or the intuition of the user

because he is who decides the structure of the problem. A bad choice of the boundary conditions, or even the wrong place where it is placed will provide a wrong solution of the problem.

In addition to the mesh and the boundary conditions other mechanisms are necessary to solve a problem by FEM, these are the basis functions. The basis functions help to find an approximation of the solution of the problem by the construction of interpolation polynomials using a finite number of parameters or also called Degrees of Freedom (DOF), so the DOF are possible solutions of the problem in a particular node. The accuracy of the solution in a particular node depends on the order of the interpolation polynomial, but at the same time the bigger the order is the bigger the amount of computational resources that are required to find the solution, so the user has to find a compromise between the accuracy of the final solution of the problem and the available resources. Once the algorithm has guessed a solution for each one of the nodes which compose the domain it tries to solve the generated system of equations to give a unique solution for each node. At this point the algorithm checks if the solution of the system of equations at a specific node with the solution of the same system for the surrounding nodes is within a specified range of error, also called tolerance. If the solution is outside this tolerance the algorithm assigns new values at each node and check again that the values are within the tolerance. This process of guessing and solving is repeated until the algorithm converges; in other words, the solution of the problem is found within tolerance value chosen by the user.

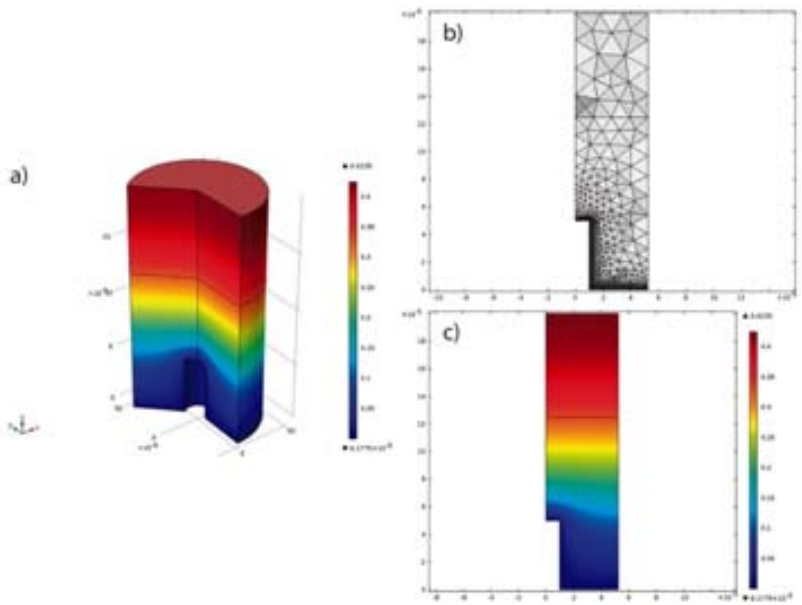

Figure 14. Example of a single domain of a fully-conducting micropillar electrode simulated with COMSOL. 3D micropillar electrode a), simplification to a 2D domain showing its mesh b), and final result of a 2D micropillar electrode.

1.3.2.1. Commercial FEM software: COMSOL Multiphysics

Until recently, most FEM algorithms had been written by the own users using any of the available high-level programming language such as C or Pascal. This task required a lot of time to be entirely developed because the entire FEM routine had to be written, and the code had to be checked to avoid errros. However currently there are several commercial FEM software packages in the market which permit to solve virtually any problem involving the use of Partial Differential Equations (PDE). This thesis includes a section in chapter 2 where commercial FEM software called COMSOL Multiphysics has been used to solve the mass transport at fully-conducting micropillar array electrodes. Figure 14 shows three images of the computational model developed in chapter 2 to study the electrochemical response of fully-conducting micropillar array electrodes.

COMSOL Multiphysics is a commercial software package based on FEM [61]. The main advantage of COMSOL lies in the ease to create any stage of a computational model based on FEM to solve a specific problem. This software includes a CAD tool to draw the domain easily. In addition to this the mesh can be defined automatically specifying the size and shape of each subdomain, and it is even possible to define different mesh densities within a domain. COMSOL permits to solve different types of physical problems. COMSOL is composed of different modules, each one of them focused on a specific field or branch of the science or technology. Each one of the modules has predefined the equations, boundary conditions and the conditions needed to describe a specific problem. Also a model can have different modules interconnected between them if different phenomena are involved in a problem. Finally the analysis to carry out is also predefined by COMSOL, allowing to have in the same model different types of analysis to study a problem from different points of view. Also different solvers are available. The results can be plotted in many different ways within COMSOL itself, or they can be exported to a file to be processed using data analysis software, such as Origin in the case of this thesis.

Despite their advantages commercial FEM software presents importants risks [62] because the user does not control the algorithms and numerical method used by the software. In an attempt to prevent accuracy problems arising from this, in this thesis the chronoamperometry and cyclic voltammetry of a flat electrode were simulated and compared to the analytical solutions for the mass transport controlled current at planar electrodes, and the mesh and tolerances were refined to until simulated and analytical results were in an arrangement better than a 0.1%. After this was possible to simulate more complex geometries, such as the fully-conducting micropillar array electrode in chapter 2. The goal of this was focused on showing that the results of the simulations obtained using COMSOL are reliable by the comparison with the analytical prediction described by Cottrell and Randles−Ševčík equations.

1.3.3. Rapid – prototyping techniques

Rapid – prototyping techniques aim to shorten the product development cycle. These techniques enable the fabrication of a working device in a short period of time, without using complex processes and also as cost effectively possible. The use of rapid – prototyping techniques is found in a wide ranges of applications in different fields of science and technology such as the development of electrochemical sensors, in electronics such as in the development of Printed Circuit boards (PCB) or flexible electronics, or also in mechanical engineering as well [63-67]. Rapid – prototyping techniques were used in this thesis to fabricate the miniaturized microbial fuel cells developed in chapter 4.

To fabricate the miniaturized microbial fuel cells devices only were necessary two prototyping techniques, they were by drilling and milling [68, 69], blade cutting jointly with laminating [70-72]. To help with the layered design and fabrication of any device by rapid – prototyping, different CAD (Computer Aided Design) or drawing software can be used. These software packages provide a wide range of functions to draw in 2D or 3D, besides their rendering engines can show a first approximation of the different pieces to create with the milling / drilling machines and the cutting plotter as well. During the development of this thesis Vectorworks 2012 (Nemetschek) and Illustrator CS5 (Adobe) were used to design the different devices.

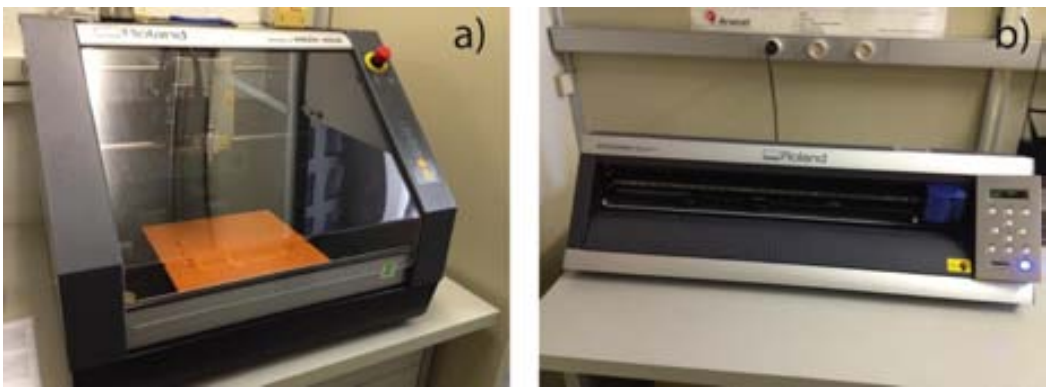

Figure 15. Rapid - prototyping equipment used in this thesis, a) Milling machine, b) and cutter plotter.

Milling and drilling are two mechanical techniques that permit respectively to remove and make holes from a workpiece [73] following a prior design. A drilling – milling machine permits the use of a wide range of different tools which can have different diameters and lengths, also these tools can work at different speeds depending on the desired final result of the user. The drilling – milling machine used to fabricate the miniaturized microbial fuel cells of chapter 4 was continuously connected to a computer that controlled and transferred the different operations and the position of the tool to perform the work by a computer numerical control (CNC) software. This

CNC software continuously controls the position of the tool; the software used here was the VCarve Pro (Vectric Ltd, UK). The model of the milling-drilling machine used is a Roland MDX-40A, and it is showed in Figure 15 *a)*. In this machine the x, y origin is defined by the user, whereas the z origin is automatically determined by the machine using a position sensor each time the tool is replaced.

Razor writing is a technique commonly used in the sign or advertisement industry for cutting graphics in adhesive plastics films. However with the improvement of cutting plotters, which currently offer resolutions down to a few hundreds of microns, razor writing has become an ideal rapid – prototyping technique used to create microstructures in films achieving faster and cheaper fabrications of devices for different applications. A cutter plotter is a plotter fit with a knife blade with few microns of thickness capable of cutting different polymers or films of different materials, Figure 15 b) shows the cutting plotter used for developing the devices of chapter 4, the model used in this chapter is a Roland CAMM-1 Servo. To transfer the different designs from the used CAD to the cutting plotter intermediate software was necessary to interpret the route the knife blade has to follow, the software used is called CutStudio 1.5 (Roland). The design and the choice of the knife blade can vary depending on the nature of the material, currently there exist three different types of cutter plotters [70], but for this thesis only one was necessary to cut the adhesive layer used in chapter 4. The method used is known as the drag knife cutting method, and it uses a swivel blade that follows the cutting path of the design [74]. The tip used to cut the different adhesive layers was a general purpose carbride, Figure 16 shows one example of this type of tip.

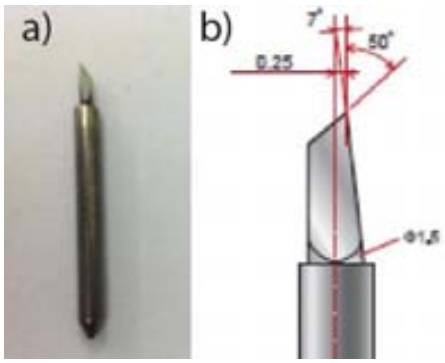

Figure 16. On the left a photo of a general purpose carbride tip, and on the right its design specifictions.

Chapter 2. Enhanced mass transport at micromachined electrodes

This chapter presents the design, fabrication and characterization of fully-conducting micropillar array electrodes. This chapter begins with the theoretical description of the mass transport at fully-conducting micropillar array electrodes. Next, a FEM computational model was developed to study the mass transport of this kind of electrodes prior to their fabrication. Micropillar array electrodes were fabricated using silicon micromachining techniques. First of all the micropillar arrays were fabricated by gold electrodeposition, but this method shows low reproducibility and high roughness at the top of these microstructures. To solve these both problems the micropillar were fabricated by DRIE and metallized by dc-sputtering, this technique presented high reproducibility and a good arrangement between computational results and experiments.

The work presented in this chapter has been published in the Journal of Electroanalytical Chemistry (*R. Prehn, L. Abad, **D. Sánchez-Molas**, M. Duch, N. Sabaté, F. J. del Campo, F. X. Muñoz, and R. G. Compton, "Microfabrication and characterization of cylinder micropillar array electrodes," Journal of Electroanalytical Chemistry, vol. 662, pp. 361-370, 2011.*), where my contribution focused on the development of the computational model and also of the physical characterization of the electrodeposited micropillars. Another paper was published in The Journal of Physical Chemistry C *(**D. Sánchez-Molas**, J. P. Esquivel, N. Sabaté, F. X. Muñoz, and F. J. del Campo, "High Aspect-Ratio, Fully Conducting Gold Micropillar Array Electrodes: Silicon Micromachining and Electrochemical Characterization," in The Journal of Physical Chemistry C, ed, 2012*).

2.1. Introduction

The use of microfabrication techniques in electrochemistry has given birth to many new devices, such as microelectrode arrays [75], nanoelectrodes and their arrays [76-80], and an entire research area known as lab on a chip [81] that includes microreactors and miniaturized fuel cells [29, 82-84]. Most of these devices have found application in electroanalysis in the form of chemical sensors and biosensors [75], but also as tools for the study of fundamental phenomena at the micro and nano scale [75, 77, 85].

When designing and constructing micro-and-nano electrode arrays, the goal is to take advantage of hemispherical diffusion to each component of the array for as long as possible before the diffusion layers of adjacent micro or nano electrodes overlap, because at that point the current response becomes controlled by planar diffusion to the whole array, and device performance dismishes. Among the virtues of micro-and-nano electrode arrays is the signal amplification provided compared to single micro-or-nano electrodes, while keeping some of the mass transport characteristics of the individual units composing them. Three-dimensional electrochemical interfaces provide a much larger surface area than planar electrodes, and this leads to higher sensitivities, higher current collections, and lower impedance. In certain electroanalytical applications, such as biosensors, using electrodes with a larger surface area means that more bioactive material can be immobilized on the electrode, which increases sensitivity and biosensor lifetime [15]. This chapter focuses on the study, fabrication and characterization of 3-dimensional microelectrodes with the goal of enhancing the sensitivity and also the current density of sensors and energy sources.

To predict and understand the behaviour that a given micro-or-nano electrode is likely to show, simulations help identify critical issues linked to the fabrication, so that the adequate fabrication processes and conditions may be selected. Finite-element software COMSOL Multiphysics has helped to design electrodes prior to their fabrication. COMSOL is a “black box” that facilitates the solution of non-linear differential equations in complex systems at the expense of user control over the algorithms and numerical methods, which is not the case when programs are written and compiled in languages such as C or Matlab, Cuttress et al. recently warned against the limitations of commercial finite element software [86]. We assumed fast Butler-Volmer electrode kinetics, and have solved the mass transport equations to micropillar arrays of different geometries, and from these simulations we have calculated the corresponding diffusion-controlled currents at those electrodes. To facilitate calculation, the diffusion domain approach has been used. This technique allows the simplification of the problem, going from 3-dimensional structures to 2-dimensional simulation domains [87]. This has been possible due to the cylindrical geometry of the pillars, and the fact that they are regularly spread across the chip surface.

This chapter presents two methods to create fully-conducting micropillar array electrodes; one relies on the electrodeposition of gold, while the other one is a combination of silicon dry etching and sputter metallization. The first method is based on using a combination of microfabrication techniques, photolithography and electroplating to fill holes patterned in a photoresist layer. These holes served as moulds to fill with electrodeposited gold and create the microstructures. Electrodeposited micropillars displayed rough top surfaces, which was associated to

the current density applied during electrodeposition. Also, because the electrodeposition was carried out at full wafer level (4 inches), uneven current

distribution inside the reactor resulted in different micropillar heights across the wafer, making it a somewhat more unveliable method than silicon micromachining to produce micropillar structures. My contribution in the development of this kind of micropillar array electrodes is limited to the simulation of their electrochemical response and also their physical characterization.

The second method to produce fully-conducting micropillars consists in the fabrication using a combination of photolithography and reactive ion etching steps, in a process known as the Bosch process [43]. After the creation of the silicon structures, a thermal oxide layer was grown to provide electrical insulation of the electrode surface from the silicon substrate, and finally the oxidized structures were metallized by dc–sputtering to provide a thin conductive layer over the entire electrode surface, even for the tallest structures. Once fabricated, both types of electrodes were characterized and their experimental results compared with the theory.

2.2. Mass transport at fully-conducting micropillar array electrodes.

2.2.1. Theory of mass transport at fully-conducting micropillar

A one-electron electrode process is assumed:

$$O + e^- \rightleftarrows R \tag{19}$$

The approach of electroactive species to the electrode is described by Fick's second law:

$$\frac{\partial C(r,t)}{\partial t} = D\nabla^2 C(r,t) \tag{20}$$

Where D_O, D_R, C_O and C_R are the diffusion coefficients and the concentrations of the electroactive species *O* and *R*, respectively. The resulting currents can be calculated by integration of Fick's first law equation, which describes the net flux of material at the electrode:

$$-J = \frac{i}{nFA} = D\frac{\partial C(r,t)}{\partial r} \tag{21}$$

Where *n* is the number of electrons involved, *F* is Faraday's constant and *A* is the electrode area. In our case, we are also assuming that electron transfer at the electrode surface follows a Butler-Volmer type potential dependence; and that electron transfer is fast:

$$J = J_o \frac{C}{C_o} exp\left[\frac{-\alpha nF}{\bar{R}T}\left(E - E^{o'}\right)\right] \tag{22}$$

Here α is the charge transfer coefficient, for which a value of 0.5 is assumed, $\bar{R}$ is the gas constant, *T* is the absolute temperature and $E^{o'}$ is the formal potential of the redox couple. To facilitate the solution of the mass transport equations, the geometric scope of the problem has been limited to 2 dimensions in the case of micropillar array electrodes, and to 1 dimension in the case of the planar electrode. The former is more broadly known as the diffusion domain approach [87], which validity has been thoroughly demonstrated for a range of different geometries at the microscale. Thus, it is possible to use such approach to describe the behavior of disk microelectrode arrays [88], arrays of microbands [89], partially blocked electrodes [90, 91], micro-ring - disk devices [92], and cylindrical microelectrodes [93].

The planar electrode case is trivial and will not be discussed here. However, the description of how the micropillar electrodes were modeled is relevant to the interpretation of our experimental results, and will be addressed next.

The diffusional current at an individual micropillar is obtained by integration of the diffusional flux at the electrode boundaries as described below. For obvious reasons, mass transport to a cylindrical micropillar is best described using cylindrical coordinates (see annex 1). Then it is possible to break down the current observed by a micropillar electrode into three components, which are the contribution of the vertical walls, the contribution of the top face, and the contribution of the basal surface between pillars.

$$i_{Dom} = i_{side} + i_{top} + i_{base} \tag{23}$$

In turn, to calculate these current terms, we must consider the diffusional flux at each type of boundary. The current at the walls is obtained integrating the flux over the micropillar height along the z axis and the angle φ around its base.

$$i_{side} = nFD \int_0^{\varphi}\int_0^{z} \rho \frac{\partial C(\rho, t)}{\partial \rho} d\varphi dz \tag{24}$$

In the case of a full cylinder, the height interval ranges from 0 to $h_{\mu Pill}$ and the azimuth φ ranges from 0 to 2π radians.

$$i_{side} = 2\pi nFDr_{\mu Pill} \int_0^{h_{\mu Pill}} \frac{\partial C(\rho,t)}{\partial \rho} dz \tag{25}$$

The current at the top cylinder face has a similar form:

$$i_{top} = nFD \int_0^{2\pi} \int_0^{\rho} \rho \frac{\partial C(z,t)}{\partial z} d\rho d\varphi \tag{26}$$

In this case the azimuth interval is the same, but now the current depends on the radial position, ρ, which ranges from 0 to the radius $r_{\mu Pill}$. The current contribution for the top face is described by:

$$i_{top} = 2\pi nFD \int_0^{r_{\mu Pill}} \rho \frac{\partial C(z,t)}{\partial z} d\rho \tag{27}$$

So the total micropillar current is the addition of both contributions:

$$i_{\mu Pill} = 2\pi nFD \left(r_{\mu Pill} \int_0^{h_{\mu Pill}} \frac{\partial C(\rho,t)}{\partial \rho} dz + \int_0^{r_{\mu Pill}} \rho \frac{\partial C(z,t)}{\partial z} d\rho \right) \tag{28}$$

In addition, for fully-conducting system, the basal region also contributes to the current, so the overall value of the current in one domain becomes (29).

$$i_{Dom} = 2\pi nFD \left(r_{\mu Pill} \int_0^{h_{\mu Pill}} \frac{\partial C(\rho,t)}{\partial \rho} dz + \int_0^{r_{\mu Pill}} \rho \frac{\partial C(z,t)}{\partial z} d\rho + \int_{r_{\mu Pill}}^{r_d} \rho \frac{\partial C(z,t)}{\partial z} d\rho \right) \tag{29}$$

Finally, the current at the whole array is obtained multiplying the individual domain current times the number of micropillars in the array.

2.2.2. Computational model

COMSOL Multiphysics, a commercial finite element software package, was used to solve these equations for two different geometries: planar and fully conducting micropillar array electrodes using the Chemical Reaction Engineering module in COMSOL Multiphysics v4.2.

2.2.2.1. Model simplification

In order to model the diffusional current at an array of cylinder electrodes, the diffusion domain approach was used to simplify the problem geometry. In summary, this technique consists in assigning each cylinder in the array its own diffusionally independent region. Here this is a hexagon which radius is the distance between micropillar centres, *d*. These regions present cylindrical symmetry around the vertical axis, which allows further simplification from a 3-dimensional problem to a 2-dimensional domain that represents a section of the micropillar and its surroundings. Each of these domains must have the same base area as the hexagonal unit cell of the array, $\pi r_d^2 = d^2 v3/2$, which provides the radius of the 2D domain. This simplification is showed in *Figure 17*.

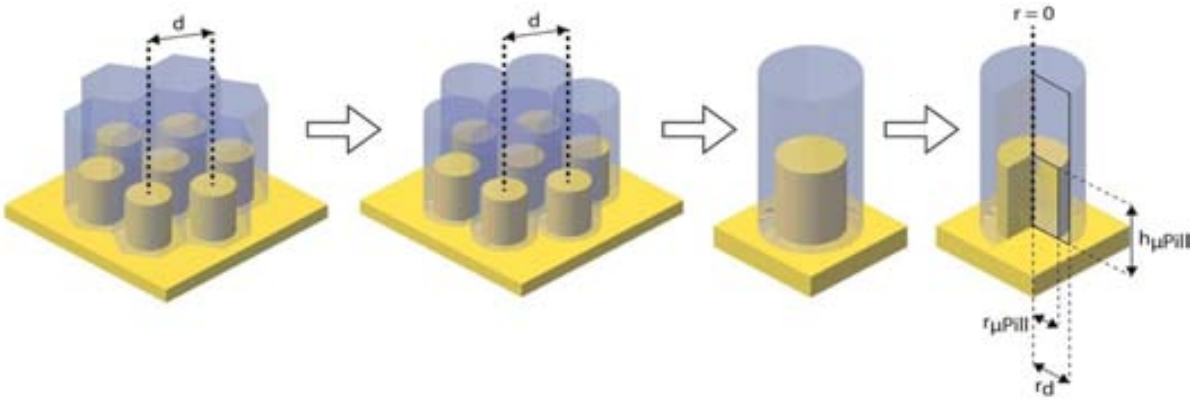

Figure 17. Schematic representation of the diffusion domain approach, from a 3D hexagonal lattice to a 2D cylindrical domain.

For an array where the micropillars are distributed in a square lattice the radius of the cylindrical domain is calculated as follows: $d^2 = \pi r_d^2$, where *d* in this case is the center-to-center distance between two adjacent micropillars.

2.2.2.2. Boundaries and time dependent mesh

Once the bidimensional model is designed, the different boundary conditions can be specified on the model. These boundaries are the different equations which define each one of the physical laws in the different regions of the computational model. The boundary conditions used in this model are summarized in Table 4.

Table 4. Boundary conditions used in the simulations.

Boundary	Equations	Domain region
1	$[O] = [O]_{bulk}$	$0 \le r \le r_d, z = z_d$
2	$[R] = 0$	$0 \le r \le r_d, z = z_d$
3	$\frac{\partial O}{\partial r} = \frac{\partial R}{\partial r} = 0$	$r = 0, h_{\mu Pill} < z < z_d$ $r = r_d, 0 < z < z_d$
4	$D_O \frac{\partial O}{\partial r} = -D_R \frac{\partial R}{\partial r} = k_f O - k_f R$	$r \le r_{\mu Pill}, z = h_{\mu Pill}$ $r = r_{\mu Pill}, 0 < z < h_{\mu Pill}$ $r_{\mu Pill} < r \le r_d, z = 0$

To minimize computing time without compromising accuracy, the size of the domain and the mesh density have been made dependent on the timescale of the computational problem, t_{sim}. Domain heights were established so that the top boundary position does not affect the solution of the simulation, and can safely be considered as bulk solution. Table 5 shows the mesh density used as a function of position in the domain.

Table 5. Description of the time-dependent mesh used in the simulations.

Mesh density	Geometric scope	
	r	**z**
$\sqrt{t_{sim}D}/6$	$0 \le r \le r_d$	$h_{\mu Pill} + \sqrt{t_{sim}D} < z \le h_{\mu Pill} + 6\sqrt{t_{sim}D}$
$\sqrt{t_{sim}D}/8$	$0 \le r \le r_d$	$h_{\mu Pill} + \sqrt{t_{sim}D}/2 < z \le h_{\mu Pill} + \sqrt{t_{sim}D}$
$\sqrt{t_{sim}D}/10$	$0 \le r \le r_d$ $r_{\mu Pill} < r \le r_d$	$h_{\mu Pill} < z \le h_{\mu Pill} + \sqrt{t_{sim}D}/2$ $0 < z \le h_{\mu Pill} + \sqrt{t_{sim}D}/2$
$3 \cdot 10^{-7}$ - $1 \cdot 10^{-6}$	$0 \le r \le r_{\mu Pill}$ $r = r_{\mu Pill}$	$z = h_{\mu Pill}$ $0 \le z \le h_{\mu Pill} + \sqrt{t_{sim}D}/2$

In addition, mesh density was refined until the difference between Randles – Ševčík and Cottrell's equations and the simulated results for the planar electrode case was less than 0.1%.

2.2.2.3. Simulated electrochemical experiments

Simulation of potential step experiments was carried out from a potential at which no appreciable reaction occurs, to one at which oxidation readily occurs and a concentration gradient is established. Cyclic voltammetry experiments, on the other hand, were simulated imposing a triangular potential wave, again from a potential at which no reaction occurs, towards potentials at which oxidation of electroactive

species becomes diffusion controlled. Dimensionless variables were used throughout our simulations. As described in Table 6, all geometric parameters were normalized to the micropillar radius, and concentration terms were normalized to the bulk concentration in the system.

Table 6. Dimensionless parameters used in the simulations.

Parameter	Definition
R	$r_d/r_{\mu Pill}$
Z	$h_{\mu Pill}/r_{\mu Pill}$
τ	$D_O t/r_{\mu Pill}^2$
C_O'	$C_O/c_{O,bulk}$
C_R'	$C_R/c_{O,bulk}$
j	$i/2\pi F\ D_O C_{O,bulk} r_{\mu Pill}$

2.2.3. Design of fully-conducting micropillar array electrodes: Computational study

To study the dependency between current and micropillar geometry ($h_{\mu Pill}$ and $r_{\mu Pill}$) and center-to-center distance (d), a number of different geometries were simulated and fabricated, these are summarized in Table 7.

Table 7. Geometric description of the micropillar arrays simulated and fabricated.

$r_{\mu Pill}$ (μm)	d (μm)	$h_{\mu Pill}$ (μm)	R	Z
5	20	5	2	1
5	50	5	5	1
10	40	5	2	0.5
10	100	5	5	0.5
5	20	25	2	5
5	50	25	5	5
10	40	25	2	2.5
10	100	25	5	2.5
5	20	50	2	10
5	50	50	5	10
10	40	50	2	5
10	100	50	5	5
5	20	125	2	25
5	50	125	5	25
10	40	125	2	12.5
10	100	125	5	12.5

All of these geometries were chosen to provide an exhaustive analysis of the current density as a function of micropillar geometry and basal domains. Note that although some dimensionless geometries are repeated, the real geometries are different. The purpose was to study the coherence of the dimensionless conversion for different real systems.

2.2.4. Theoretical results

This section presents the results obtained in the simulations for the two types of electrochemical experiments described in section 2.2.2.3.

2.2.4.1. Cyclic voltammetry simulations

Figure 18 shows the simulated peak current densities vs. the square root of scan rate for micropillar arrays with different densities. Diffusionally controlled processes lead to straight peak current vs. √υ plots. The different segments in the plots shown in Figure 18 indicate the presence of different, time dependent, diffusional modes.

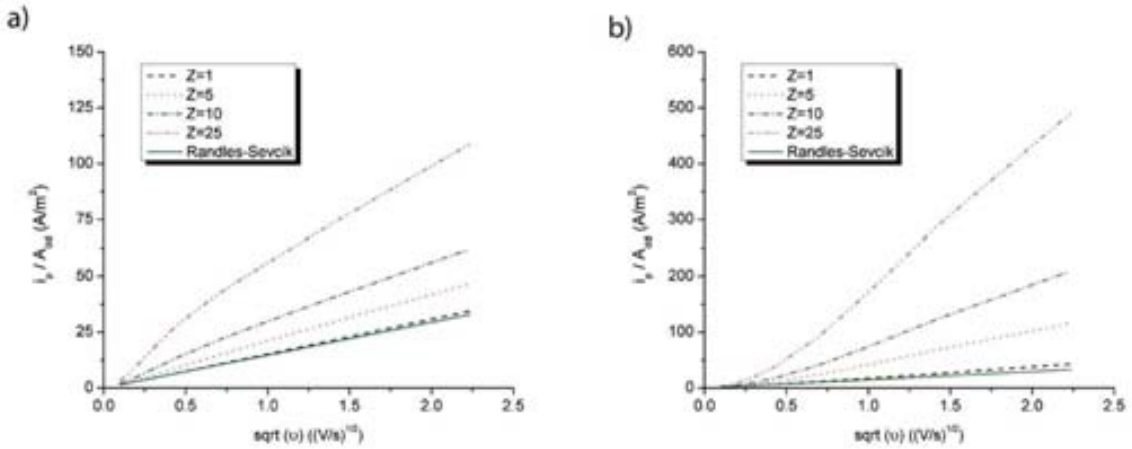

Figure 18. Simulated voltammetric peak current density as a function of the square root of the scan rate for two different dimensionless densities, R=5 (a) and R=2 (b).

The curves represented in this figure show at least three distinct regions, corresponding to planar diffusion to the surface of the micropillars and their base (fast scan rates), a transition region in which the material confined between micropillars is completely depleted, and a third segment dominated by planar diffusion from the solution bulk to the array (slow scan rates). Although this is present in all micropillar arrays, it is more easily visible in the case of taller micropillar arrays. For very densely populated microarrays, such as the case represented in Figure 18*.b,* the intermediate region is much more difficult to observe because the material contained in the space between micropillars is quickly depleted and there is nearly no time for hemispherical diffusion to set in.

Similarly to other microstructured electrodes, four different diffusion categories can be distinguished at micropillar array electrodes. At very short times, when the diffusion layer thickness is significantly smaller than the micropillar size, the concentration profile can be considered planar, and the current is proportional to the real surface area of the electrode. This is normally referred to as case 1, and in voltammetric experiments corresponds to faster scan rates. Case 2 occurs when radial diffusion sets in at the edges of the micrometric features on the electrode surface. In the case of cylindrical micropillar array electrodes, this would be on the edges around the top face of the cylinders. Case 2 would correspond to fast-to-moderate scan rates. Eventually these radial diffusion layers begin to overlap, but the concentration profiles still retain some of their non-planar structure. This is case 3, when planar diffusion continues to operate at the electrode base and on the sidewalls of the microcylinders, while radial diffusion operates at their top-side edge. Eventually the effect of radial diffusion at the top of the cylinders will be swamped by the growth of the diffusion layer of the entire electrode, so that planar diffusion will predominate in case 4. Case 4 arises in voltammetry at slow scan rates by two ways depending on the geometry of the array.

One limiting case corresponds to a high density of pillars – tall pillars highly packed on the electrode surface. The second limiting case occurs when there is a low density of pillars – short pillars sparsely spread across the electrode surface. When there is a high pillar density, planar diffusion is reached because the diffusion layers of adjacent pillars overlap. On the other hand, when pillar density is low, planar diffusion is reached as the diffusion layer developing from the conducting base around the electrodes effectively ‘‘swallows’’ the pillars and their individual diffusion layers. In the first case, it is the top side of the pillars that is effectively contributing to the observed current. In the second case, the contribution of the pillars to the overall current is negligible. The first case reminds of a porous electrode, while the second case may be compared to a rough electrode. Thus, there are two factors affecting the response of fully conducting micropillar array electrodes. These are the size of the pillars – a combination of pillar radius and pillar of height – and the density of pillars. But whether the pillars in the array are very densely packed, resembling a porous electrode, or are only sparingly scattered over a planar surface, such an electrode will eventually display behavior consistent with planar diffusion, hence making it virtually impossible to discriminate between a porous or a rough electrode from the voltammetric peak current at slow scan rates. Henstridge and co-workers have very recently reported [94, 95] this from the perspective of porous electrodes with different pore sizes, and concluded that, ‘‘Randles-Ševčík behavior is observed at both very high and very low cylinder separation with a greatly enhanced peak current being seen at intermediate separation which is dependent on the film thickness.’’ Figure 19 shows the concentration profiles corresponding to the peak potential at six different scan rates, representing the four diffusion cases described before. The figure shows that, in

contrast to the case of the planar electrode, the dimensionless current at micropillar array electrodes depends on scan rate.

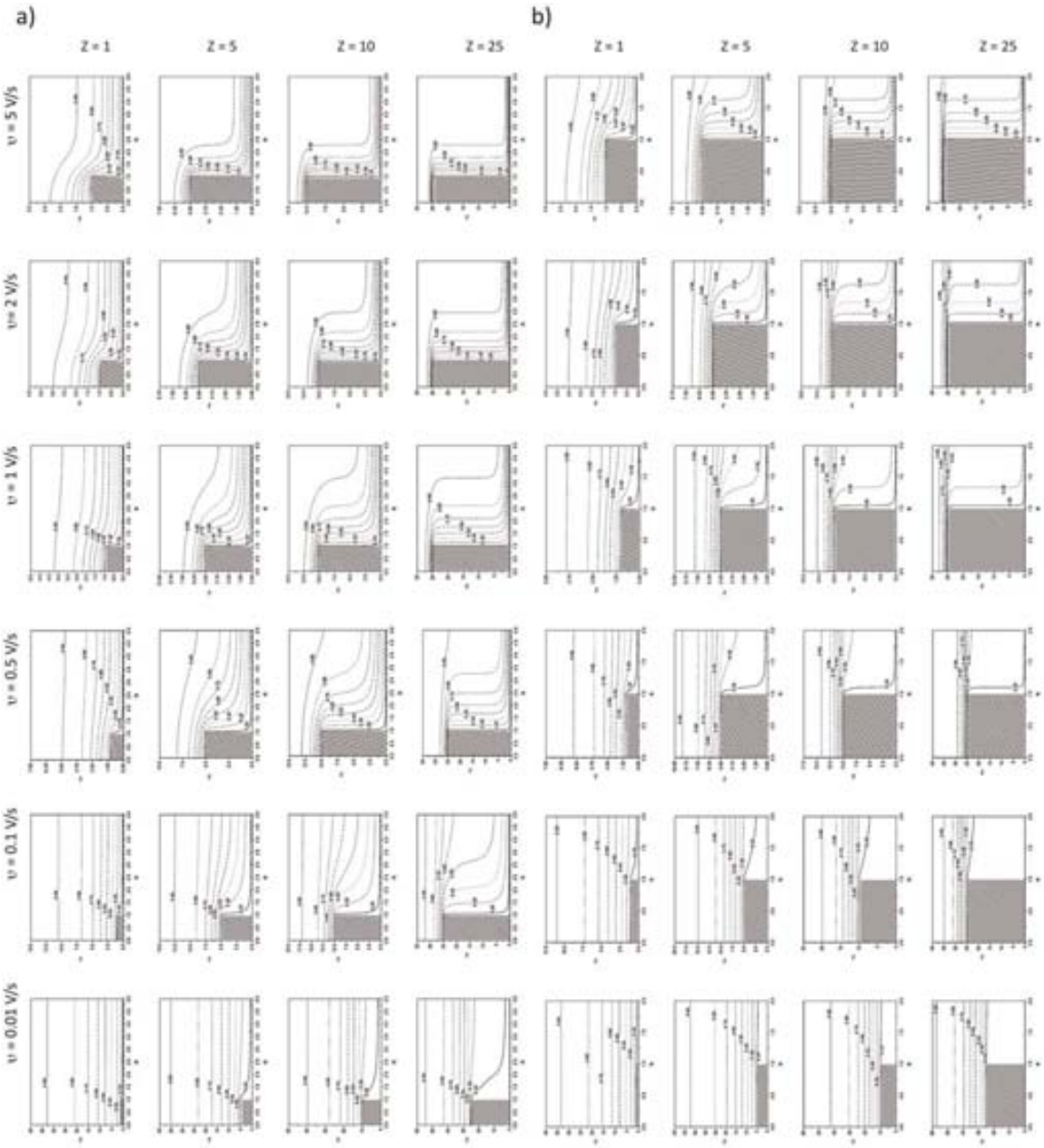

Figure 19. Concentration profiles at the peak potential and different scan rates in simulated cyclic voltammetries for R=5 (a) and R=2 (b).

2.2.4.2. Potential step simulations

The chronoamperometric response of a micropillar array electrode is controlled by micropillar height, represented here by dimensionless parameter *Z*, and micropillar density, represented by parameter *R*. Note that micropillar radius is considered in both of these parameters. Figure 20 shows some chronoamperometries for micropillar

arrays of four different dimensionless heights: Z = 1, 5, 10 and 25, and two different densities: R = 5 and 2, respectively.

The response of those micropillar array geometries is shown along the transient current corresponding to a planar electrode of same area as that of the microelectrode arrays. These figures show log-log plots of current density vs. time in which it is easy to observe at least three distinct regions, related to the four different behavior cases of the micropillar arrays [94, 95].

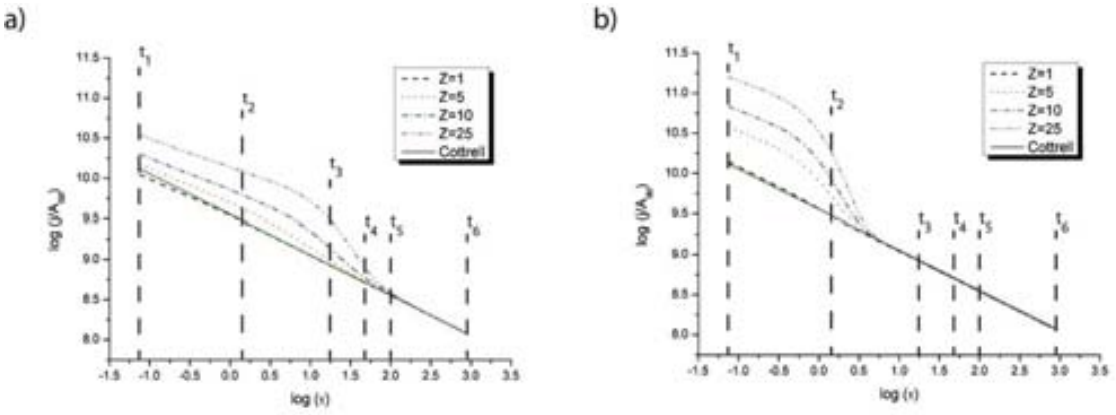

Figure 20. Simulated chronoamperometry at arrays of different geometries R=5 (a) and R=2 (b).

Case 1 behavior occurs at very short times, when the diffusion layer is much smaller than the size of the micropillars, and planar diffusion to the surface of the micropillars and their base dominates. The slope of -1/2 appearing in the early region of the log-log plot of Figure 20 is consistent with this. Following this period of planar diffusion comes a region of current decay in which the material is fully depleted in the space between pillars; sections t_3-t_4 in Figure 20 *a),* and section t_2-t_3 in Figure 20 *b).*

The diffusion layer in this region is comparable to the separation between micropillars, and the current decay is due to the consumption of the material occupying this space between them. The shape and extent of this decay depends both on micropillar height and on the separation distance between pillars.

This current decay region corresponds to behavior cases 2 and 3 in disk microelectrode arrays. Last, when the diffusion layer is greater than micropillar radius and the separation between micropillars, planar diffusion to the entire array sets in, and behavior case 4 is observed.

For convenience, Figure 21 *a) and b)* show concentration profiles from the shortest to the tallest micropillar arrays, at the times highlighted in the transients displayed in Figure 20. The concentration profiles in Figure 21 reveal the relative importance of planar diffusion to the vertical walls vs. hemispherical diffusion to the micropillar tops during the current decay region. Simulations show that planar diffusion to the walls is

dominant for high aspect ratio structures, and that planar diffusion to the base is dominant for very low aspect ratio structures. On the other hand, hemispherical diffusion seems more important in those intermediate cases in which the aspect ratio of the pillar approaches unity; that is, when Z/R = 1.

Also note that, unsurprisingly, higher pillars display larger initial currents (Figure 20_*a) and b*) due to their larger (side) surface area. On the other hand, increasing the separation between micropillars leads to slightly lower maximum currents due to a lower micropillar density (Figure 20.*a*) that can be sustained longer times because the volume between pillars is greater and therefore it takes longer to deplete.

Also, because larger separations allow the diffusion of material from the bulk solution that can replenish the material consumed by the micropillars.

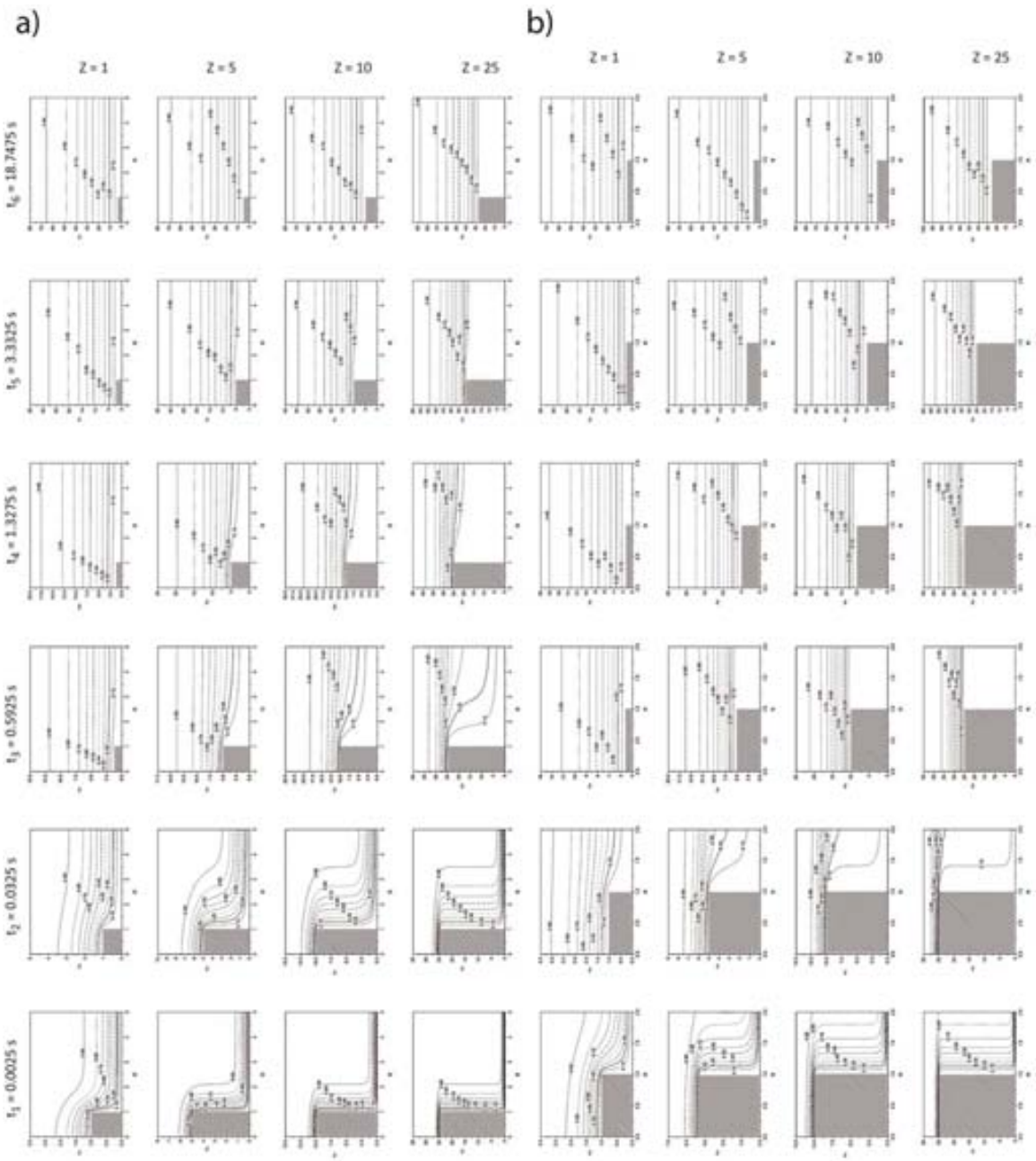

Figure 21. Concentration profiles for fully-conducting micropillar array electrodes with R=5 (a) and R=2 (b) at different times.

This is illustrated experimentally in Figure 22, which displays the responses of micropillar array geometries from Table 8. This figure shows that while the current limits are the same for micropillars of identical *Z* and *R* parameters, the transition between the maximum current level and the typical Cottrellian level depends on the actual geometry of the device.

Table 8. Equivalent micropillar array geometries compared.

	$r_{\mu Pill}$ (μm)	d (μm)	$h_{\mu Pill}$ (μm)	R	Z
Geometry 1	5	20	25	2	5
Geometry 2	5	50	25	5	5
Geometry 3	10	40	50	2	5
Geometry 4	10	100	50	5	5

Thus, when geometries 1 and 3 in Table 8 are compared, the current decays sooner in geometry 1 than in geometry 3 arrays because the actual volume between pillars in geometry 1 is smaller and therefore the material contained within it can be depleted more rapidly than in geometry 3 arrays.

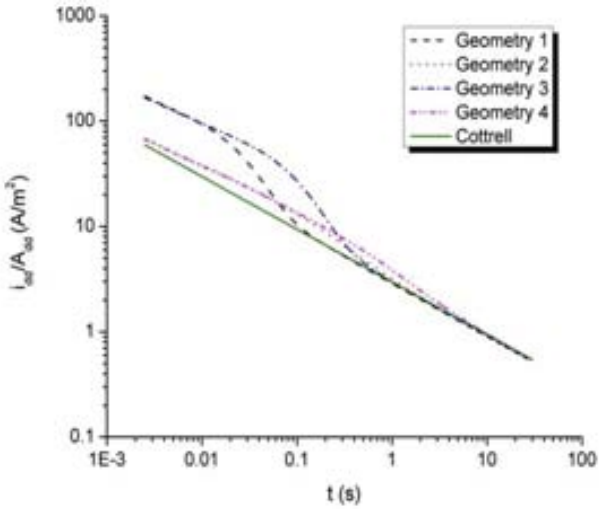

Figure 22. Simulated chronoamperograms for four different arrays sharing dimensionless parameters arising from different actual size parameter values.

A similar pattern is observed for geometries 2 and 4 in Table 8, with geometry 4 presenting a much larger inter-pillar volume than geometry 2. Also, note that the current passed by micropillar geometries 2 and 4 goes through a maximum shortly before the current decays. This is due to the relative importance of hemispherical diffusion mentioned above for geometries with aspect ratios close to 1. From these four sample geometries we can conclude that the dimensionless parameters *R* and *Z* by themselves are not enough to completely describe the current responses, and that knowledge of the actual geometry from which they arise is important to understand and predict the behavior of these systems.

2.3. Fabrication of electrodeposited gold fully-conducting micropillar array electrodes

Fully-conducting micropillar array electrodes were fabricated in a class 100-10,000 cleanroom, class 100 for the working areas and class 10,000 for the service areas, using silicon micromachining techniques explained in the introduction of this thesis.

2.3.1. Microfabrication process

Figure 23 summarizes the fabrication process used to produce micropillar arrays by gold electroplating. First of all a n-type silicon wafer was chosen as substrate of the electrodes (a). A 1 µm thick thermal oxide layer $Si0_2$ was grown over 4 inch silicon wafers to provide electrical insulation to the electrode structures (b).

Next, gold electrodes were produced through a combination of metallization and photolithographic steps. The electrodes were defined by lift-off using Clariant's inversion photoresist AZ-5214E (c). Following the lithographic step, the wafer was metallized by dc-sputtering with a layer of Ti (25 nm), Ni (25 nm) and Au (125 nm) (d). Titanium acted as adhesion promoter for the other metals, and nickel was used as a diffusion barrier to avoid the formation of Ti/Au alloys during the step of passivation deposition.

Following the metallization, the wafer was immersed in an acetone bath to remove the resist and lift-off the unwanted metal. Next, the wafer was passivated by PECVD in an Oxford Instruments PlasmaLab reactor by deposition of a double layer of silicon oxide followed by silicon nitride (e). This passivation layer was 1 µm thick, and had a double purpose. It protected the contact lines between the electrodes and the contact pads, and defined the electrode areas.

The passivation was opened by reactive ion etching, RIE, after a second photolithographic step (f). To ensure that all silicon oxide had been removed from the gold surface, the wafers were immersed for 20 seconds in a Sioetch MT 06/01 solution (BASF) where any remaining silicon oxide was completely removed from the gold surface. This completed the fabrication of flat gold disk electrodes, and represented the starting point for the production of these conducting pillar electrodes.

The first step in the construction of the microcylinders was the preparation of a suitable template. This was done in a photolithographic process using a 17 µm-thick layer of positive photoresist AZ-4562 (g). 10 and 20 micron round wells were defined in the resist after insolation through a dark field mask and subsequent resist development. To ensure good electrical contact between the gold at the bottom of

these templates and the plating solution, the wafers were treated in a 300 W oxygen plasma (TEPLA 300E, Techics Plasma

GmbH) for 30 seconds. This plasma treatment removed any traces of resist contamination remaining on the gold after development. The last step was the growth of gold microcylinders by electrodeposition (h). A gold cyanide-based commercial bath from Enthone-Omi (Pur-A-Gold) was used for the electrodeposition of gold micropillars. The bath is formed by an electrolyte and a double potassium and gold cyanide complex. The wafer was placed on a wafer holder with front contacts made in AMMT (Advanced MicroMachining Tools) to protect its back-side and achieve a homogeneous current distribution during plating. Note that because pillars are grown electrochemically on all the disk electrodes spread throughout the wafers, it was necessary to design a layout that connected all the working electrodes to a large current collector located around the wafer edge. However, the electrodes were later independently addressable on the chip because these contact lines were cut on dicing the wafer.

Gold electrodeposition was carried out using an Autolab PGSTAT302N potentiostat/galvanostat. The process was performed at room temperature and at a pH of 7.0. A magnetic stirrer was used to keep a homogeneous composition in the plating bath. A fixed current density of 1,3 mA/cm^2 was applied during the process. Gold net (99.9% Goodfellow, UK) was used as a counter electrode, in a 2-electrode configuration, with the wafer acting as the cathode. The grown rate was 1000 Å/min, so the process would typically run for 75 minutes (4500 seconds) to obtain a 7.5 µm gold layer.

The fabrication was complete after the resin was stripped from the wafers in an acetone bath, and a final oxygen plasma treatment was applied to remove any traces of resist left (i).

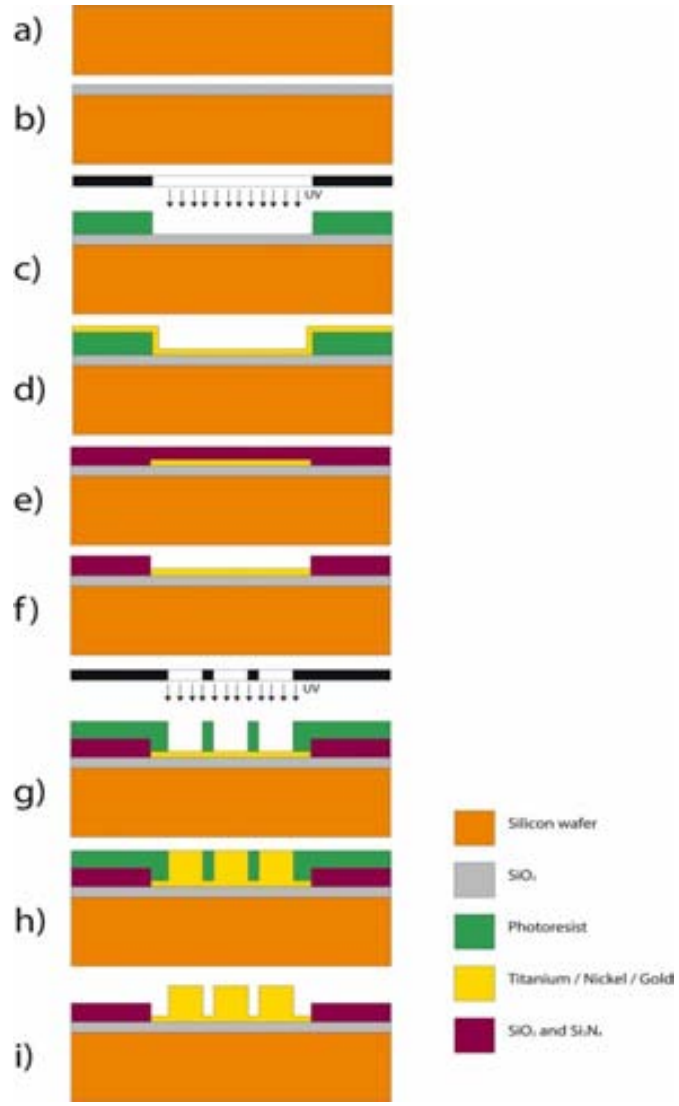

Figure 23. Electrodeposited gold micropillar array electrodes fabrication process.

2.3.2. Physical characterization

The resulting micropillar array electrodes were characterized using different physical techniques. Scanning electron microscopy, SEM (LEO 1530 Carl Zeiss) was used to verify if the surface was totally metallized. Besides, to determine the homogeneity of the process across the entire wafer surface, profilometry measures (Veeco Dektak 150) and confocal images (PLμ 2300 Sensofar) were taken. All of these data from the surface provide useful information about the geometrical parameters in each one of the fabricated micropillars.

Profilometric and confocal measurements ruled this out as they showed that the pillars were shorter than the thickness of the resist layer, and that their height was very similar throughout the wafer, presenting typical standard deviations around 2 μm. Pillar height was controlled by the thickness of the resist layer used as template and by the charge passed during electrolysis. We produced pillars of different heights, ranging

from 5 to 15 µm to avoid overflowing the resist used for molding, which was 17 µm thick. The differences in cylinder diameter were more likely due to a combination of problems in the lithographic step, and in the wafer cleaning step before electroplating, and resulted in pillars which radius was bigger than initially planned, or in pillars that resembled inverted cones. The cleaning step before electrodeposition consisted on a mild oxygen plasma treatment. This oxygen plasma is known to etch the photoresist isotropically, so all the structures should have been etched to a similar extent. However, the plasma inside the reactor is inhomogeneous, and although a mild power was used for a brief period of only 30 seconds, the wafer areas exposed to more active plasma regions suffered a lateral over-etching that then led to bigger cylinders. Thus, while most of the cylinders kept close to the nominal diameter sizes of 10 and 20 microns, cylinders up to 40 microns in diameter could be found in certain areas.

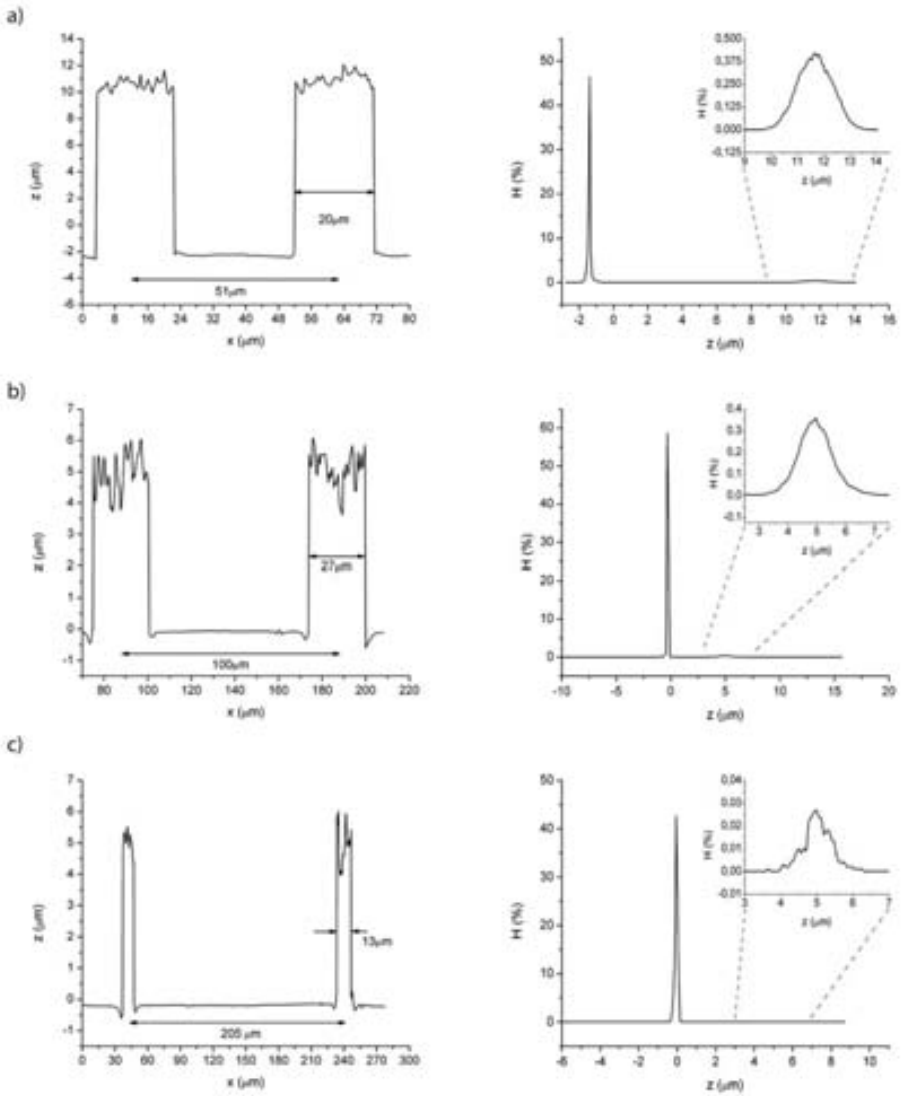

Figure 24. Confocal microscopy measurements of electrodeposited gold micropillar array electrodes.

One interesting feature revealed by profilometry is the difference in surface roughness between the electrode surface on the original gold electrode, which is basically flat, and the top-side of the pillars, which appears very rough. This is shown in the profilometries in Figure 24.

On the other hand, it was very difficult to infer much about the roughness of the side walls from profilometric measurements, and SEM and FIB were used to look at the cylinder side walls and tops in more detail. The next pictures in Figure 25 are electron microscopy image of a focused ion beam cut showed that the cylinders' side walls are flat and smooth, which means that the plating solution penetrated and wetted the photoresist template adequately.

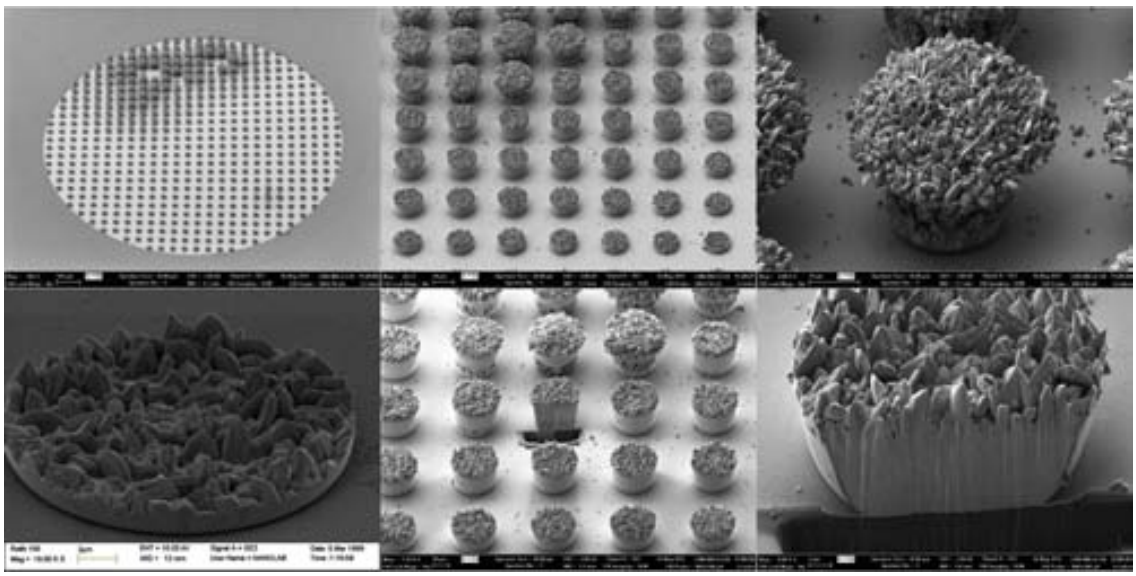

Figure 25. SEM images of a electrodeposited micropillar array electrode and a FIB cut of one micropillar.

This figure also shows that the interface between the pillar and the underlying gold surface is very tight, to the point where the two materials are nearly indistinguishable from each other, and that the gold inside the cylinders is very dense. Figure 25 also shows that the walls of the pillar present a slightly negative slope. That is, they are smaller at the base than they are at the top. This kind of profile is consistent with the use of a positive photoresist as a template. In a positive photoresist, the photoactive compound makes the parts exposed to UV light more soluble in the developer solution. As the light goes through the resist, the resist closer to the photomask is exposed longer than the resist directly in contact with the substrate. During this time of exposure, the photoactivated compound diffuses away from the illuminated areas into the dark ones. Under standard conditions this does not represent a problem because resist thicknesses between 1 and 2 microns are used, and exposure times tend to be very short. In the present case a resist layer 17 microns thick was used, which required longer exposure times. The result is that, when the resist is developed,

the features defined by the resist can be bigger at the top than at the bottom. With the exception of lift-off processes, the profile of the resist does not necessarilly matter but, in the present case the result of the lithography has a clear impact on the geometry of the resulting microstructrues because the resist was used as a template. The third observation from the SEM images is that the top sides are composed of gold crystallites growing with no apparently preferential direction. The size of these microcrystals is controlled by the current density used to grow the cylinders, although an in-depth study on the effect of current density is beyond this work. The increased roughness made the cylinders look darker under the optical microscope, but this was not noticeable electrochemically.

2.3.3. Cyclic voltammetry

The micropillar aray electrodes were electrochemically characterized using a solution 2 mM of potassium hexacyanoferrate (≥98.5%, Sigma Aldrich) prepared in potassium nitrate 0.5 M (≥99.0%, Sigma Aldrich). Before starting any experiment the micropillar electrode under study was previously purged with N_2 gas to remove oxygen from the solution. An electrochemical analyser (Autolab) was used to do chronoamperometries and cyclic voltammetries in a three-electrode configuration, using an Ag/AgCl reference electrode (Metrohm) and a Pt auxiliary electrode (Metrohm) inside a Faraday cage.

The voltammetry of microcylinder array electrodes differs very little from that of planar macroelectrodes at slow and moderate scan rates. Figure 26 shows experimental I_p vs. $\upsilon^{1/2}$ plots for three different micropillar densities, where the data are plotted along the theoretical current predicted by the Randles-Ševčík expression. The pillars on the electrodes used in in these experiments are 10 µm radius, but present distances of 50, 100 and 200 µm between them. This figure shows that, (i) in all cases the voltammetric peak currents at low scan rates tend toward the planar electrode values, and (ii) that as scan rate is increased, the current observed at the micropillar array electrodes deviates from planar behavior. This deviation in behavior from the flat electrode becomes more significant as pillar density and pillar height increase.

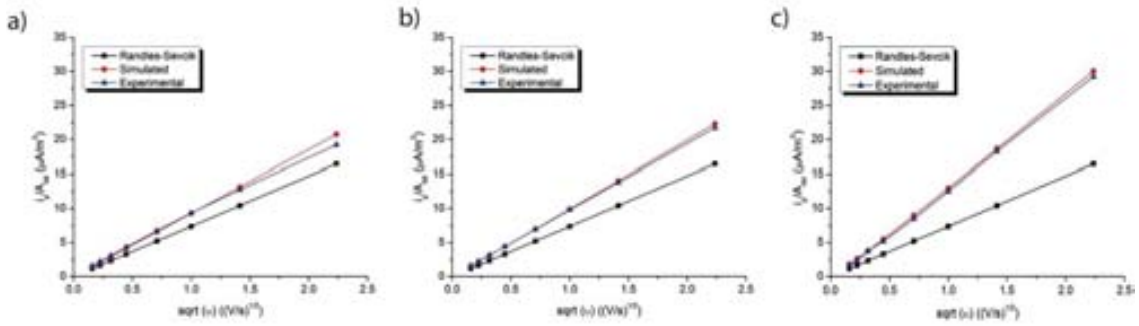

Figure 26. Peak current density as a function of the square root of scan rate for electrodeposited gold micropillar arrays for three different densities, d=200 µm (a), d=100 µm (b) and d=50 µm (c).

The data in Figure 26 shows that as the number of microcylinders per unit area of electrode decreases, it becomes virtually impossible to tell whether there are any micrometric 3D features at all on the electrode surface, even at the faster scan rates studied. This is because the surface area of the pillars, relative to the surface area of the entire electrode, is so small that the pillars contribute too little to the overall current compared to the conducting plane surface around them, which masks their presence. In the case of more densely populated micropillar arrays, the actual surface area of the electrode is bigger than the projected area, and most of the current is

collected at the microcylinder surface, so the observed current is greater than in the planar electrode case as long as the diffusion layers of adjacent pillars do not overlap.

2.4. High Aspect Ratio (HAR) gold fully-conducting micropillar array electrodes

The second method used for the fabrication of fully-conducting micropillar array electrodes is based on the combination of silicon patterning by dry etching and its metallization using also gold as electrode material. This process is explained next, and Figure 27 shows the summary of the fabrication process. These electrodes were also microfabricated in the IMB-CNM cleanroom.

2.4.1. Microfabrication process

An n - type one side polished silicon wafer was used as electrode support. It was previously cleaned with deionized water to eliminated particles (a). Next, 0.4 µm of Al/Cu metal layer were deposited on the wafer by dc - sputtering (Leybold - Heraeus Z - 550) to act as mask for future DRIE (Deep Reactive Ion Etching) steps (b).

The different micropillar arrays were defined by photolithography using a 2 µm positive resist (HiPR - 6512) spin coated on the wafer (c). A wafer aligner - insolator (Canon PLA - 600F/FA) was used to transfer the design from a bright-field Soda-Lime Cr photomask (Deltamask, NL) to the photoresist after developing the photoresist, to which the design of the electrode arrays were transferred, the Al/Cu layer was wet etched from all the places where photoresist was not present (d), which was in the

areas between micropillars. Next, the remainder of the photoresist was also removed in an acetone bath and leave the Al/Cu layer acting as the sole mask during the following steps of the process (e).

Micropillars were created using the Bosch method, [43, 50] which consists in the sequential etching of silicon, leading to controllable and stable lateral profiles, high etch rates and high selectivity. The Bosch method is a type of DRIE time – multiplexing alternating process which splits the process of removing material from a substrate in two phases: etching and polymerization, allowing the creation of HAR microstructures. The polymerization step offers protection to the sidewall, while the etching process removes substrate material from unmasked areas. Lateral etch contribution must be strictly controlled to achieve the highly anisotropic profiles. For this reason, different parameters affecting process performance such as pressure, gas flow rate, and power were optimized and tailored to obtain the best results for our application. Etching and passivation steps are alternated until the desired etching depth is reached, and the process time for each step is balanced to achieve the desired anisotropic profiles. Our process for fabricating micropillars was developed using a

RIE chamber (Alcatel 601 - E) where SF_6 working as etching gas, and C_4F_8 working as passivation gas, were pumped under this conditions (P = 4.5 – 7.5 Pa, Φ = 175 - 275 V, Q_{SF6} = 325 - 350 sccm, and Q_{C4F8} = 175 - 250 sccm). The overall time of the process depended on the desired height of the micropillars. The longer the process, the taller the resulting structures (f).

Table 9. DRIE process time according to the heigh of the micropillars.

$h_{\mu Pill}$ (μm)	Process time (min)
5	80
25	390
50	661
125	1685

After creating micropillars, the masking Al/Cu metal layer was also removed, this time immersing the wafers in a piranha solution for 15 minutes. RCA cleaning (H_2O : H_2O_2 : NH_4OH (5:1:1) for 10 minutes and H_2O : H_2O_2 : HCl (6:1:1) for 10 minutes) was applied to eliminate organic and metallic traces on the silicon to ensure good future processes. After rinsing the wafers in DI water, they were dried using a hot plate instead of using the usual processes based on high speed rinsing and ultrasounds to avoid the destruction of the microstructures. After the micropillars were fabricated, a layer of thermal oxide (1 μm) was grown to provide enough electrical isolation between the final electrodes and the wafer (g).

Last, 50 nm of titanium (P = 1000 - 1500 W, Q = 30 – 40 sccm, P = 5 – 15 mT), to enhance adhesion, 150 nm of nickel (P = 1000 - 1500 W, Q = 30 – 40 sccm, P = 5 – 15 mT), to avoid Ti - Au alloy formation, and 150 nm of gold (P = 500 - 750 W, Q = 25 – 35 sccm, P = 5 – 10 mT), were deposited on the SiO_2 surface of the micropillar arrays by dc – sputtering (MRC - 903) (h). The use of sputtering instead of e-beam or thermal evaporation ensures the metallization of the micropillar vertical walls down to their base.

The encapsulation of each electrode is formed by two components. A thin Cu wire was pasted using silver epoxy (RS Amidata, ES) to provide electrical contact between the electrode and the contact pad of a print-circuit board. Photocurable resist (Epotek OG147-7), cured in a UV flood lamp (Dymax 5000 - EC), was used to isolate the contacts and define active areas.

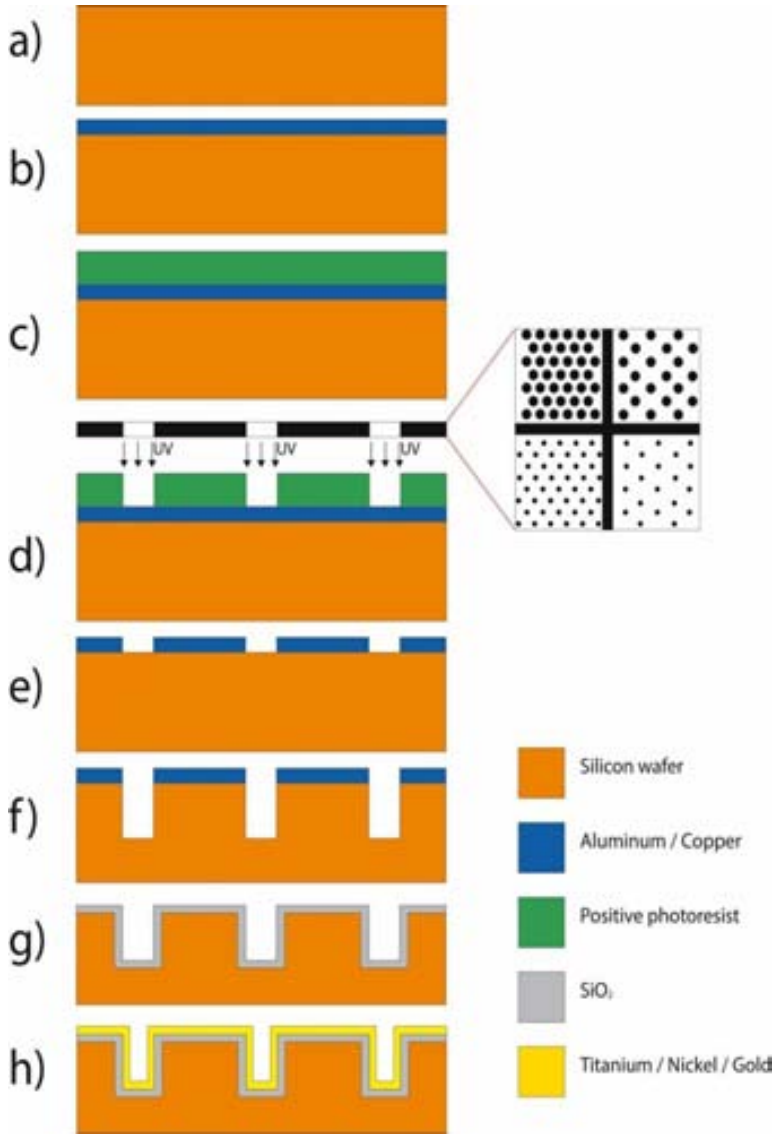

Figure 27. Fabrication process of gold fully-conducting micropillar array electrodes by DRIE and dc-sputtering metallization.

2.4.2. Physical characterization

The resulting micropillar array electrodes were characterized also using SEM to verify the correct metallization over the entire micropillar height. Figure 28 shows SEM images of a series of different micropillar array electrodes.

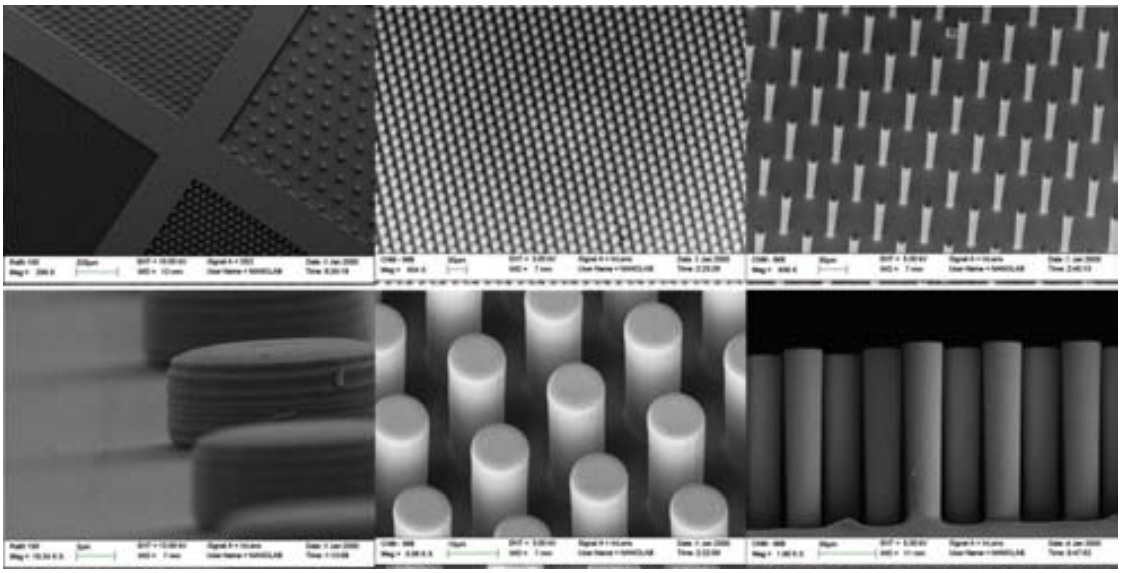

Figure 28. SEM images of several fully-conducting micropillar array electrodes.

To determine the homogeneity of the process across the entire wafer surface, profilometry measurements and confocal images were taken as well. The data from these measurements provided useful information on the geometrical parameters in each of the fabricated micropillar arrays.

We noticed slight variations in micropillar height across the wafer. The resulting heights depended on the position within the wafer and on the separation distance between micropillars. Micropillar radius, on the other hand, was the same as defined in the original photomask layout design. Figure 29 presents histograms showing the actual sizes of the micropillars obtained in 4 different wafers.

These deviations from the nominal values shown in Table 7 forced us to adapt the simulations to the actual micropillar sizes and facilitate comparison with the experimental results. Finally, optical microscopy (Leica DM4000) was used for measuring with high accuracy the active area of each electrode, which we then used to report current densities.

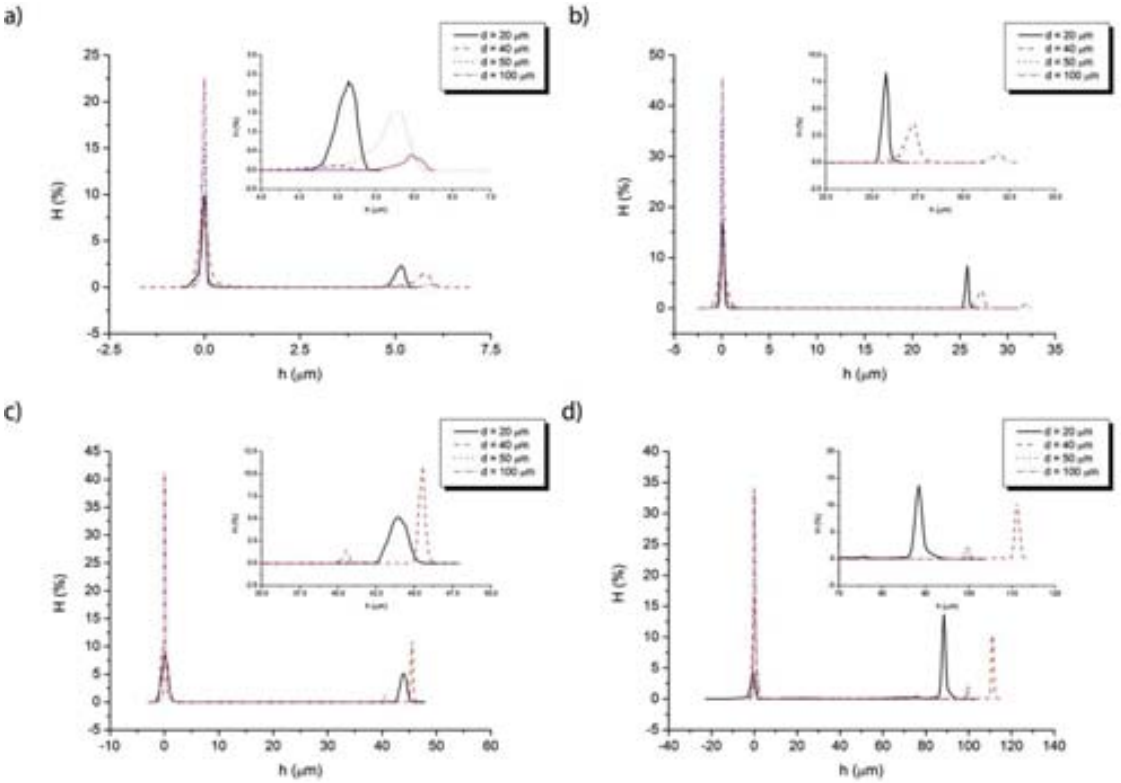

Figure 29. Histograms showing the average height of the micropillar array electrodes.

2.4.3. Experimental section

2.4.3.1. Potential step experiments

Some of these micropillar structures, particularly the most densely populated by tall micropillars, needed to be immersed in isopropanol for one hour prior to the electrochemical experiments. Isopropanol has a lower surface tension than water, so it penetrates into the structures more easily. Once the space between micropillars is filled with isopropanol, the chips are transferred into the aqueous solutions, where the alcohol mixes with water and is eventually totally replaced by it.

Figure 30 compares theory and experimental results obtained from 8 of the different microfabricated micropillar arrays described in Table 7. The figures show slight discrepancies arising between experimental and simulated current densities at short and long times, but excellent agreement in the magnitude of the current densities, and particularly in the transition between planar diffusion regions. While the differences between experimental and simulated currents at short times are due to charging currents that are not considered in the simulations, it has not been possible to attribute the mismatches at longer times to a specific phenomenon.

The experimental currents show that the micropillars have been completely metallized, as already suggested by the SEM images, and that they can be used as working electrodes.

Note that the most suitable geometry will be dictated by the final application. For instance, micropillar arrays destined for fuel cells may be different from arrays used in electroanalytical applications. Arrays with very high aspect ratio may be better suited for electroanalysis since they observe higher currents shortly after the potential step, but they are able of sustaining those high current levels for an only short period of time. This may be sufficient to achieve very high sensitivities using potential pulse techniques.

On the other hand, a fuel cell may benefit from using lower aspect ratio micropillars and, even if the current output is lower than for taller arrays, they will be able to sustain their maximum current levels longer as the fuel can access the entire surface more easily. These are just examples of why one would choose one design or other. Chapter 4 will illustrate this point in the case of miniaturized microbial fuel cells.

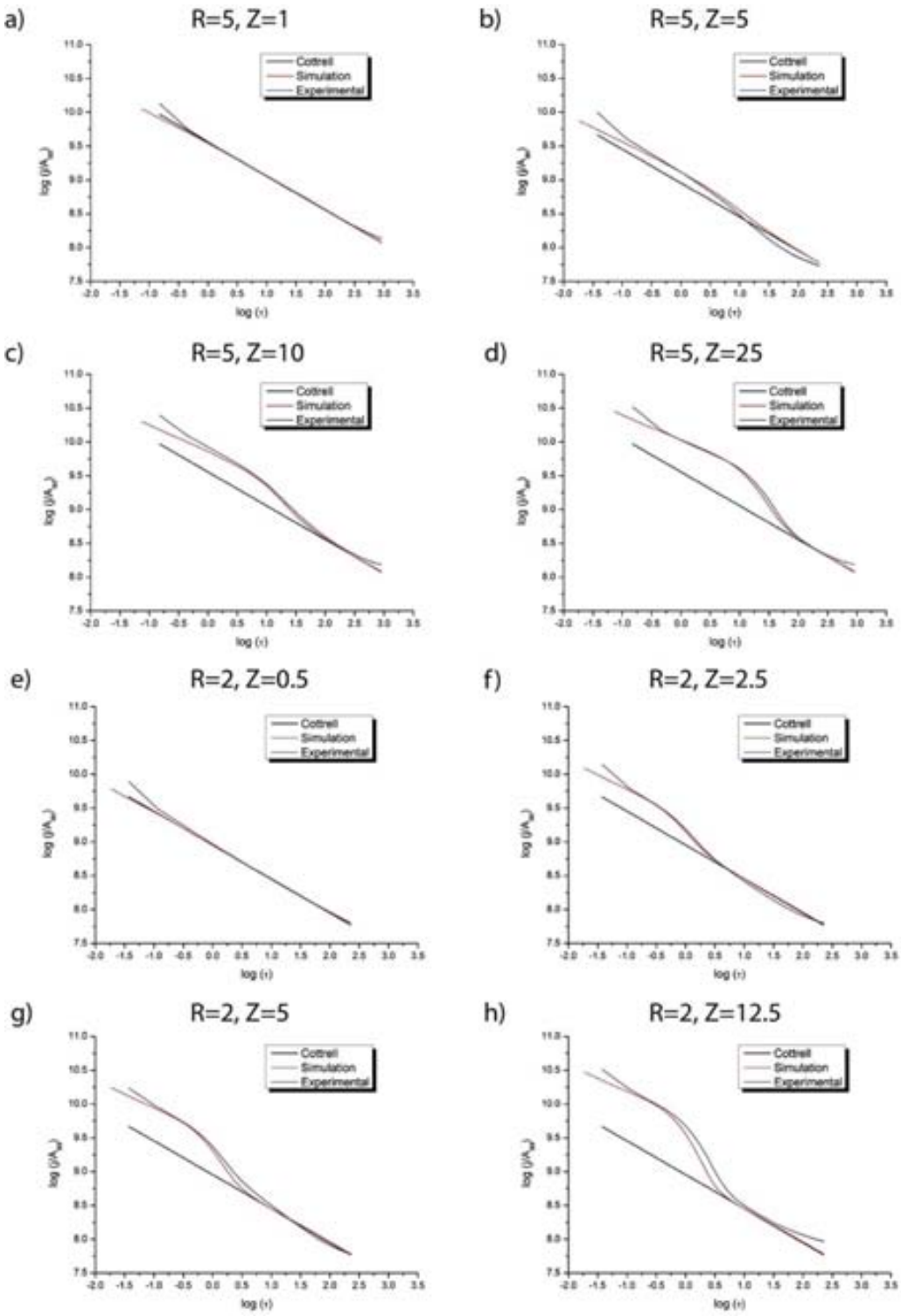

Figure 30. Experimental and simulated transient current densities for gold fully-conducting micropillar array electrodes and flat electrode.

2.4.3.2. Cyclic voltammetry

Figure 31 shows some experimental cyclic voltammograms recorded at four different micropillar array electrodes at scan rates ranging from 5 mV/s to 200 mV/s.

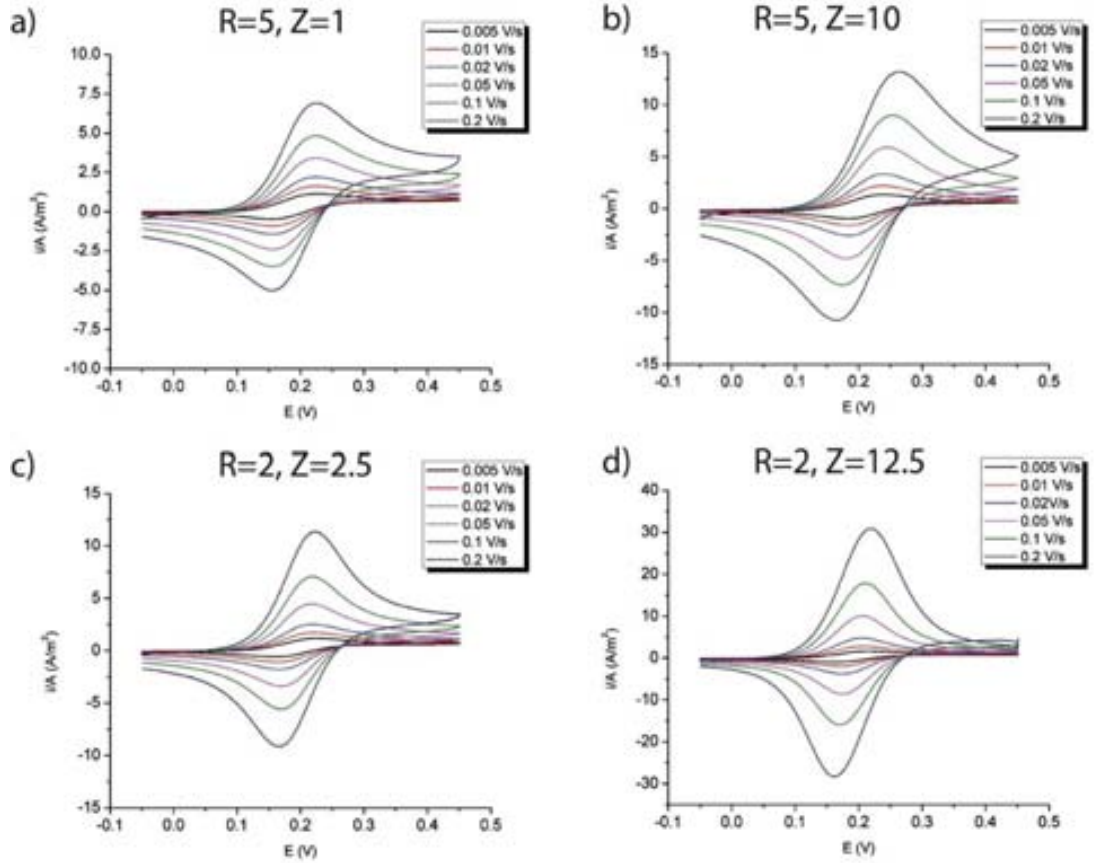

Figure 31. Cyclic voltammetries for different geometries and ranging some scan rates.

The most obvious effects of pillar size and density are an increase in the peak currents and a narrowing of the peak-to-peak potential separation. The current densities displayed in the figure have been calculated dividing the current by the area taken by the array, rather than the actual surface area of each electrode. So for a given surface area, arrays with a constant density but with taller pillars present larger currents, and higher pillar densities also lead to higher currents for a given micropillar size. But what is more interesting about these devices is how the presence of micropillars affects the shape of the voltammograms, narrowing the potential peak-to-peak separation. This has been predicted by Henstridge et al. [94, 95], and is due to a thin layer effect caused by the rapid depletion of the material between neighboring micropillars. This thin layer effect is also manifest in chronoamperometry, shortly after a potential step, as a region of high current density followed by a decay that leads to a second region controlled by planar diffusion.

Figure 32 shows i_p/A_{dd} vs. $\sqrt{u}$ plots for 8 different micropillar arrays. Here we compare the results from cyclic voltammetry experiments in 2 mM ferrocyanide solutions and

from finite-element simulations, and with the case of a planar electrode. For array electrodes with low micropillars or sparsely populated arrays, the current density increases compared to the planar electrode case described by Randles–Ševčík's equation over scan rates up to 5 V/s (Figure 32.a). The results displayed in this figure show that the peak current tends toward the planar electrode case at slower scan rates because the pillars are actually masked by the diffusion layer that develops on top of them. In other words, at slow scan rates, the diffusion layers around the pillars overlap and the only possible access of fresh material to the array is from the top, and the response of the array becomes similar to that of a planar electrode of the same size as that of the array. This is analogous to what happens at microelectrode arrays at equally long timescales.

On the other hand, as scan rate increases the diffusion layers at the sidewalls of neighboring pillars no longer overlap, and the pillars become fully visible in the voltammetry. Diffusion becomes planar over the surface of the pillars, and the current is therefore proportional to the real surface area.

Note that if the current densities were calculated using the real surface area instead of the projected area, these plots would merge with the prediction of Randles-Ševčík's equation, except for deviations appearing at intermediate scan rates at which the degree of depletion of material confined between micropillars is such that it allows radial diffusion to operate (leading to higher current densities). Overall, planar diffusion dominates the transport of electroactive species to micropillar array electrodes.

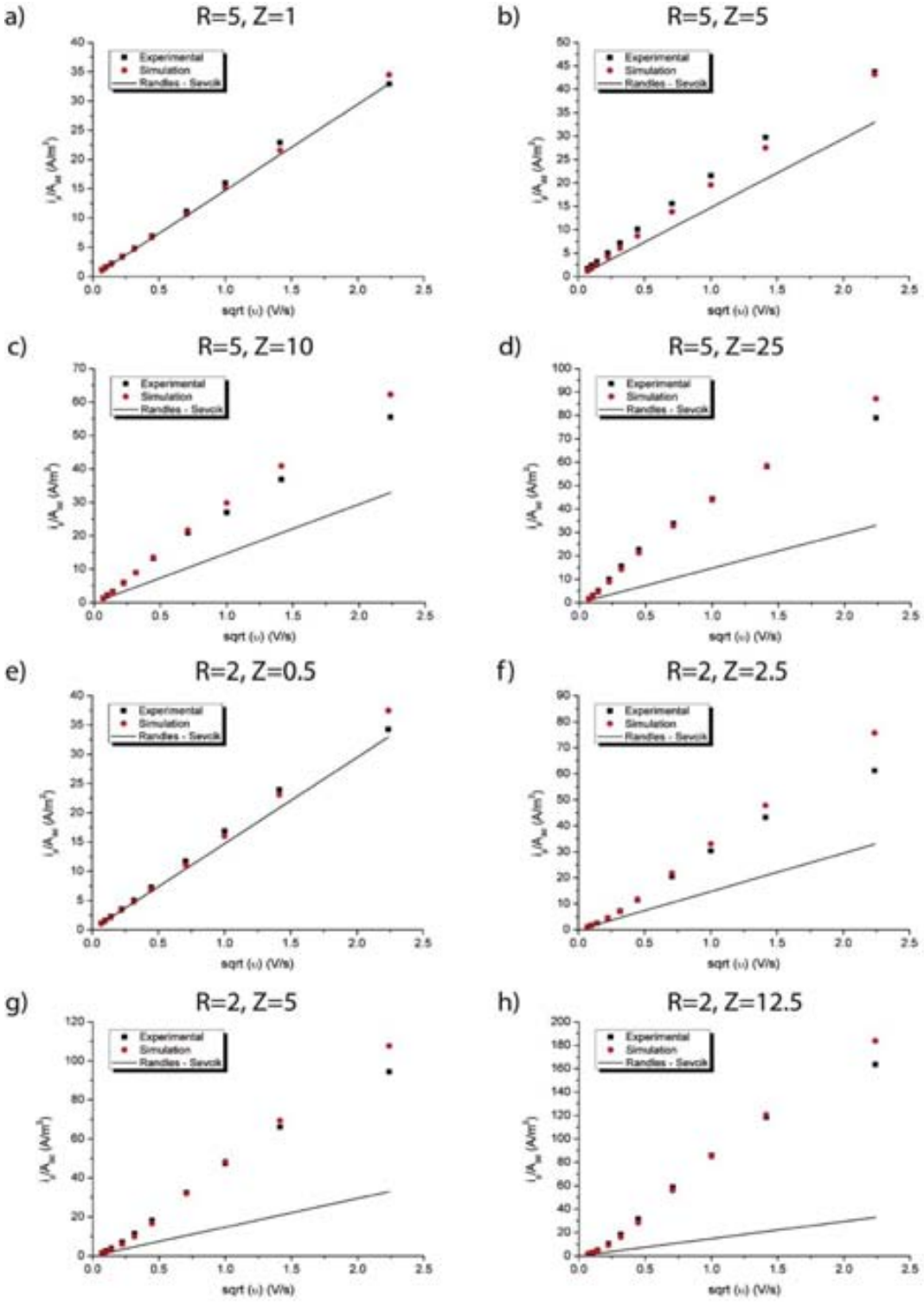

Figure 32. Peak current density as a function of the square root of scan rate for simulated and experimental cyclic voltammograms, and Randles-Ševčick equation prediction.

Note that, also in Figure 32, the experimental peak current values are systematically lower than the simulated values at the higher scan rates, although at lower scan rates the experimental and simulated values are almost identical. This is because our simulations assumed fast electrode kinetics, so that only mass transport effects could

be seen. However, in reality electron transfer at our micropillar array electrodes should be considered quasi-reversible. To show this, we determined the heterogeneous electron transfer rate constant, k^o, using a planar electrode fabricated by the same processes and conditions as in the case of the micropillars. We performed a series of cyclic voltammetry experiments within the same scan rate range as that used with the micropillar arrays, and plotted the peak-to-peak separation vs. the scan rate. These results are given in Figure 33. At low scan rates, this ΔE_p remains close to 70 mV. This is already 13 mV away from the theoretical 57 mV predicted for a fully reversible electrochemical process, but remains constant up to a scan rate of 100 mV/s. For higher scan rates, ΔE_p grows linearly wilt $\log_{10}$ (υ).

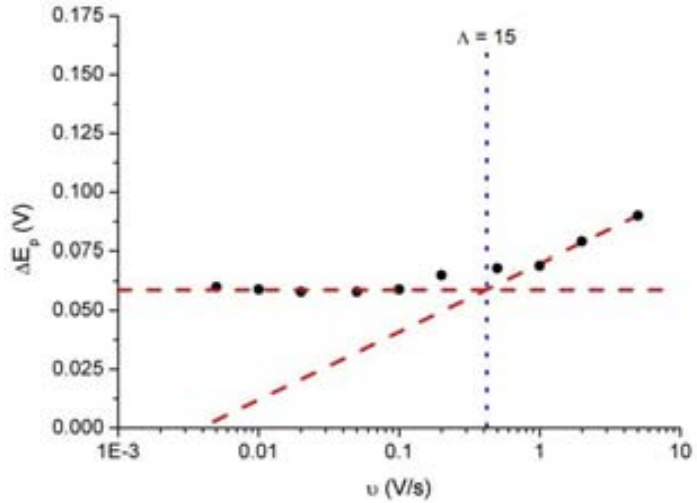

Figure 33. Variation of peak potential separation with scan rate for a flat electrode fabricated using the same processes as for the micropillar array electrodes. The auxiliary red dashed lines facilitate the identification of the transition between reversible and quasi-reversible electrode kinetics.

Using Matsuda and Ayabe's approach (27), we can use the transition scan rate to estimate the electron transfer rate constant:

$$\Lambda = \frac{k^o}{\sqrt{FD\upsilon/RT}} \tag{27}$$

Where Λ is a dimensionless parameter that reflects the kinetics of the electrode process. The transition between reversible and quasi-reversible kinetics occurs when Λ = 15 [96]. According to this, in our case k^o = 0.01 cm·s^{-1}. To understand this figure, we compared it to the value of the mass transport coefficient, m_T, for the slower and for the faster scan rates used.

$$m_T \sim \sqrt{\frac{D}{(RT/F\upsilon)}} \qquad \begin{matrix} k^o \gg m_T\ (Reversible) \\ k^o \ll m_T\ (Irreversible) \end{matrix} \tag{28}$$

In our case, $m_{T\,(5\ mV\cdot s\text{-}1)} \approx 10^{-3}$ cm·s^{-1} and $m_{T\,(5\ V\cdot s\text{-}1)} \approx 0.036$ cm·s^{-1}. These values show that our electrode material fails to meet the reversibility criterion for the faster scan rates used. Therefore the ΔE_p is systematically larger than for the simulated cases, and the experimental peak currents are consequently slightly lower than the simulated ones. Hence, at faster scan rates, the experimental voltammograms are expected to show slightly smaller currents and wider peak-to-peak separations.

Figure 34 shows ΔE_p vs. $\log_{10}(\upsilon)$ plots for different micropillar array geometries. These figures show the experimental ΔE_p measured from cyclic voltammetry experiments (using ferrocyanide solutions), and simulations assuming fast electron transfer kinetics. The horizontal dotted lines signal the 60 mV level. In all cases the experimental ΔE_p is larger than the simulated ones because our electrode material displays limited electron transfer rates to ferrocyanide at moderately fast scan rates. In all cases, ΔE_p increases with scan rate as expected for our electrode material, and at the faster scan rates studied the peak-to-peak separation exceeds 100 mV. The results shown in Figure 34*.a and 34.c* resemble the planar case throughout the entire range of scan rates studied. This is because the pillars in them are not very high and, on top of that, in cases *a* and *b* the arrays are not very densely populated either.

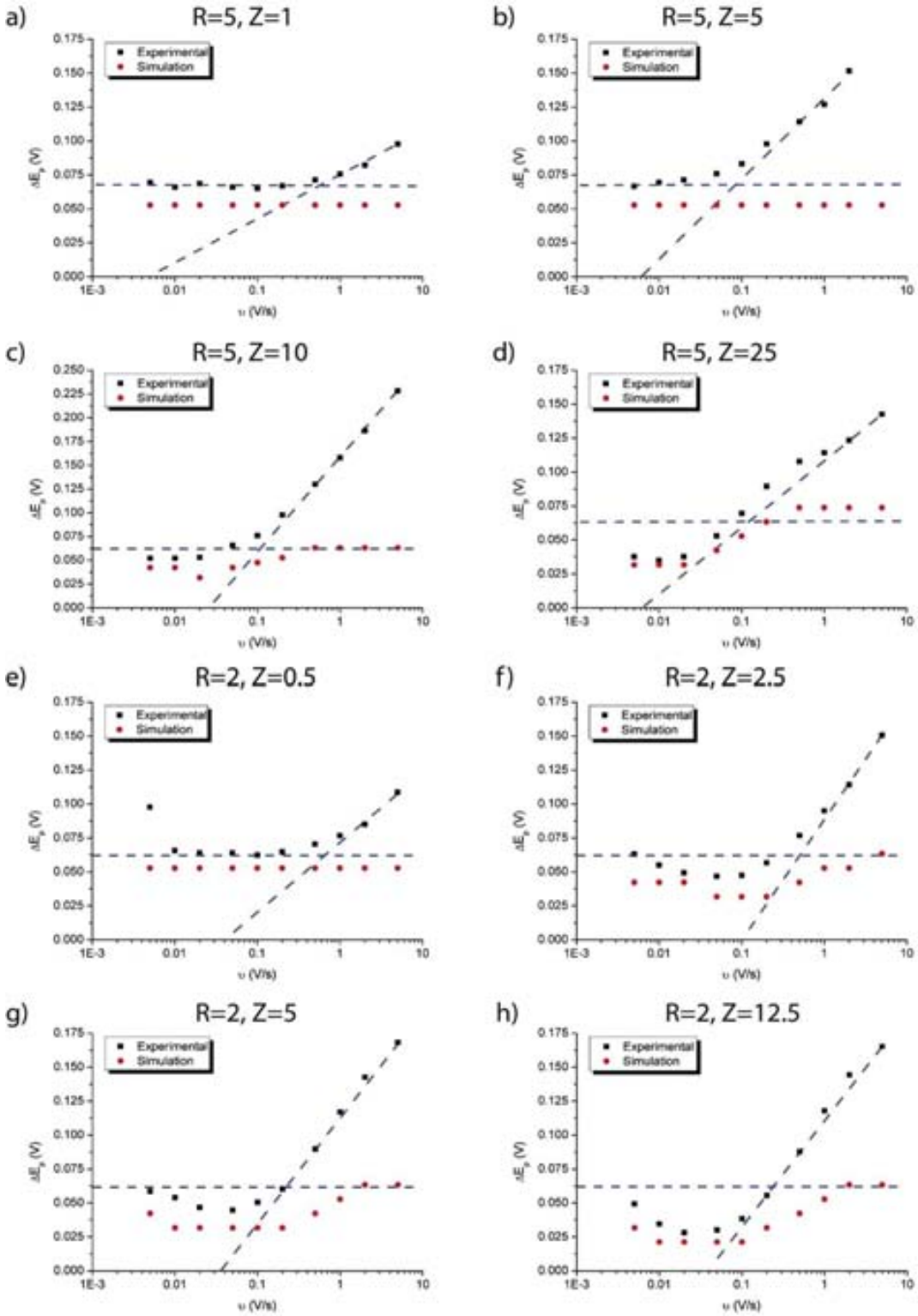

Figure 34. Peak potential dependence with scan rate for different micropillar array geometries.

However, for the rest of the array geometries, the peak-to-peak separation obtained at scan rates below 200 mV/s dips below the theoretical 57 mV, expected for diffusion controlled processes at planar electrodes. The explanation for this effect, which was already predicted by Henstridge et al. [94, 95] and in the section 2.2.4.1, can be found

as in the case of the potential step experiment, examining the concentration profiles obtained from simulation.

In short, the reason for this voltammetric shape and the smaller ΔE_p values is a thin-layer effect brought about by the rapid depletion of electroactive material confined in the small volume between micropillars. At both very slow and very fast scan rates, the current is controlled by planar diffusion and the ΔE_p at the micropillar arrays is the same as in the planar electrode case. At slow scan rates, not only the material confined between micropillars is effectively depleted, but also a significant diffusion layer develops over the surface of the array, masking the presence of the pillars. Note that in this case the concentration profiles run parallel to the surface of the array. At the other end, under very fast scan rates, the concentration profiles run parallel to the surface of the micropillars and the penetration of the diffusion layer of the array into the solution bulk is not very deep. The intermediate cases, where the dips in Figure 34 occur, need more attention. At these scan rates, the concentration profiles show that the main contribution to the current comes from the depletion of the material confined between micropillars, even if an otherwise significant diffusion layer develops into the solution bulk. The rapid depletion of the material confined between pillars causes the current to increase and decay very rapidly, leading to the appearance of sharp peaks that mask the contribution of the bulk solution. For a given micropillar density, increasing micropillar height exacerbates this effect. On the other hand, the effect of radial diffusion at micropillar tops is even harder to notice from the shape of the voltammograms than it was through the Randles-Ševčík analysis of peak current density.

2.4.3.3. Wetting problems in micropillar array electrodes

This closing section addresses a different kind of practical question, which is whether there is a limit in terms of micropillar height and density that can be used to perform electrochemical measurements in particular and, perhaps, wet chemistry experiments in general.

Figure 35 shows results from chronoamperometric and cyclic voltammetry experiments at an array very densely populated by tall micropillars (R = 2 and Z = 25; where $r_{\mu Pill}$ = 5 µm, d = 20 µm and $h_{\mu Pill}$ = 125 µm), and allow comparison with theoretical predictions from simulations.

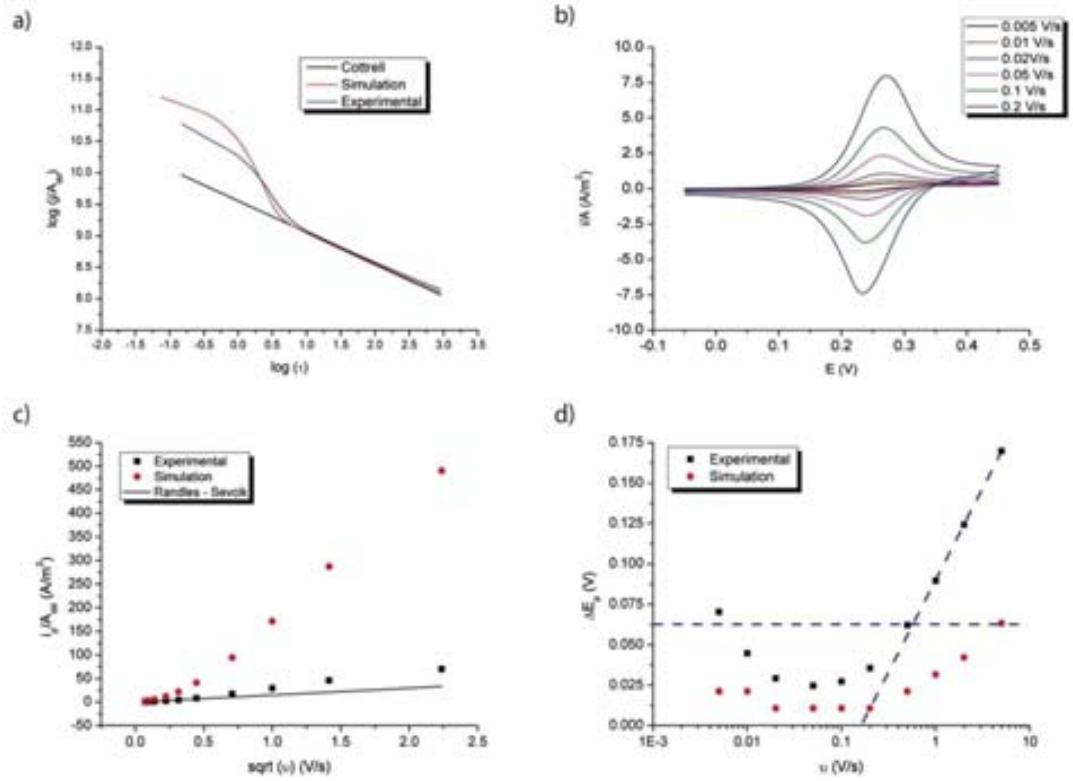

Figure 35. Simulated and experimental chronoamperograms and cyclic voltammograms for the geometry with R=2 and Z=25.

Although SEM images, Figure 28, show that these structures are fully metallized, the experimental currents shown in Figure 35 are well below the theoretical predictions. In spite of this, the presence of micropillars is clearly given away by the dip in the ΔE_p vs. $\log_{10}(\upsilon)$ plot shown in Figure 35.*d*, where ΔE_p values down to 25 mV have been measured. The minimum ΔE_p obtained in the simulations were around 10.5 mV. The reason for the large discrepancies between theory and experiments in this case is simply that, due to surface tension, the solution cannot penetrate through the gaps between micropillars down to their base. Consequently, the active surface area corresponds only to the micropillar surface wet by the solution. Therefore the currents recorded are much lower than expected.

2.5. Conclusions

This chapter presents the fabrication of cylindrical micropillar array electrodes using a combination of silicon micromachining techniques in a cleanroom, and the characterization of these electrodes using a range of microscopy-based techniques, profilometry and chronoamperometry and cyclic voltammetry of ferrocyanide. In addition, we have used finite-element method simulations using a commercial software package to aid in the study and interpretation of the experimental data.

This chapter began with a theoretical description of mass transport at fully-conducting micropillar array electrodes. Finite-element methods were used to solve the mass transport equations, based on the diffusion domain approach. These simulations were useful both at the design and the characterization stages, as they served as a base for comparison of the experimental data and also offered important insight into the current response of these devices. The results obtained show that in contrast to planar microelectrode arrays, hemispherical diffusion plays only a very minor role in the mass transport to micropillar array electrodes. Instead, planar diffusion is the main transport mechanism; at short times, planar diffusion to the vertical surface of the micropillars yields very high currents because the micropillars can increase the surface area of the device by up to an order of magnitude. This planar diffusion region is easily observable at short times in chronoamperometry, and affects the shape of cyclic voltammograms. To verify all of these theoretical results several gold fully-conducting micropillar array electrodes were fabricated using silicon micromachining techniques.

After the study of the mass transport to micropillar array electrodes, several micropillar array electrodes ranging the three geometrical parameters which describe them were fabricated using different clean room processes. The first arrays composed by micropillars were fabricated using gold electrodeposition. The voltammetric response of electrodeposited cylinder micropillar array electrodes has been shown to depend largely on pillar geometry and density, as well as voltammetric scan rate. In most cases, the voltammetric response at low scan rates is virtually indistinguishable from that of a flat electrode of the same area. As the scan rate increases and the concentration profiles of the pillars cease to overlap, radial diffusion sets in at the cylinder top edges and then the observed current becomes larger than the planar electrode case. Using this fabrication technique the micropillars present some discrepancies between the design and the fabricated device. Confocal microscopy and SEM images show how the roughness at the top of the micropillars is high, and the diameter and height do not match the design very closely, which means that more work is needed to create better defined electrodeposited micropillars.

To improve the fabrication of gold fully-conducting micropillar array electrodes, to achieve better reproducibility, and also to compare experimental and theoretical geometries, a different approach was taken to fabricate High Aspect Ratio micropillars. This was a combination of DRIE etching and dc-sputtering metallization steps. The physical characterization of the structures created using this method shows how the roughness on the top surface is null and the homogeneity of the height of each microstructure is approximately constant in any point around the wafer, besides SEM images show how the micropillars were completely metallized. This type of fully-conducting micropillars show in chronoamperometry two distinct planar diffusion regions separated by a transition which duration and extent depend on the particular geometric features (*R* and *Z*) of the system. In cyclic voltammetry, micropillars bring about the appearance of sharp peaks in which the peak-to-peak separation is narrower than the usual 57 mV predicted by theory of diffusion-controlled processes at planar macroelectrodes. Planar diffusion also controls the current response at longer times and slower scan rates, only this time transport occurs from the solution bulk towards the top side of the array because the material confined between micropillars has already been depleted. In contrast to planar microelectrode arrays, at which radial diffusion is crucially important, hemispherical diffusion at micropillar array electrodes mostly goes unnoticed, but it is clearly observed in the chronoamperometric data obtained from arrays of relatively low aspect ratio (R = 1, Z = 1).

Micropillar array electrodes may find application in a wide variety of scenarios, both in the areas of electroanalysis and fuel cells. To focus in the real topic of this thesis the application of fully-conducting micropillar array electrodes in microbial fuel cells lies on the large surface areas of these three-dimensional electrodes compared to planar electrodes. It makes micropillar array electrodes suitable candidates for the electrochemical study and application of biofilms because they can probe much deeper than conventional planar electrodes, making it easier to exchange electrons with the bacteria.

Chapter 3. Carbon electrodes based on Pyrolyzed Photoresist Films to detect mercury

This chapter shows the fabrication of PPF disk electrodes for the detection of mercury in aqueous samples. These electrodes were fabricated by the pyrolysis of positive photoresist using a RTP oven. After the pyrolysis, these electrodes were passivated depositing SiO_2 and Si_3N_4 by CVD. After depositing of the passivation layer it was opened by DRIE to define the active windows of these disk electrodes. The experiments were carried out by Square Wave Voltammetry, and the calibration plot showed that the minimum detection limit for this type of electrodes was around 2 ppb of mercury.

The results of this chapter were reported in the following paper, ***D. Sánchez-Molas***, *J. Cases-Utrera, P. Godignon, and F. Javier del Campo, "Mercury detection at microfabricated pyrolyzed photoresist film (PPF) disk electrodes," Sensors and Actuators B: Chemical, vol. 186, pp. 293-299, 2013.* Also, note that I fabricated the PPF electrodes used in the next work, *M. J. González-Guerrero, J. P. Esquivel,* ***D. Sánchez-Molas***, *P. Godignon, F. X. Muñoz, F. J. del. Campo, F. Giroud, S. D. Minteer, and N. Sabate, "Membraneless Glucose/O2 Microfluidic Enzymatic Biofuel Cells using Pyrolyzed Photoresist Film Electrodes " Lab on a chip, 2013*, where a microfluidic enzymatic biofuel cell was fabricated and characterized

3.1. Introduction

Building on the group experience in the fabrication of pyrolyzed photoresist films (PPF), [97, 98] we present in this work the wafer-level fabrication of PPF disk electrodes with special emphasis in a new route to passivate PPF structures consisting of a mixed layer of silicon oxide and silicon nitride [99], and the subsequent patterning of this passivation layer by means of additional lithographic and etching steps.

PPF is an amorphous carbon material closely related to glassy carbon, [100] although it is easier and less costly to produce.[101, 102] PPF emerged as an interesting material for use in the manufacture of integrated circuits (IC) because its precursor photoresist could be easily patterned by lithography, and because its electrical properties can be controlled by the synthetic conditions.[103-105] Ten years later, Whitesides demonstrated the fabrication of carbon microstructures using polymeric precursors and PDMS micro-moulds for application in microelectromechanical systems (MEMS).[106, 107] Around the same time, Kinoshita published the first electrochemical study on PPF electrodes.[108] Those same workers published a series

of works describing electrochemical response of regular interdigitated PPF electrodes which bands were 50 µm wide and 500 µm long. Much smaller interdigitated structures on PPF by direct lithography have recently been reported by Madou and Shin, who have described the fabrication of nanobands that are 300 nm wide separated by a gap less than 2 microns.[109] Already in the 2000s, Madou and McCreery published a series of works on the electroanalytical properties of PPF electrodes.[110, 111]

In general, PPF is synthesised either from positive or negative tone resists, although the pyrolysis of composite materials has recently shown to be feasible too.[112] Positive-tone, phenol-based resins yield more conducting PPF, [104] but negative tone, epoxy-based resins, such as SU-8 allow the fabrication of thicker PPF, and are better suited for the construction of complex 3D structures.[113] Burckel and Polsky have recently described the fabrication of 3D structures using rapid thermal processes, [114] and also have described the conversion of PPF 3D structures into graphene. [115]

The passivation of PPF is a difficult task for three reasons. First, because RTP synthesized PPF structures are much more weakly bound to the silicon wafer than the original photoresist coating.[116] This requires careful wafer handling throughout the process, but particularly during those operations involving immersion in solvents, such as during resist development in lithography, or during rinsing steps. Second, because the smoothness of the PPF surface greatly hampers the adhesion of the passivation layer, making it necessary to pre-treat the surface and, third, because PPF is a low density material that is easily etched by a range of plasmas used in common reactive ion etching (RIE) processes.[117]

Except for a few works [118, 119] where an SU-8 passivation is used to define the active area of an interdigitated microband array and its contacts, and the recent work of Park et al. describing a SiO_2 passivation of PPF,[120] the fact is that the connections of most PPF-based devices reported to date were protected by hand using different resins, introducing additional cost and variability to the fabrication process.

The second part of this chapter demonstrates the application of these PPF electrodes for the detection of mercury down to ppb levels. We chose mercury because it is the most neurotoxic element known, and its detection in natural waters is of great environmental interest. [121] Although mercury is typically detected by atomic absorption-based methods, the availability of portable electrochemical instrumentation enables its detection in the field, mostly using glassy carbon electrodes. Glassy Carbon (GC) is the most common material used as electrode for the detection of metals in solution. The advantages of carbon electrodes compared to other materials such as gold or iridium are its inertness, low porosity, and ease to work

with it,[122-126] all of which result in high reproducibility. In general, carbon electrodes have been used in combination with other materials that facilitate the pre-concentration of mercury and hence reduce analysis time while keeping an adequate sensitivity. In the case of mercury detection, gold nanoparticles deposited on carbon nanotubes [123] have been shown to improve sensitivity, and gold and platinum nanoparticles have been deposited on a nanofiber matrix [127] to achieve high sensitivity and selectivity and a remarkable detection limit of 8 ppt (0.008 ppb). However, standard glassy carbon electrodes require polishing and preparation prior to analysis, and we believe that disposable PPF electrodes can improve current methodologies by reducing the variability associated to these manual operations. We show the suitability of PPF for the fabrication of low-cost sensors, and demonstrate the direct detection of mercury down ca. 2 ppb in aqueous solutions at PPF disk electrodes. These electrodes may be used several times without memory effects.

3.2. Experimental section

3.2.1. Chemicals and instrumentation

Electrochemical measurements were performed using a µ-Autolab - III (Metrohm, NL) with a tree-electrode configuration. The reference electrode was an Ag/AgCl (3M KCl) electrode (Metrohm REF 6.0726.100), and the auxiliary electrode was a Pt ring (Metrohm REF 6.0351.100). The PPF working electrodes were made as described below.

All solutions were prepared using deionised water of resistivity not less than 18 MΩ·cm. Oxygen was purged from the solutions by bubbling N_2 through them for no less than 5 minutes prior to recording voltammetric data. N_2 bubbling was maintained during the mercury electrodeposition step, but not during voltammetric runs. Potassium nitrate (≥98.5%), potassium ferricyanide (99.8%) and nitric acid (65%) were purchased from Sigma-Aldrich. Hg mercury standard for AAS (1000 mg/l) was purchased from Fluka.

3.2.2. Electrode fabrication and PPF synthesis

Figure 36 summarizes the fabrication process of the PPF electrodes, which was as follows: one-side polished silicon wafers were used as electrode substrate. In order to provide electrical isolation between the wafer and the PPF structures, 1 µm of SiO_2 was grown thermally on the wafers prior to any further processing. Next, a homogeneous coating of approximately 20 µm of positive photoresist AZ - 4562 (Clariant, Microchemicals GmbH) was spin coated on the wafer at 1600 rpm. This

seemingly high thickness leads to a final PPF thickness about 3 microns, as the resist loses about 80% of its original volume during pyrolysis. [97, 105]

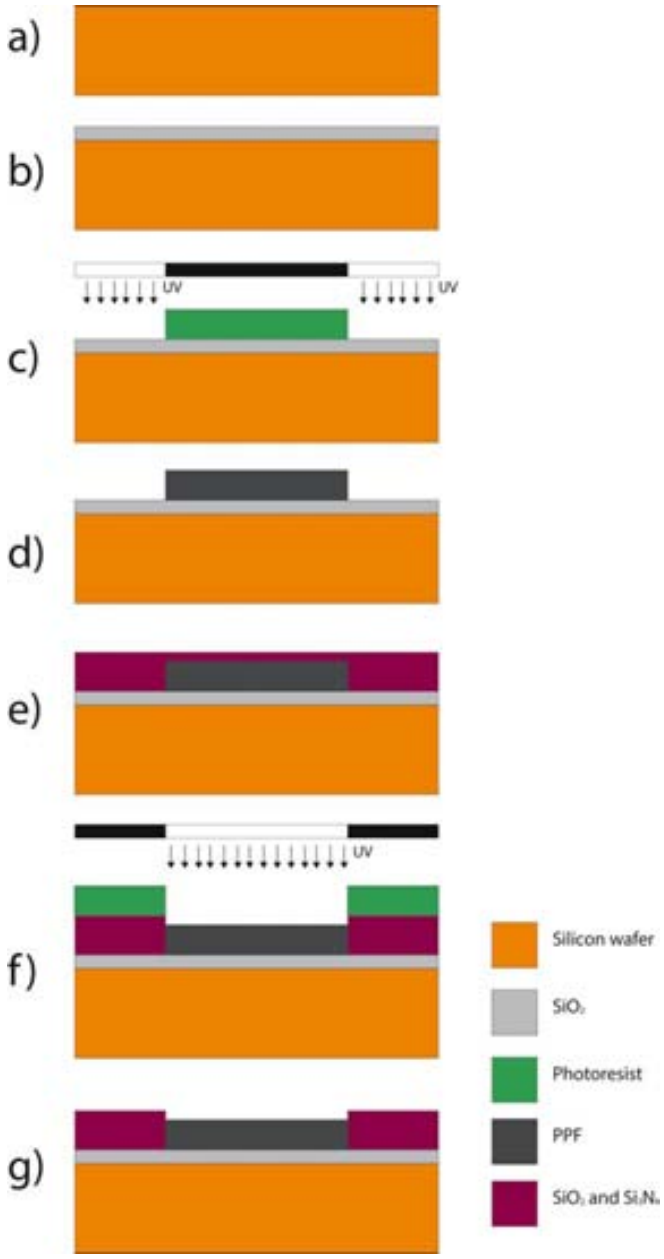

Figure 36. Diagrammatic representation of the PPF microelectrode fabrication process.

The structures that will give rise to the final PPF electrodes were transferred to the photoresist by photolithography in a double-side aligner (Karl Suss MA56) using a bright field, soda-lime/chromium photomask (Deltamask, NL). After developing the resist, the wafers were dried and subject to a soft bake process of 24 hours at 80 ºC to evaporate solvents and other unwanted volatile impurities. The wafers were then introduced in an RTP oven (Centrotherm, DE) where the resist structures were pyrolyzed in a three-step process [97]. First, the wafers were heated up to 1000 ºC at a

rate of 60 ºC/s. Then, the wafers were kept at the maximum temperature for 1 hour, after which the wafers were left to cool down to room temperature inside the oven.

After pyrolysis, the wafers were cleaned with N_2 gas and deionized water to remove particles detached from the wafer edges during pyrolysis, and which ended up on the wafer

surface. The next step was the PECVD (Plasma Enhanced Chemical Vapour Deposition) deposition of the passivation layer, consisting of a double layer of 400 nm of silicon oxide and 400 nm of silicon nitride. The passivation layers were deposited in an Oxford IPT Plasmalab 800 Plus (Oxford Instruments, UK) following the next process conditions: for 400 nm Si3N4 (T = 350 – 450 ºC, P = 550 - 750 mT and P_{RF} = 50 - 70 W) over 400 nm of SiO_2 (T = 350 – 450 ºC, P = 800 - 1100 mT and P_{RF} = 150 - 250 W). Before depositing the passivation the PPF was previously cleaned with an ammonia plasma (T = 350 – 450 ºC, P = 800 - 1100 mT, t = 250 - 350 s and P_{RF} = 50 - 70 W). Due to the bad adherence between PPF and CVD silicon oxide a previous process to enhance the adherence was necessary. This process will be explained further in section 3.1.

Once the passivation was in place, it was necessary to open it to define the electrodes active areas and contacts. This was done in a second photolithographic step. This time, 6 µm of positive photoresist were spin coated on the wafers, and subsequently insolated through a dark-field Cr photomask. Once the resist was developed, the contacts and active areas were patterned on the passivation layer using a Deep Reactive Ion Etching (DRIE) process (Alcatel AMS - 110DE) ranging these conditions (T = 20 – 5 ºC, P_{RF1} = 2000 - 3000 W, P_{RF2} = 100 - 300 W, Q_1 = 20 – 40 sccm C_4F_8, Q_2 = 10 – 30 sccm CH_4 and Q_3 = 10 – 20 sccm He). This removed the silicon nitride and silicon oxide layer from all the areas not protected by photoresist. Then the remaining photoresist was removed in a stripper bath at 80 ºC.

Last, the wafers were diced into individual chips. Because wire bonding to PPF is not possible, the contacts to these electrodes were made attaching a thin copper wire to each contact pad using silver epoxy (RS Amidata, ES). This contact was then covered by a glob of photocurable resist (Epotek OG147-7) and subsequently cured in a UV flood lamp (Dymax 5000 – EC). After this, the electrodes were ready for use in electrochemical experiments.

3.2.2. Hg determination procedure

The experimental parameters were optimized to achieve detection limits in line with current legislation, and which are in the low ppb range. [128] Electrochemical detection of Hg on PPF electrodes was done using Square Wave Anodic Voltammetry

(SWAV) in 0.5 M KNO_3 solutions of pH adjusted to 1.5 HNO_3, and calibration curves were constructed by the standard additions method, using a 10 ppm Hg stock solution.

Our detection procedure was adapted from previous work, [126] and consisted of three steps. First, mercury was deposited on PPF at a potential of -0.5V vs. Ag/AgCl for 1800 s. During the electrodeposition step, the solution was agitated with a magnetic stirrer at 330 rpm to increase mass transport toward the PPF electrode. Next, mercury was stripped in an anodic square wave scan between -0.6 V up to 0.2 V vs. Ag/AgCl at a frequency of 25 Hz and a signal amplitude of 50 mV. Although two different peaks could be observed associated to mercury, at –0.45 and –0.1 V vs. Ag/AgCl, only the signal at –0.45 V was used for analytical purposes. The other wave was associated to calomel formation arising from chloride ions leaking out of the reference electrode.

Last, after each measurement, new square wave scans were run to check that the signals due to mercury no longer appeared, thus ensuring that all the mercury had been effectively stripped and that the electrode could be used in a new determination.

3.3. Results and Discussion

3.3.1. Physical characterization

Photoresist undergoes important physical and chemical changes during pyrolysis. Profilometry and confocal microscopy were heavily relied upon to follow the morphological evolution of the resist structures and the passivation throughout the fabrication process. Figure 37 shows profilometric data of an electrode structure after pyrolysis. These resulting disk electrodes are 1.5 mm in diameter and connected to a 0.8 x 3 mm contact pad by a 0.5 mm wide and 3 mm long conducting track. The figure shows how resist flow during pyrolysis results in the rounding of the structure edges. Also, because resist flows during the early stages of the heating ramp, it builds up around the edges, leaving slightly depressed areas behind. This depression is clearly visible in the disk, where the central area is ca. 1 micron thinner than the edges. All in all, the resist has shrank about 80% during pyrolysis (from 20 microns down to 3 - 4 microns), which is in line with our previous observations [129] and also those of other workers. [75, 80, 88, 130, 131]

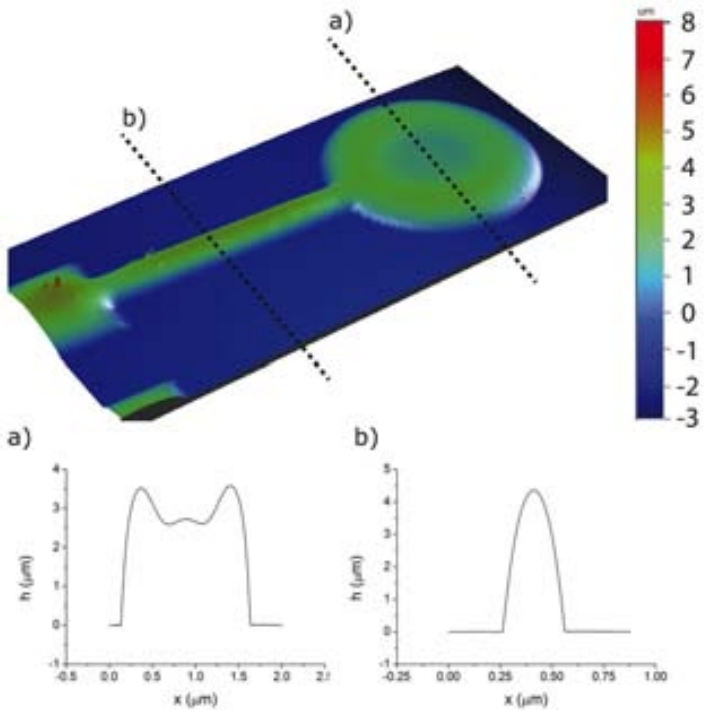

Figure 37. Confocal microscopy image of the PPF structure used in the microfabrication of disk electrodes. The dotted lines indicate the areas where the profilometric data displayed in sub-figures (a) and (b) were collected.

Due to the smoothness of PPF, a certain pre-treatment is required to facilitate the adhesion of the passivation layer. We chose to roughen up the surface and, for this, we used oxygen plasma, which is known to etch PPF.[117] We used a TEPLA 300E barrel-type reactor to produce the O_2 plasma, controlling time and power. Although plasma homogeneity is better in planar reactors, an absorbance reading enabled us to monitor the activity inside our reactor and achieve good process reproducibility.

We compared different treatments and established a series of process end-point guidelines. Figure 38 and annex 2 show the results of different experiments using PPF samples exposed to oxygen plasmas at powers ranging from 220 W up to 400 W between 30 and 120 s.

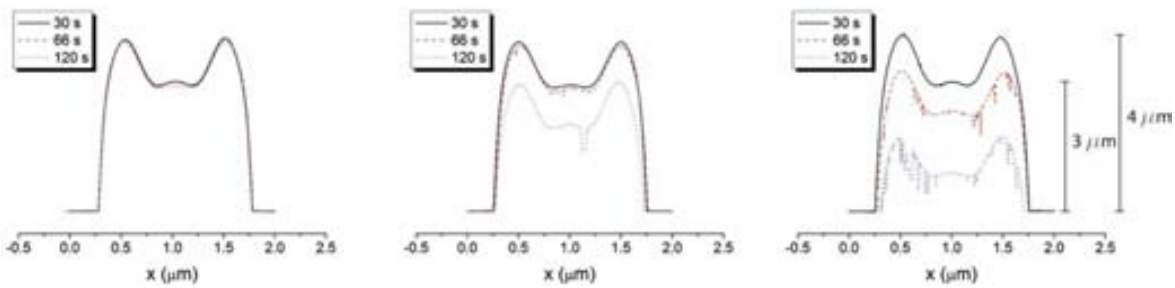

Figure 38. Effect of exposure to oxygen plasma on PPF. (a) 220 W, (b) 300 W, (c) 400 W.

It is clear from the figure that PPF is a very soft material that can be easily etched at moderate to high powers. In fact, etching of PPF by oxygen plasma is much faster than etching of fresh photoresist, which points to the possibility of making PPF structures by etching rather than direct lithography.

On the other hand, exposing PPF to low power oxygen plasma results in rougher PPF surfaces without substantial overall damage to the structure. Although oxygen plasma makes the PPF surface rougher, this is not sufficient to improve adhesion of the PECVD SiO_2 and Si_3N_4 layers, which flake off easily, soon after their deposition. To promote adherence of the passivation layer on the PPF further we silanized the PPF structures after roughening the PPF surface with plasma. A stream of SiH_4, one of the CVD precursors used in the passivation process, was flowed for 10 minutes (T = 350 – 450 ºC, P = 800 - 1100 mT, Q_1 = 20 – 40 sccm SiH_4 and Q_2 = 900 – 1100 sccm N_2) following plasma treatment and prior to the deposition of the passivation layer.

The resulting passivated PPF structures were much more stable than before. Stability of the passivation layers was tested by immersing the wafers with passivated PPF structures in water, and drying them in a N_2 stream. We had previously observed that poorly adhered layers readily came off on immersion of the coated wafers in water.

The passivation was measured by ellipsometry before and after this test, and the results are given in Table 10. The results demonstrate the passivation remained on the surface of the PPF and that its thickness did not change as a result of the immersion in water.

Table 10.- Si_3N_4/SiO_2 passivation layer adhesion test results.

Parameter	Before adhesion test		After adhesion test	
	Si_3N_4	**SiO_2**	**Si_3N_4**	**SiO_2**
Thickness (nm)	404.6	430.7	406.5	425.6
σ^2 (nm)	38	91.9	27.7	40.1

The fact that the surface pre-treatment (silanization) and the passivation deposition can be carried out in the same reactor is a great advantage, as less wafer handling reduces the possibilities of wafer contamination and/or physical damage during fabrication. After depositing the passivation, the electrode areas and contacts were lithographically defined in the passivation, which was subsequently etched by deep reactive ion etching (DRIE).

This etching step must be executed with great caution. Although over-etching is a common practice aimed at ensuring that even the smallest features are open and it does not damage hard materials such as metals, it may cause the partial or complete

disappearance of soft materials, such as PPF, Figure 39 shows the resulting disk electrodes.

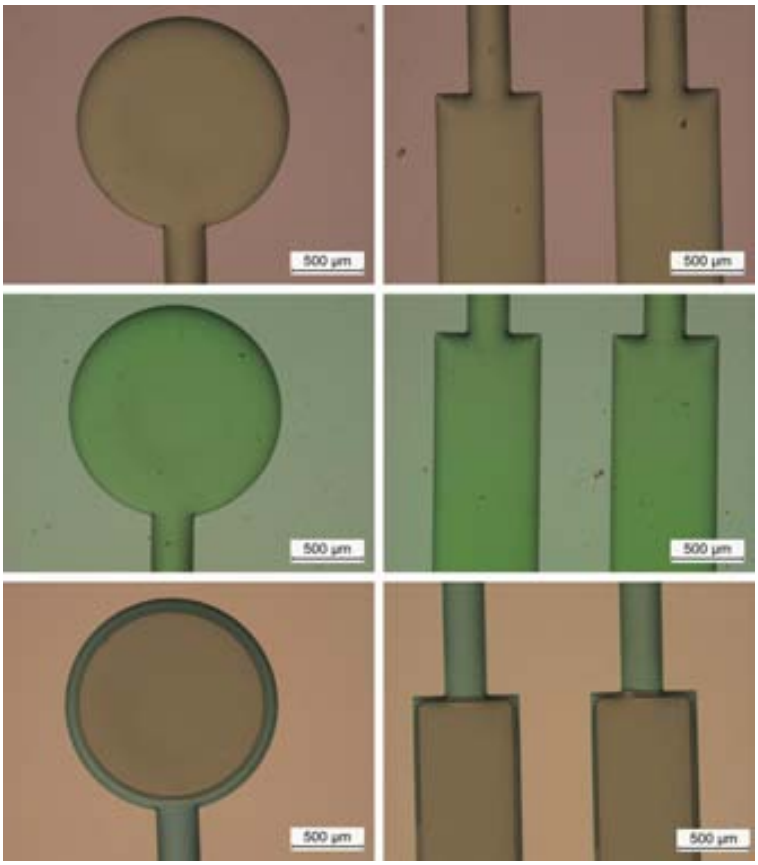

Figure 39. Optical microscopy images of the different parts of a microfabricated PPF disk electrode at the following stages: (a) freshly sinthesisez PPF structure, (b) SiO_2/Si_3N_4 passivated PPF structure, and (c) final PPF disk electrode after opening the passivation.

3.3.2. Electrochemical characterization

Before attempting the detection of mercury, the electrodes were first characterized using ferrocyanide solutions in 0.5M KNO_3. Figure 40 shows background corrected cyclic voltammograms at scan rates ranging from 50 mV/s up to 0.5 V/s of ferrocyanide solutions.

The deviations from the Randles-Sěvčik equation at faster scan rates are due to the vertical sidewalls and the surface roughening resulting from the DRIE over-etch of the PPF layer. These voltammograms display good electrochemical characteristics in terms of ΔE_p and I_p values. Peak current correlates well with the square root of scan rate, indicating diffusion control, and the average electron transfer rate constant determined from the dependency of peak-to-peak separation with scan rate[132] was 0.014±0.007 cm/s, which is in line with the value of ca. 0.015 $cm \cdot s^{-1}$ reported previously for this material.[129]

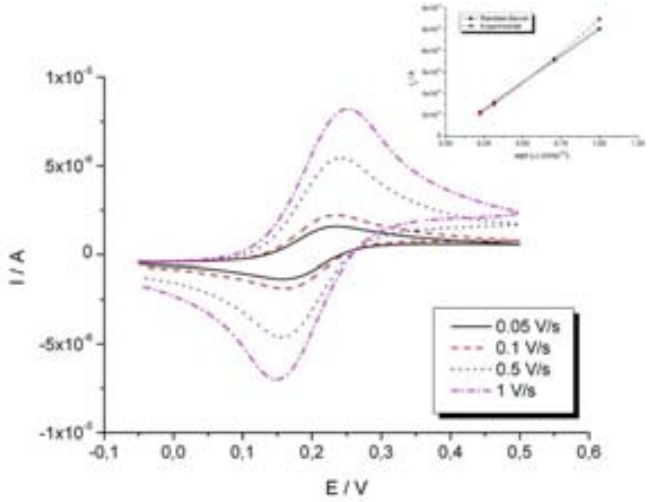

Figure 40. Cyclic voltammograms obtained at a microfabricated disk PPF electrode in 2 mM ferrocyanide at differen scan rates, and the overlap of Randles-Ševčik prediction and the peak current density the inset.

3.3.3. Determination of electrodeposition parameters

After checking the suitability of PPF electrodes as described in the previous section, different electrodeposition potentials were tested to optimize the mercury detection protocol. For this, 10 ppb mercury solutions in 0.5M KNO_3 and pH=1.5 were used. In this experimental series, the electrodeposition time was fixed at 30 min. The solutions were stirred during the electrodeposition step and the stirrer was switched off during the stripping scan by square wave voltammetry (SWASV).

Electrodeposition potentials between -0.9 and -0.4 V vs. Ag/AgCl were studied. The large currents demanded by the onset of the hydrogen evolution process result in the detachment of the PPF from the silicon oxide substrate, limiting the cathodic potential window accessible to our electrodes. Using slower thermal ramps during PPF synthesis may mitigate this effect, and work is currently under way to overcome this problem.

On the other hand, the first mercury stripping peak was observed between -0.5 and -0.4 V, so electrodeposition potentials above -0.4 V were ruled out. -0.5 V was found to be the most suitable electrodeposition potential under our experimental conditions, at which an electrodeposition time of 30 minutes was required to achieve a detection limit in the low ppb range. Figure 41 shows typical mercury stripping voltammograms obtained at PPF disk electrodes.

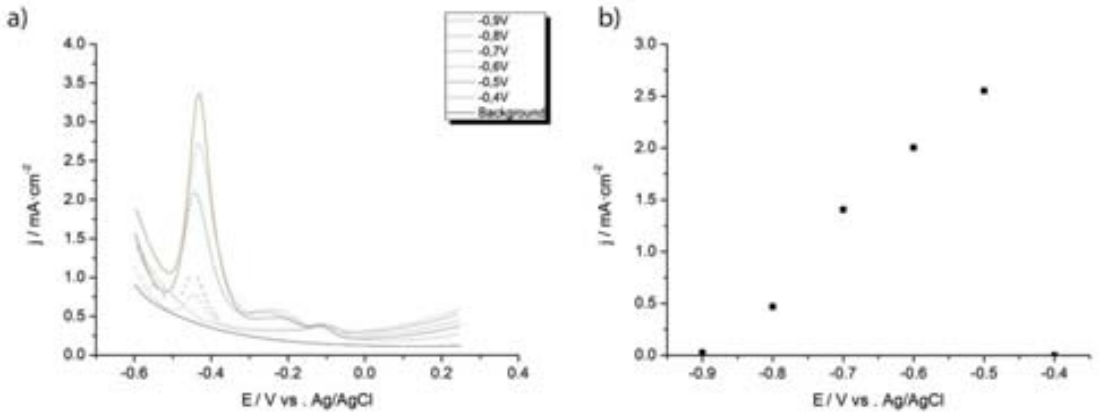

Figure 41. (a) Stripping peak dependency on electrodeposition potential. (b) Typical mercury square wave anodic stripping voltammograms after electrodeposition for 30 min at different potentials. -0.5 V vs. Ag/AgCl was chosen as optimum electrodeposition potential.

The voltammograms present three different mercury-related peaks, at -0.45, -0.25, and -0.1 V vs. Ag/AgCl, respectively. Although a speciation analysis is beyond the scope of the present work, these different signals are due to the stripping of different mercury I and mercury II species.

3.3.4. Mercury detection down to 2 ppb

Using the experimental conditions identified as optimum above, mercury could be detected down to *ca.* 2 ppb. Figure 42 shows a typical standard additions graph showing that the stripping peak current density increases linearly with mercury concentration in the range between 2 and 14 ppb.

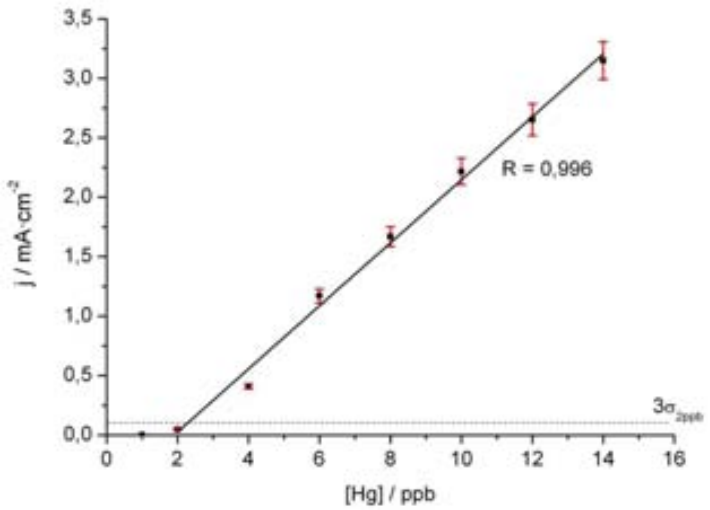

Figure 42. Stripping peak current at PPF microelectrodes increases linearly with mercury concentration between 2 ppb and 14 ppb.

The sensitivity found at these PPF microelectrodes was around 2.67 $\mu A \cdot cm^{-2}$/ppb-mercury, and the correlation coefficient, R=0.996, demonstrate the high linearity of

the response, and the narrow error bars demonstrate excellent reproducibility. Using the 3σ method (N=3 at 95% confidence) we obtained a limit of detection of 2.35±0.25 ppb. However, the voltammograms recorded in solutions containing 1 ppb already showed a slight shoulder around -0.45 V, suggesting that the detection limit can be improved, reaching the limit recommended by the World Health Organization (WHO) as the maximum allowed mercury levels in water. Although the obvious way to improve the detection limit consists in extending the electrodeposition period, our current method already takes 30 minutes, which might be considered long in the light of recommended standardized methods. [128]

In order to make a more competitive method, the electrodeposition of mercury might be enhanced either by improving mass transport toward the electrode surface, using flow devices, or decorating the PPF surface with gold nanoparticles, either before or during the electrodeposition of mercury.[117] Although this will increase the cost per analysis, it will also result in an overall shorter analysis time (USEPA Method 7472 recommends a mercury electrodeposition period between 1 – 3 minutes).

3.4. Conclusions

We have presented the microfabrication at wafer level of PPF disk electrodes featuring a passivation layer consisting of silicon oxide and silicon nitride. Passivation of PPF with other materials such as SU-8 and SiO_2 have been reported so far [111, 120, 133-136], but in this work we present a new route to define electroactive windows using a passivation layer deposited by CVD and its opening by deep reactive ion etching (DRIE).

Direct adhesion of this passivation layer, is poor on bare PPF substrates due to the high surface smoothness of the latter. However, treating the PPF with a mild plasma and silanizing it immediately before CVD deposition of the passivation results in an adequate adhesion of the passivation. Further lithographic processing of the passivated PPF structures is possible, and we used a DRIE step to define the disk electrodes through the passivation and the contact pads.

The voltammetric characterization using ferrocyanide solutions showed that the resulting PPF electrodes were suitable for electroanalytical work, using the detection of mercury in aqueous solutions as an example. A linear range was found between 2 and 14 ppb, and even though an electrodeposition period of 30 minutes was required, we believe this is a reasonable starting point for the development of real applications using PPF electrodes, given the relatively low cost and ease of fabrication of this material.

In addition to the detection of heavy metals, PPF may thrive in plenty of other applications where glassy carbon electrodes have traditionally been the material of choice. This is the case of enzymatic fuel cells, where PPF electrodes have recently been used, [98] and another case might be biosensors, [134] where covalent surface functionalization may be easier on a carbon than on a gold or platinum surface,[137] thanks to the rich chemistry of carbon and the ease of modification by different oxidative or reducing routes.

In addition to the work developed in this chapter, PPF electrodes has been used in the development of microfluidic enzymatic biofuel cells, and these kind of electrodes has given good results. In addition to my thesis, I have also collaborated in the work published by Ms. González-Guerrero, *M. J. González-Guerrero, J. P. Esquivel,* ***D. Sánchez-Molas****, P. Godignon, F. X. Muñoz, F. J. del. Campo, F. Giroud, S. D. Minteer, and N. Sabate, "Membraneless Glucose/O2 Microfluidic Enzymatic Biofuel Cells using Pyrolyzed Photoresist Film Electrodes " Lab on a chip, 2013*, and where I participated in the fabrication of the PPF electrodes. The membraneless enzymatic biofuel cell

developed by González-Guerrero et. al. is continuously provided with all the necessary reactants in the anode and the cathode for the correct operation of the device using microchannels. Regarding the fabrication of carbon electrodes in microfluidic fuel cells, it might be focused on the development of three dimensional PPF micropillar array electrodes by Deep Reactive Ion Etching (DRIE). This technique has already been tested in chapter 3, but there are at least two limitations. First of all the physical parameters of the DRIE process must be under strict control because slight overtimes of the process can remove completely the whole PPF layer. The second drawback is in the deposition of thick layers of photoresist before the pyrolysis to have tall microstructures. Note that although the deposition of AZ photoresist with thickness of 40 µm and 60 µm has been attempted, the results have been poor due to the lack of homogeneity and the appearance of a too many bubbles that caused the completely destruction of the photoresist during the pyrolysis.

Furthermore, thanks to the good results obtained in the detection of mercury with the PPF disk electrodes from chapter 3 I have also designed and fabricated, in parallel with my thesis, a flow cell using PPF microband electrodes, Figure 43. This flow cell incorporates internally all the necessary electrodes, built all of them with PPF, to measure the sample under study.

Figure 43. PPF microband flow cell to detect mercury in water samples.

The optimal values of the electrodeposition potential, the electrodeposition time and the flow rate of this flow cell have already been found. Currently the calibration curve at different concentrations of mercury within the range from 0.5 to 14 ppb is been performed to find out the minimum level of mercury that this flow cell is able to detect. Moreover, once the calibration curve will be done gold nanoparticles will be deposited on the surface of these PPF electrodes to enhance the minimum level of detection of this flow cell.

Chapter 4. Fabrication and characterization of miniaturized microbial fuel cells

This chapter describes the fabrication, by rapid-prototyping techniques, of a miniaturized microbial fuel cell using the fully-conducting micropillar array electrodes developed in chapter 2. The aim is to increase as much as possible the typically low output power densities of this kind of fuel cells. The results presented in this chapter show that fully-conducting micropillar array electrodes can improve the maximum power and current densities as well as increase the open circuit voltage of these miniaturized microbial fuel cells as function the geometry of the chosen array. Also, the results show that the performance of these miniaturized microbial fuel cells depends on the time, achieving the maximum electrical performance at short operation times. For greater times, the performance approaches that of miniaturized microbial fuel cell using flat electrodes.

This work will be presented at the 4th International Microbial Fuel Cell Conference in Cairns (Australia) under the title, *Improving the electrical performance of microbial fuel cells using fully-conducting gold micropillar array electrodes.* ***Sánchez-Molas, D****., Pujol, F., Schmidt, I., Uría, N., Mas, J., Muñoz, F. X., Esquivel, J. P., Sabaté, N., Schröder, U., and Del Campo, F. J.* The Labview routine described here has also been published in, *N. Uría,* ***D. Sánchez****, R. Mas, O. Sánchez, F.X. Muñoz, J. Mas, Effect of the cathode/anode ratio and the choice of cathode catalyst on the performance of microbial fuel cell transducers for the determination of microbial activity, Sensors and Actuators B: Chemical, 170 (2012) 88-94.*

4.1. Introduction

Most of the world energy demand is satisfied by fossil fuels and nuclear power. The World Nuclear Association estimates that the electrical power demand is around 15.000 TW/h, and this amount is expected to increase up to 30.000 TW/h in 2030.

According to the World Wide Fund for Nature (WWF) green and renewable sources of electricity are a real alternative to meet current and also future energy demands. Moreover the most important advantage of renewable energy sources is their relatively low environmental impact and favourable contribution to global warming. This type of energy takes advantage of inexhaustible natural sources such as the sun, the natural water streams, or the wind for running systems that transform mechanical energy into electricity, or by the photoelectric effect in the case of the solar energy. In

spite of the benefits of all of these sources of green energy, they require complex and typically large facilities that make them economical only at a large scale.

In contrast to the energy sources explained above, other types of devices capable of generating green electricity in a relatively small space have started to emerge. These are known as fuel cells. As described in the introduction of this thesis, a fuel cell is an electrochemical device that generates electricity using an external chemical energy source known as fuel. The chemical energy stored in the fuel is converted to electricity by a catalyst, [11, 13, 138] which in the case of the present chapter is composed by microorganisms [19, 24, 139].

Fuel cells using microorganism as catalysts are known as Microbial Fuel Cells (MFC). In general, MFCs use exoelectrogenic bacteria to oxidize organic fuels using their own metabolism, and generating electrons. Exoelectrogenic bacteria have different ways to transfer these electrons to the anode. [17, 19, 20, 140] These mechanisms involve electron mediators or shuttles [23, 141], nanowires [21, 22] or even direct membrane associated electron transfer [142, 143]. Electrons flow to the cathode through an external circuit generating electrical current.

The applications where microbial fuel cells can be used range across different fields [33, 144-149], such as water treatment [33, 144, 150], environmental sensors [147], hydrogen production [34, 36, 37, 151] and also they have even been tested as power source for low-power medical devices [26]. However for the generation of electricity they have not yet been used due to the low output power densities that they can deliver compared to other types of fuel cells. To deal with this issue, there are different strategies to improve the power output of these devices [14, 152, 153] such as decreasing the ohmic loses by reducing the distance between the electrodes, using thinner proton exchange membranes [154], synthesizing new materials to facilitate the contact with the bacteria [155-157] and thus electron transfer [32, 157], or also improve the ion conduction through the Proton Exchange Membrane (PEM) [12, 158, 159].

The application described in this chapter takes advantage of the enhanced current flux displayed by the fully-conducting gold micropillar array electrodes described in chapter two. This chapter focuses on the study of the electrical response of miniaturized microbial fuel cells fabricated by rapid-prototyping to find out if the use of gold fully-conducting micropillar array electrodes improves the electrical efficiency of miniaturized microbial fuel cells [14, 148, 153, 160, 161].

The use of microelectrode arrays for enhancing the sensitivity in electrochemical sensors [6, 7, 90, 91, 94, 99, 162-167] has been widely demonstrated. Microelectrodes

take advantage of hemispherical diffusion to increase the consumption of chemical electroactive species [162, 163, 166, 168]. Besides, if microelectrodes are adequately arranged in an array, their resulting response equals that by a single microelectrode times the number of microelectrodes in the array. The introduction of silicon micromachining techniques has made the fabrication of microelectrodes more accessible, allowing the development of even 3-dimensional microelectrodes [165, 169-171]. Thanks to their side-walls, 3-dimensional electrodes present larger active-surfaces than flat electrodes, and 2-dimensional microelectrodes. This additional active-surface helps to increase the amount of charge collected by the electrodes.

In addition to the design of the electrodes, their packaging in a device is another key matter. Polymeric materials such as PDMS (Polydimethylsiloxane) and SU-8, in combination with photolithography have been the most common materials used in the development of lab-on-a-chip and also microfluidic devices to date [172-175]. More recently, the introduction of milling and drilling machines [176], cutter plotters [70] and low power CO_2 lasers has transformed the heterogeneous integration of these devices, making the development of new devices easier and less costly, thanks to their flexibility and the low cost of the materials used. Today, 3D printing is rising as a very promising tool in the engineers arsenal, enabling things that up until now were impossible to imagine [177-179].

This work benefits from the knowledge acquired in the previous work on fully-conducting gold micropillar array electrodes [169, 171] to fabricate and characterize miniaturized microbial fuel cells by rapid-prototyping techniques. The results presented here show that fully-conducting gold micropillar array electrodes can boost the current and power densities at short times, but there seem to be no real benefits in the long run because the electrical performance converges to the planar electrode case. Table 11 summarizes the reported current and power densities reported in the recent literature on microbial fuel cells.

Table 11. Electrical performance from the most recent microbial fuel cells reported to date.

Year	Bacteria	Electrode	TEA	$\mu A \cdot cm^{-2}$	$\mu W \cdot cm^{-2}$	Reference
2013	*Shewanella Oneidensis MR-1*	Micropillar array elecrodes	Ferricyanide	310	132.3	This work
2012	*Shewanella Oneidensis MR-1*	-	-	25	1.5	[180]
2012	*Shewanella Oneidensis MR-1*	Gold nanoparticles on carbon paper	-	88.3	34.6	[181]
2011	*Shewanella Oneidensis MR-1*	Gold on glass substrate	Air	214.8	2.9	[182]
2011	*Geobacteraceae-enriched culture*	Gold	Ferricyanide	33	4.7	[183]
2011	*Geobacter sulfurreducens*	Arrays of Gold via-squares	Ferricyanide	14	6.4	[147]
2010	*Shewanella Oneidensis MR-1*	Gold-sputtered on carbon paper	Air	13.5	N/A	[184]
2006	*Shewanella Oneidensis DSP10*	Reticulated vitreous carbon	Ferricyanide	2.4	10	[185]
		Graphite felt		1	3.2	

This chapter reports the greatest current and power densities achieved to date by any microbial fuel cell. These results may open new routes to develop sensors with high sensitivity based on miniature fuel cell architectures. Also, the results of this work may take up again the generation of bio-electricity for applications which do not require big electric power consumption, because even have achieved the highest output power densities to date, the electrical performance of the miniaturized microbial fuel cells presented in this work is too low for the vast majority of the electronic applications which currently in the market.

4.2. Design of a system to characterize automatically fuel cells

This section presents the design and implementation of an instrumental set-up to automate the measurement of electrical parameters of any fuel cell. The usual way to plot the i–V and i-P graphs of any fuel cell is to place a resistor of known value between the anode and the cathode, and then measuring the voltage difference between them to obtain the current delivered by the fuel cell. Because this method is very time consuming, an instrumentation system developed using Labview 8.5 (National Instruments) by GPIB communication protocol was designed to automate the characterization of fuel cells.

This system can perform two types of characterization experiments; the first one aims to obtain the corresponding i–V and i-P graphs, and the other experiment focuses on studying the voltage response of a fuel cell on application of a constant current over an extended period of time. Figure 44 summarizes the architecture of this system.

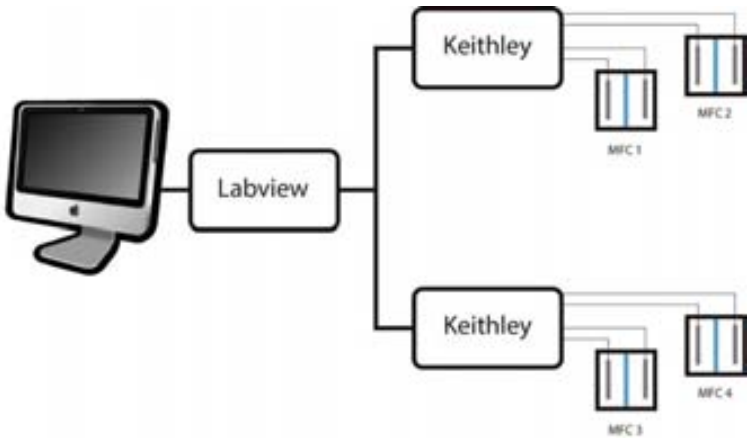

Figure 44. Schematic representation of the instrumentation system implemented to characterize automatically fuel cell.

This system is composed by two Keithley 2612 (Tektronix, USA), each connected to a computer using a GPIB bus. A Keithley 2612 is a source-meter device able to deliver electrical current through a circuit, while at the same time it measures the voltage between the input and the output of this circuit. Besides, each Keithleys has two independent channels, so that four fuel cells can be studied together with two Keithley 2612 in parallel applying different experimental conditions to them.

The algorithms to control the Keithleys using Labview for each one of the two kinds of experiments are showed in Figure 45. The inputs of this system are four: i_{exp}, $i_{step,}$ t_{wait} and t_{finish}. i_{step} controls the current increment, t_{wait} fixes the time for which a constant

current is applied before taking a measure of the voltage and, last, t_{finish} controls the duration of an experiment.

To start plotting the i–V and i-P graphs the first value of the applied current must be zero (i_{step} = 0 A) to obtain the value of the Open Circuit Voltage (OCV). When the time reaches t_{wait}, the voltage is measured and saved to a file. If the voltage is greater than zero after t_{wait}, it means that the fuel cell has not reached its maximum level of current yet, and the applied current is increased in i_{step} Amperes. This process is repeated until the measured voltage becomes zero or lower. When this happens, the i–V and the i–P graphs are plotted and saved in a file.

The process to measure the generated voltage when a constant current, i_{exp}, is applied to the fuel cells is approximately the same as in the case described above to obtain the i–V and the i–P graphs, but in this case the value of the applied current does not change at any time. At the beginning of this routine the desirable value of the current is applied to the fuel cell and it is kept until the end of the experiment. The voltage is then measured during a given t_{wait}. When this time is over the voltage is saved. After saving this value the system measures the voltage again without changing the value of the current, this process is repeated until t_{finish} is reached. At the end of the experiment the evolution of the voltage as function of the time at a given constant value of the current is plotted in a graph and saved into a file.

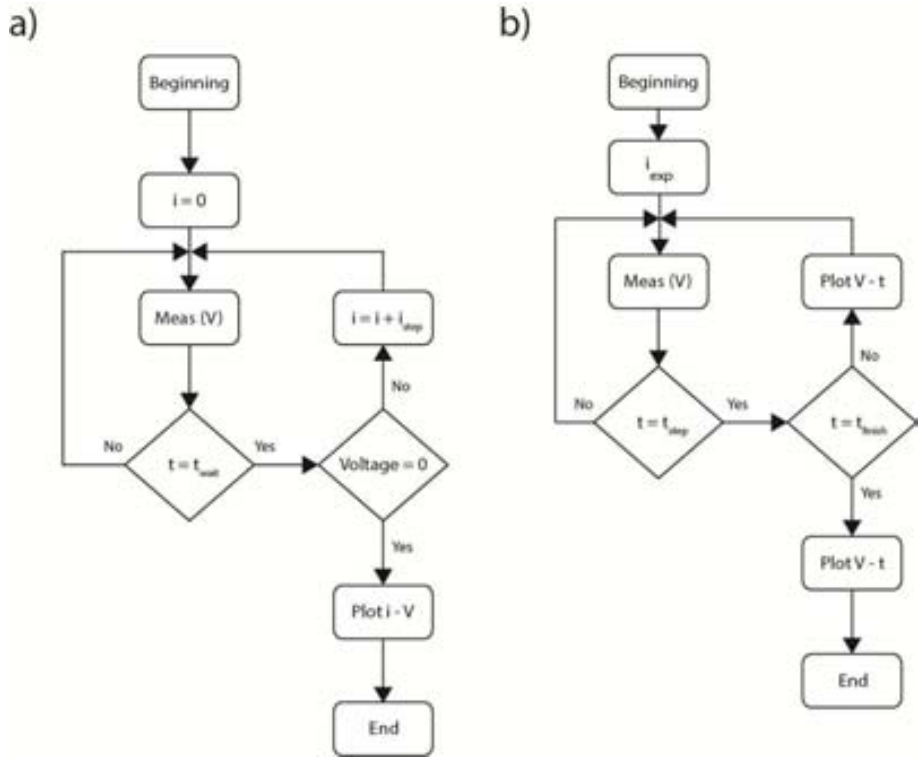

Figure 45. Diagrams of the algorithms used to characterize fuel cells, a) algorithm to plot i-V and i-P graphs, and b) algorithm to measure the voltage over the course of time at a given constant current.

4.3. Design and fabrication of miniaturized microbial fuel cells

The aim of this section was to fabricate a miniaturized microbial fuel cell of volume less than or equal to 1 cm^3 so that the micropillar array electrodes could be used more effectively. Note, that the cost of the fabrication of gold micropillar array electrodes at wafer-level is over 300 €/wafer, so making smaller electrodes chips allows for more experiments per wafer. For this reason the different parts which form the fuel cell were designed to make the most out of each wafer.

To achieve this goal the parts of the fuel cell were fabricated using rapid-prototyping techniques. Different adhesive tapes provided different functions, and enabled us to achieve the thinnest device, while using that the parts were completely sealed to avoid fluid leaks in the anode and the cathode. Figure 46 shows the scheme of this miniaturized microbial fuel cell, which is described in detail next.

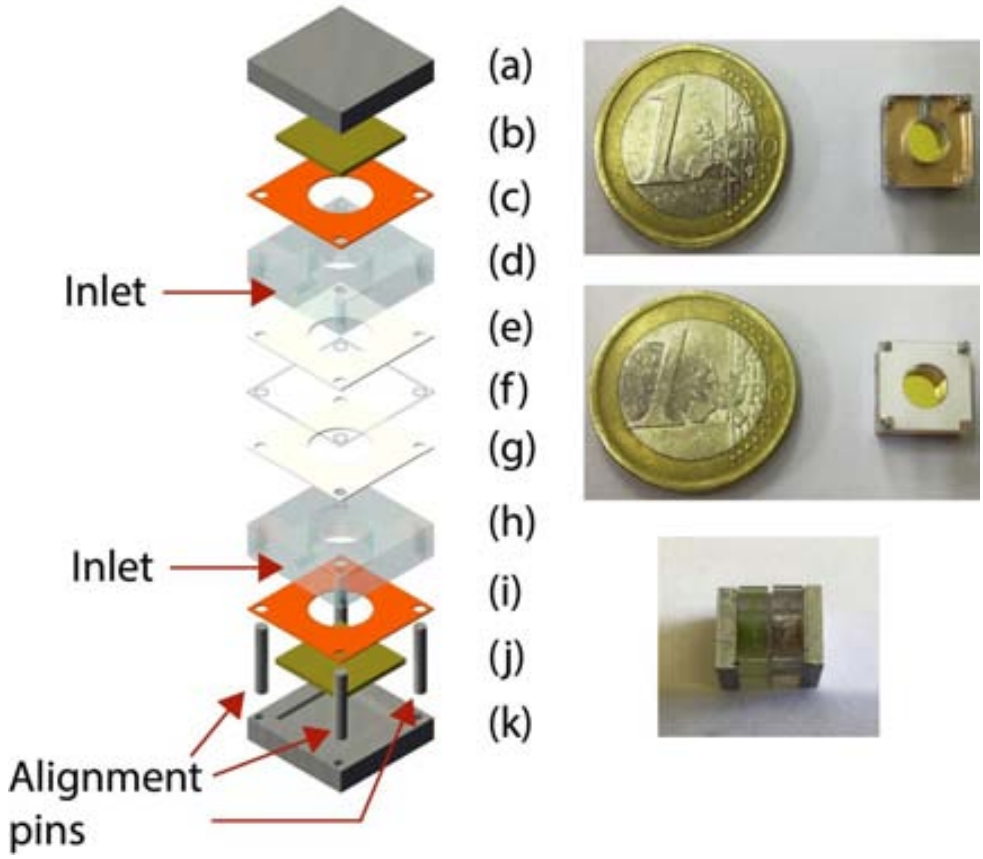

Figure 46. Diagrammatic representation of the miniaturized microbial fuel cell showing the different parts of it (left). Photos of the different layers which form a miniaturized microbial fuel cell (right).

10 x 10 x 2mm aluminum pieces were used for contact and electrode support. A 0.6 mm deep and 7 x 7 mm square socket was milled (Roland MDX-40A) in these aluminum pieces to hold the electrode chips. Besides, four 1 mm diameter and 1.5 mm depth holes were drilled in the corners to use them for aligning the various parts of the fuel cell using pins (a and k). A double side adhesive copper tape (3M, RS Amidata, ES) was used to provide electrical contact between the electrode and the back of the aluminum contact (c and i). Finally this part was pressure-attached to the reactor (d and h).

Both sides of the fuel cell, anode and cathode, were made by milling of a 3 mm thick PMMA (Polymethylmethacrylate) piece. Each reactor is a square of 1 cm of side and 3 mm thickness. The main cavity was drilled through these PMMA blocks using a 5 mm drill bit. Besides, four alignment holes were drilled, and also another hole of 1 mm of diameter was also created on one side of the reactor as inlet to allow the pass of the reactants from an external source to inside the chamber. The reactors were attached to the membrane (e and g) using double side Pressure Sensitive Adhesive (PSA) (AR care 8939, Adhesives Research Inc, IR), cut by a cutting plotter (Roland CAMM-1 Servo, Roland DG, ES).

The membrane used in this work was Nafion 117 (Ion Power, Inc., USA) cut in 9 x 9 mm squares (f). Note that the membrane was cut in smaller squares than the remaining parts because the activation process increases the size of Nafion by 10%. Before packaging it with the rest of the fuel cell it was activated in four steps, as follows. First of all the membranes were immersed in a boiling solution of water and hydrogen peroxide for one hour. After this, the membranes were also immersed for one hour in boiling water. Once this was done a solution of water and sulfuric acid with a 96% of purity was used to immerse the membranes for one hour again. Finally the membranes were again immersed in boiling water for another hour.

After activation, the membrane surface was carefully dried to enhance the adhesion between it and the adhesive tape on the reactor side. The other half of the cell was built following the same procedure to complete the fuel cell.

4.4. Preparation of the microbial cultures and chemicals

The Terminal Electron Acceptor (TEA) in the cathode was a 50 mM solution of Potassium Hexacyanoferrate III (Panreac) prepared in 100 ml of phosphate buffer 0.1 M of pH = 7. The phosphate buffer was made stirring 5.25 g of Potassium di-Hydrogen Phosphate PA-ACS (Panreac) with 14.02 g of di-Potassium Hydrogen Phosphate 3-hydrate PRS (Panreac) in one liter of deionized water.

Shewanella Oneidensis MR-1 was the bacterial strain used in the anode. The bacteria were grown in 500 ml of LB growth medium; it was prepared in one liter of deionized water with 10 g of Sodium Chloride (Panreac), 10 g of Tryptone (Conda) and 5 g of Yeast Extract (Conda). Finally when the medium was prepared it was kept for approximately one day at 30 ºC and also stirred at 170 rpm. After this, the medium was split in six different 50 ml falcon tubes which were simultaneously centrifuged at 10.100 G and 4 ºC for 15 minutes. After this centrifugation, four different falcon tubes were chosen randomly to start again another centrifugation under the same conditions than the first one using 50 ml of fresh medium. After finishing the second centrifugation the six pellets were emptied, filled with 1 ml of phosphate buffer, stirred and added together in one tube to get a high concentration of bacteria in the resulting 6 ml of medium. Finally 60 µl of lactate 20 mM were used as carbon source to feed the bacteria.

The amount of bacteria in each of the media used in the experiments was determined counting bacteria colonies on Petri dishes. The average value and the standard deviation of the concentrations of bacteria were respectively $8.43 \cdot 10^{-10} \pm 3.08 \cdot 10^{-10}$ CFU/ml.

A maximum of four different miniaturized MFCs could be characterized in parallel, and experiments were conducted for several days. For this reason, new chemical solutions were prepared before starting a new series of experiments to allow that each one of the miniaturized MFCs had fresh solutions to achieve the most suitable conditions to carry out the experiments.

4.5. Electrical characterization

Different MFCs were built to study the effect of micropillar array electrodes. Micropillar electrodes with the same geometry were used both in the anode and in the cathode. First of all the least densely populated arrays, which center-to-center distance was d = 100 µm and radius $r_{\mu Pill}$ =10 µm and heights of $h_{\mu Pill}$ = 5 µm, 25 µm, 50 µm and 125 µm were used as electrodes. This choice was made to facilitate that the side-walls of the micropillars could be completely covered by bacteria which are a only few microns in size. In addition, flat gold electrodes were also used to provide a baseline for comparison and determine wether the presence of micropillars brought about any difference.

Once the MFCs were assembled the reactors were slowly filled with the bacteria culture and the TEA using a syringe. The fuel cells were filled slowly to avoid the formation and presence of air bubbles inside the fuel cell. Bubbles are a problem because they reduce the volume available for the bacterial culture in the anode or the TEA in the cathode, and also because they may block the electrodes resulting in worse electrical performance.

4.5.1. Study of the electrical response of microbial fuel cells with flat gold electrodes

Experimental parameters i_{step} and t_{wait} are introduced in the control software before starting the characterization of the different MFCs. The values of these two parameters have to be chosen to provide the best balance between the time a MFC takes to reach and hold the maximum voltage at a given current, and also the minimum number of points required to extract the most accurate information from any i-V and i-P graphs.

To make a quick estimation on the most suitable values of i_{step} and t_{wait} prior to extracting the curves, the transient voltage response was studied at different current levels. The typical results of these experiments are plotted in Figure 47. This figure shows how the voltage depends on the current and time; the voltage decreases when the current increases following the behavior of a typical fuel cell. Moreover, the voltage also decreases from the beginning of the experiment until its end. Also, note that the speed of the voltage which the voltage decreases because it depends on the current the microbial fuel cell delivers. These two factors affect the choice of t_{wait} and

i_{step}. If t_{wait} is too short the voltage at this level of current might not reach the maximum level, on the other hand if i_{step} is too big maybe the number of points to plot the i-V and the i-P graphs is too small, and therefore the extracted information may not be so accurate.

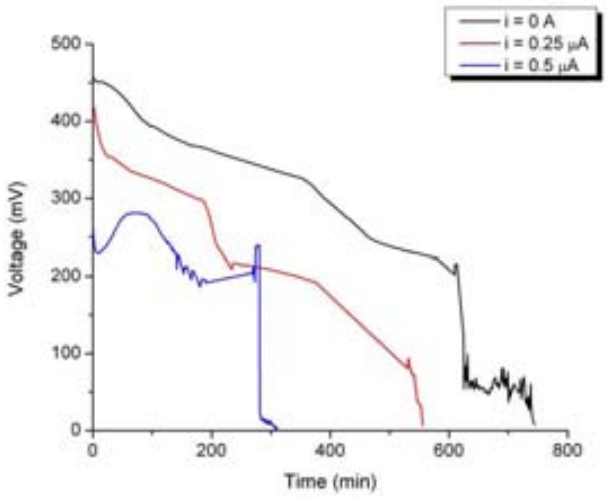

Figure 47. Voltage over the time generated by three microbial fuel cells with flat electrodes each one of them at a given constant current.

The explanation why voltage decreases can be found in the consumption of the TEA and the mediators inside these fuel cells because they were not supplied with fresh and instead they were run as batteries. Moreover, voltage can also decrease due to the diffusion of the oxygen in the anode. Often in conventional PEMFC the main path for the diffusion of oxygen to the anode is through the PEM, but for the miniaturized MFCs designed in this thesis, the presence of oxygen may also be accessing the system through the gaskets of the adhesive layers used to hold the different pieces together, or also through the open inlets. The presence of oxygen in the anode can impose important limitations to the operation of these fuel cells, because it prevents the flow of electrons towards the cathode through the external circuit, as they are directly transferred to Dissolved Oxygen (DO) in the anode [186]. This explains the response showed by Oh et al. who described how the concentration of DO in the anode affects the performance of a MFC when it exceeds a certain level. When this happens the electrons are consumed in the anode, so less are able to reach the cathode, causing that the current and also the voltage decay sharply.

Moreover, the formation of Prussian Blue on the cathode side of the PEM can be another cause of MFC malfunction. This Prussian Blue formation on the PEM creates a barrier that hinders the passage of protons through the PEM. The formation of Prussian blue in this case is caused by the constant reduction of the Potassium Hexacyanoferrate III [187-189] in the cathode due to the electrons coming from the fuel cell anode since the beginning of the experiment.

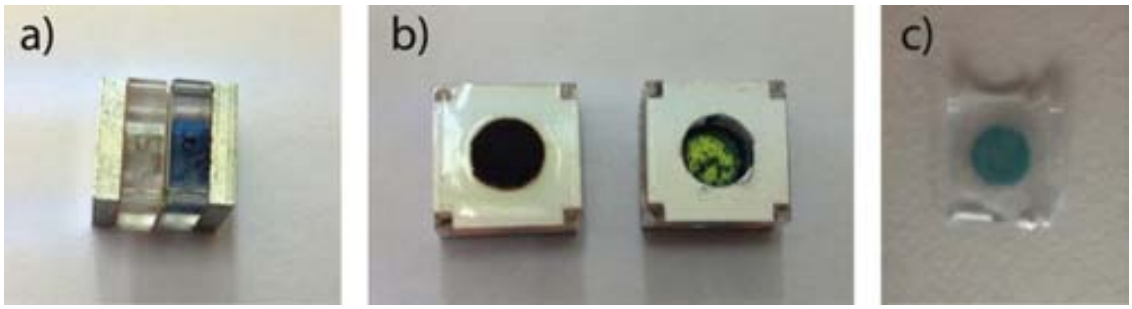

Figure 48. A miniaturized microbial fuel cell after finishing an experiment. a) Prussian blue in the cathode, b) Prussian blue deposited on the MEA and on the surface of the electrode and c) Prussian Blue in the MEA.

Another cause of malfunction may come from the leakage of the TEA from the cathode to the anode through the MEA, killing bacteria, but in this case this was not observed because the anode was not dyed yellow, a telltale of ferricyanide presence.

Finally, at the end of the experiment the voltage drops sharply finishing the operation of the microbial fuel cells because the fuel, the mediator, or both are completely exhausted.

Miniaturized MFCs with flat gold electrodes where tested to extract their i-V and i-P graphs at different times of the experiment with the aim of comparing in the next section the performance with MFCs with gold fully-conducting micropillar array electrodes. The goal of this study is to determine whether the use of micropillar array electrodes helps to increase the electrical performance of miniaturized microbial fuel cells. The resulting i-V and i-P graphs recorded at different times of the experiments for MFCs with flat gold electrodes are showed in Figure 49.

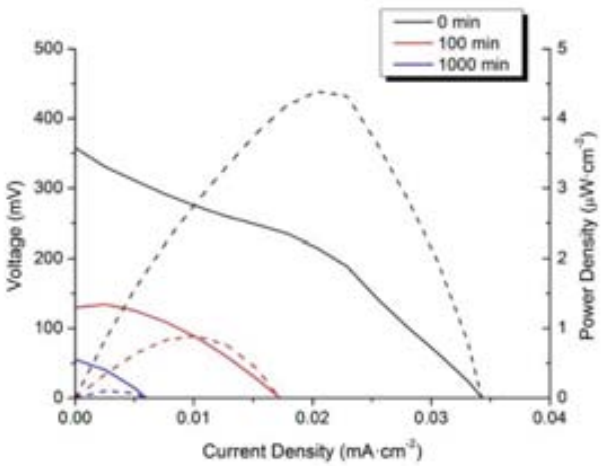

Figure 49. i-V and i-P graphs for a miniaturized microbial fuel cell with flat gold electrodes.

4.5.2. Miniaturized microbial fuel cells with micropillar array electrodes

In this section different MFCs with different micropillar array electrodes where used to study how their electrical performance changes according to the geometry of the arrays used in comparison to a MFC with flat gold electrodes. The different MFCs where characterized with the same values of t_{wait} and t_{step} used to extract the electrical performance of a MFC with flat electrodes to restrict the changes only to the different geometries of the array electrodes used in each case.

Note that the tested miniaturized MFCs were not refilled with fresh fuel or TEA during the experiments (batch mode) because the goal of this work was mainly to study the gain in the electrical performance stemming from the use of fully-conducting micropillar array electrodes, in contrast to flat electrodes. Future work contemplates the design and fabrication of microfluidic microbial fuel cells with micropillar array electrodes, and in that case a constant flow of fuel and TEA will be possible. The resulting i-V and i-P graphs for these experiments at three different times are showed in Figure 50.

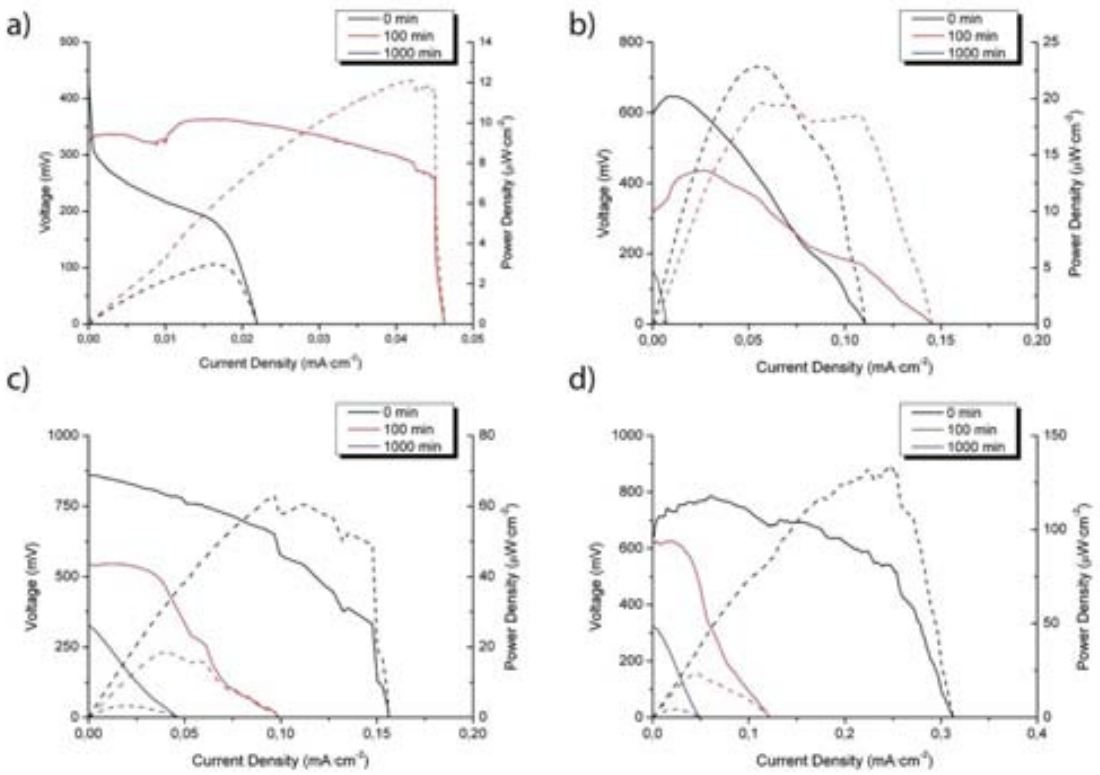

Figure 50. i-V and i-P graphs for different micropillar array electrodes with centre-to-centre distance d = 100 µm, radius $r_{\mu Pill}$ = 10 µm, and height $h_{\mu Pill}$ a) 5 µm, b) 25 µm, c) 50 µm and d) 125 µm.

Comparing the results obtained with MFCs with micropillar array electrodes with the analogous cells mounting with flat electrodes, it is clear that micropillar arrays improve

the electrical performance at short and medium times, although for long operation times the performance is close to the case of a miniaturized MFC with flat electrodes. Note that the performance of these fuel cells also depends on the geometry of the array. Figure 51 summarizes the key information from the i-V graphs showed in Figure 50 showing only maximum current density, maximum power density, and OCV as function of micropillar height at three different times.

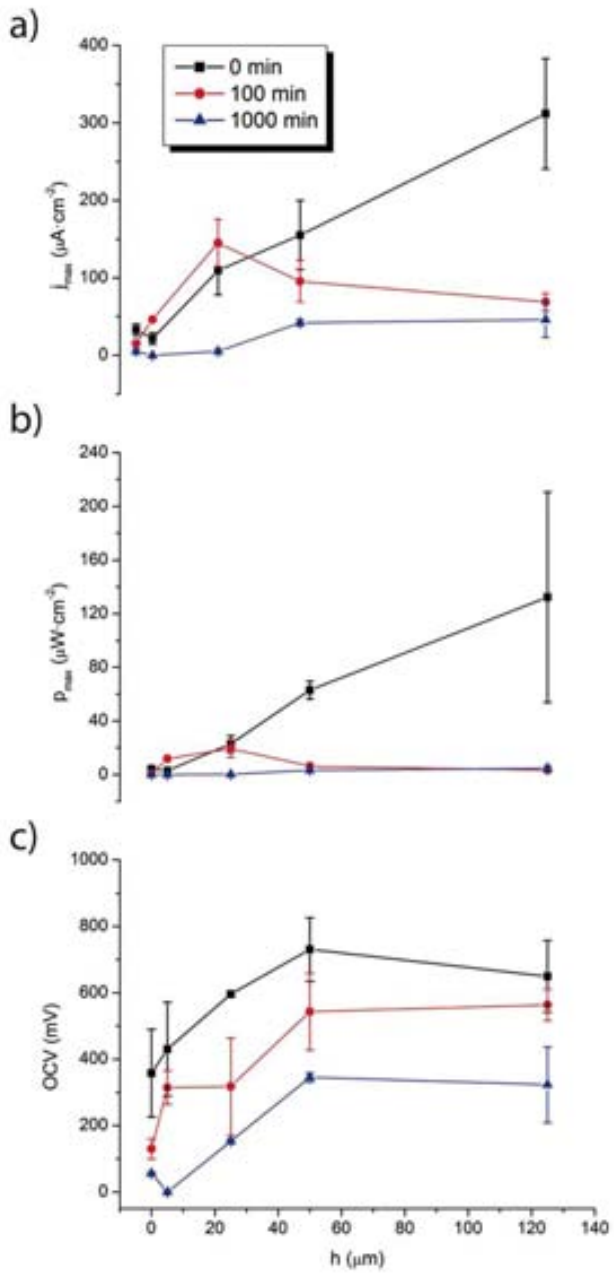

Figure 51. Maximum current density a), maximum power density b) and OCV c) as function of the height for the different micropillars array electrodes and the time of the experiment.

The maximum current density in these miniaturized MFCs improves with micropillar array electrodes, particularly at short times, see Figure 51 *a)*. The current density increases almost linearly with the micropillar height. This is due to the concentration of

the micropillars side-wall to the current. This effect appears because the higher the micropillars are, the bigger the real area of the electrode causing that the amount of contact points with the biocatalyst. This linear improvement with micropillar height is only seen at short operation times (for times lower than 10 minutes); at medium and long times the current density is still bigger than for the case of a MFC with flat electrodes, but the maximum current density approaches the level of a MFC with flat electrodes. This is in line with the results presented in chapter 2 for the voltammetric and chronoamperometric experiments.

The maximum power density shown in Figure 51 *b)* presents a similar trend to that of the maximum current density. It also improves with micropillar array electrodes in comparison to a MFC with flat electrodes. In this case the power density only shows significant improvement at short operation times. At longer times the power density decreases and its value becomes approximately the same than for a MFC with flat electrodes. Note that the current density and aslo the power density were calculated using the projected area of the electrodes in the MFCs, that in this case is a circle of 2.5 mm of diameter. Finally the trend of the OCV with the height of the micropillars is showed in Figure 51 *c)*. The OCV increases 250 mV from the value obtained for a MFC with flat electrodes up to for an array with 50 µm micropillars. From this height the OCV keeps approximately a constant value independently the height of the micropillars. The explanation why the OCV increases with micropillar height may be found in Nerst's equation which establishes a relationship between the concentration of the electroactive species in a solution and the electrochemical potential. As was seen in chapter 2 the amount of material confined between micropillars at a given time depends on their height causing different material consumption speeds concluding that the higher the microstructures are, the longer the confined material takes to be consumed. So the produced voltage is bigger for those array electrodes with the highest micropillars because the material between pillars is consumed more rapidly, affecting the local concentration potential.

This phenomenon may be related to thin layer effects, and is also in agreement with the data showed in chapter 2 where the peak-to-peak potential separation decreased as function of the geometry of the array until reaching a minimum level voltage. From this point, independently of the geometry, the value of the peak-to-peak potential separation did not decrease any more. Also Henstridge et al. [190] studied this phenomenon at porous and micropillar array electrodes and found that it is caused by thin-layer effects; that is the depletion of electroactive species confined in a small volume. Regarding the dependence with the elapsed time of the experiment, the OCV also decreases as function of the time the experiment is running, eventually approaching to the value of the OCV achieved for a miniaturized MFC with flat gold

electrodes. The graphs show large y-error bars because of the big dispersion existing in the determination of bacteria that was measured for each of the experiments. This big dispersion might be due to slight temperature gradients during the process of growing bacteria, or also during the performance of the experiments.

The reason why miniaturized MFCs give the maximum electrical efficiency only during the early stages of an experiment is explained by the rapid consumption of reagents at fully-conducting micropillar array electrodes trending to a planar response rapidly. Bear in mind that the experiments were performed in batch-mode and that the fuel was not being constantly supplied to the fuel cell. Another issue comes from the low volume of the anode and the cathode providing low volume of the analyte and the catholyte. Both of them cause that the chemicals necessary for the correct operation of the MFCs would be consumed fast, and as a consequence the maximum electrical performance of our miniaturized MFCs decreases rapidly.

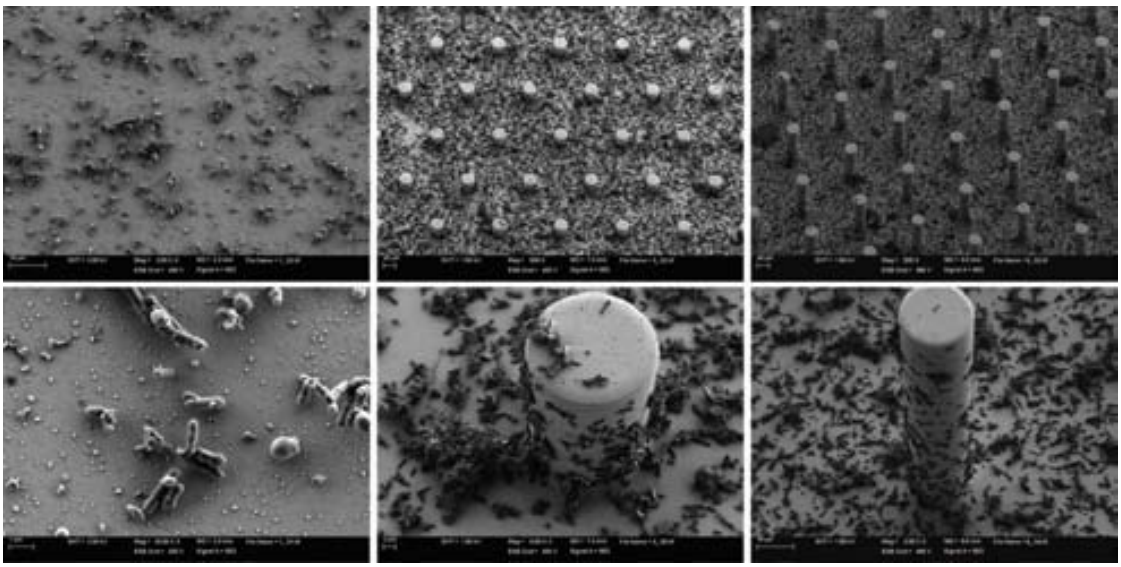

Figure 52. SEM images of the micropillar array electrodes used after finishing the experiments.

4.5.3. Miniaturized microbial fuel cells with densely packed micropillar arrays electrodes. Limitations affecting the choice of the micropillar array electrodes

With the aim of improving the power density more miniaturized microbial fuel cells were tested using in this case array electrodes with closer micropillar than the use in the previous section. From the theoretical and experimental results presented in chapter 2 we concluded that the amount of micropillars in an array affects both the current density and also the peak potential separation. From these results we concluded that the closer the micropillars are, the higher the generated current density and the more reversible the electrode is. The geometries of these micropillar array electrodes are summarized in Table 12.

Table 12. Geometries used to improve the electrical performance of these miniaturized MFCs.

Geometry	$r_{\mu Pill}$ (µm)	d (µm)	$h_{\mu Pill}$ (µm)
A	5	10	25
B	5	40	5

Following the same experimental procedure and using the same set-up than for the last experiments these miniaturized microbial fuel cell were also tested; Figure 53 shows the i-V and i-P graphs for these arrays. From the i-V and i-P graphs in Figure 53 we can see that all of these MFCs with micropillar arrays electrodes perform worse than flat electrodes. These unexpected results can be explained by the same phenomenon observed in section 2.4.3.3. That section showed that the performance of an array with dimensionless center-to-center separation of R = 2 and dimensionless heights of Z = 25 did not fit the results obtained in the simulations. It was due to the micropillars not being entirely wetted by the solution because the surface tension between micropillars was high.

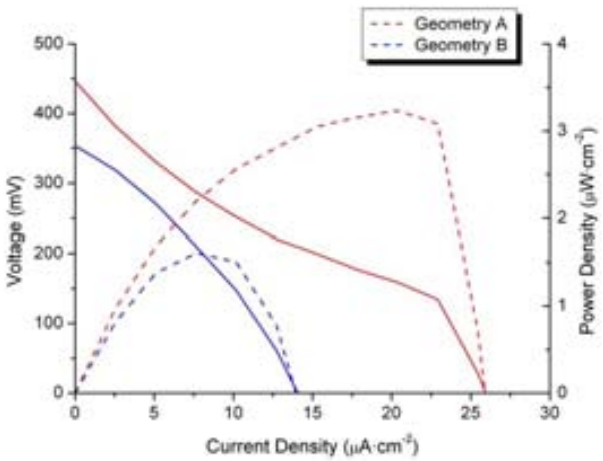

Figure 53. i-V and i-P graphs for two MFCs with the micropillar array electrodes showed in Table 12.

Another possibility is that the bacteria, which size is up to 3 microns [191], cannot have contact with the side-walls of the micropillars because the space between micropillars is small for them to access tha gap between, so the only working area for these array electrodes is the top of the micropillars. Figure 54 graphically describes this phenomenon.

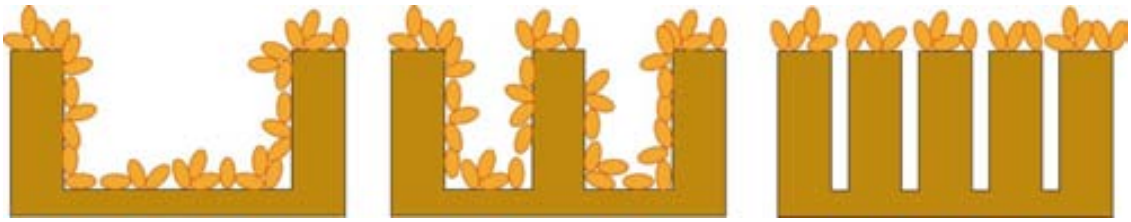

Figure 54. Different cases of covering micropillars array electrodes with bacteria.

Figure 54 *a)* shows an array with separate micropillars. In this case the bacteria can contact with the side-walls of the micropillars and also with the bottom of the electrodes because the space between micropillars is big enough. In contrast to Figure 54 *b)* the gaps between micropillars are so small where that the bacteria cannot contact neither with the side-walls of the micropillars nor with the bottom of the electrode. This little space between micropillars causes that the bacteria can only have contact with the top of the micropillars reducing the operational surface of the electrode resulting in a lower surface than a flat electrode. As a consequence a MFC with array electrode with close micropillars will be offer a worse electrical performance than the same MFC with flat electrodes.

4.6. Fabrication of a power source based on miniaturized microbial fuel cells

To finish this chapter the design of a power source composed by miniaturized MFCs was proposed with the goal of switching on an electrochromic display. An electrochromic display is a device that is able to reversibly change its color thanks to the use of electrochromic materials such as polyaniline or tungsten oxide. These materials can change they own color by the absorption or injection of electrons depending on the polarization of the external power source the device is connected.

To minimize the difficulties regarding the minimum voltage and current needed to switch on this display the proposed power source was built using miniaturized MFCs with micropillar array electrodes whose geometry was equal to $r_{\mu Pill}$ = 10 µm, d = 100 µm and $h_{\mu Pill}$ = 125 µm. This geometry was chosen because these miniaturized MFCs supply the highest output power delivering a voltage and current of 540 mV and 0.05 mA respectively. The final power source, Figure 55, was composed by an array of three columns and three rows of MFCs that provided 1.5 V and 0.15 mA approximately.

The miniaturized MFCs composing each column were connected to each other using copper tape with adhesive on both sides. To isolate the columns PSA stripes with adhesive on both sides were placed between adjacent columns. Finally copper tape was used again to interconnect all the columns to each other. The bottom of Figure 55 shows a sequence of three images to provide evidence that the design of the power source based on the miniaturized MFC presented in this chapter is working. In this

sequence a segment of this display appears slowly whereas the supplied output power from the source is applied between its terminals.

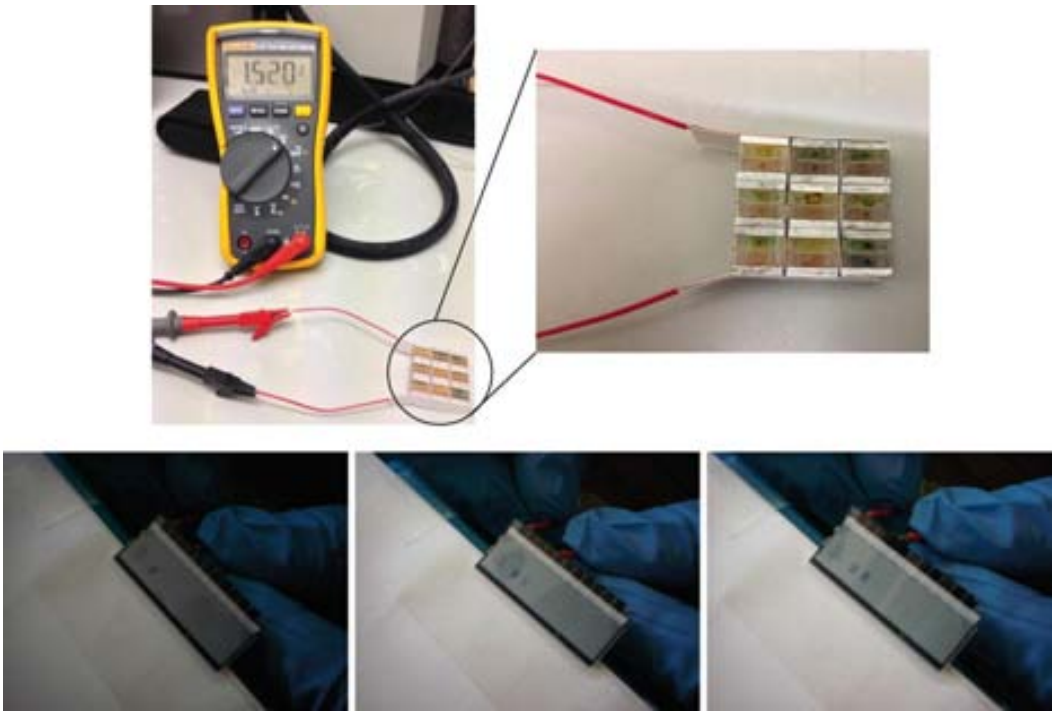

Figure 55. Final power source composed by nine MFCs to switch on an electrochromic display.

4.6. Conclusions

In this chapter the fully-conducting micropillar array electrodes designed, fabricated and characterized in chapter 2 have been used to increase the electrical performance of miniaturized microbial fuel cells.

Before starting the electrical characterization an instrumentation system was created to get the i-V and i-P graphs, and also the voltage at a given constant current for four miniaturized microbial fuel cells working in parallel. This system is composed by a routine developed with Labview and two Keithley 2612 connected both of them to a computer by GPIB. The routine programs each one of the two Keithley sending the specific instructions through the GPIB interface to measure the voltage with a specific constant current for the different four MFCs during a specific time.

To achieve the goal of this chapter miniaturized microbial fuel cells with a volume of 1 cm^3 were fabricated by rapid-prototyping techniques using a milling machine and a cutter plotter. The fabrication of these miniaturized MFCs was done by milling and drilling pieces of PMMA (Polymethylmethacrylate) and pieces of aluminum to create the reactors and the holders for the electrodes respectively. To assemble and seal the different pieces adhesive plastic sheets were cut by a cutter plotter. Besides cooper adhesive tape was used to allow electrical conductivity between the aluminum holder and the electrodes. The electrodes used to develop the miniaturized MFCs were the same fully-conducting gold micropillar array electrodes fabricated and characterized in the chapter 2. They were used to achieve high values of voltage, current density and power density despite the low size of the final microbial fuel cells fabricated.

Our results show that the maximum power density and also the current density achieved for our devices are 132.31 $\mu W \cdot cm^{-2}$ and 310 $\mu A \cdot cm^{-2}$ respectively. These results represent the largest power and current densities reported to date for an MFC, however the maximum performance is only kept for a short period of time because of the following design limitations. The first one regards to the low volume of both the reactors which both of them only permit to host a low volume of analyte and catholyte. The second refers to the rapid consumption of the mass which is usual at fully-conducting micropillar array electrodes. Moreover the experiments were done without refilling with fresh reactants what also caused the degradation of the performance of our devices. In addition to the design the design of the micropillar array plays an important role because the distance between them must be enough to permit that the bacteria can contact with the side-walls of the micropillars.

The last section of this chapter demonstrates that the power generated by these MFCs is sufficient to switch on an electrochromic display, thus showing that the miniaturized

microbial fuel cells developed in this chapter can be used in very low power electrical applications.

Possibly the future of microbial fuel cells is not in the generation of electricity at large, or even at small scale because these cells can deliver very little power. However their use in the purification of water is a reality, and currently a lot of work is being done towards the development of new materials to be applied in water purification plants based on microbial fuel cells. Although the miniaturized microbial fuel cells developed in this chapter cannot provide very much electrical power, the micropatterned electrodes from chapter 2 can be also used in other types of fuel cells such as methanol or ethanol fuel cells to increase the output power density.

Regarding the future of the large-scale fabrication of micropillar array electrodes it should be based on using polymeric substrates, because it will drastically decrease the cost of the fabrication. One method to achieve this is using a silicon master mould to transfer this architecture to a polymeric substrate. Another route to have micropillar array electrodes is by photolithography what will give tallest microstructures. However, the adhesion of the metal layer is a problem in both routes because polymers present low roughness what will need further research to find out the best solution to solve this problem. Once the adhesion problem is solved, these new fully-conducting micropillar array electrodes may be used in Proton Exchange Membrane (PEM) microfluidic fuel cells fabricated by rapid-prototyping techniques such in chapter 4. This microfluidic architecture might increase the lifespan and also the output power thanks to the constant delivering of fresh Terminal Electron Acceptor (TEA) that will help the transport of electrons, and the constant delivering and removing of chemicals and fuel between micropillars. Also, if the bacteria are constantly fed with fuel they may create a biofilm which will likely increase the electrical current generation at the anode [192]. Note that the use of a PEM will be necessary to avoid the contamination of the anode with the TEA because it may affect, or also kill the bacteria.

In addition to the development of microfluidic microbial fuel cells with fully-conducting micropillar array electrodes Mr. Igor Schmidt, a PhD student at the sustainable chemistry & energy research group at Technische Universtität Braunschweig under the supervision of Professor Uwe Schröder, is following the work I started there regarding how to grow biofilms at micropillar array electrodes. Also, note that Mr. Schmidt used this work for his master dissertation entitled, "*Spektroelektrochemische Untersuchungen an aus Abwasser angereicherten Biofilmen" (Technische Universität Braunschweig, Braunschweig, Germany, 2013)*. The results presented in this master thesis show that the current density does not increase with micropillars with

separations of 20 µm and 50 µm in comparison with the values obtained with flat electrodes, what reaffirm the results showed in section 4.5.3.

Annex 1. Cylindrical coordinates

The rectangular coordinate system and cylindrical system are showed in Figure 56.

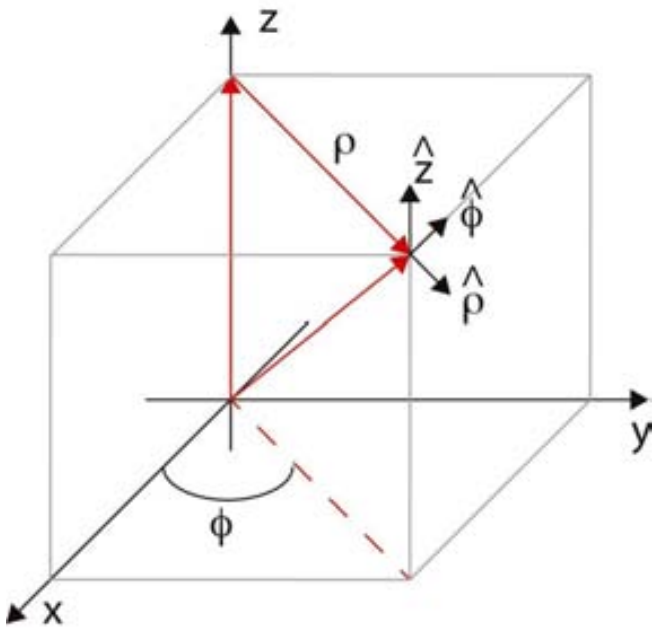

Figure 56. Rectangular and cylindrical coordinate system.

Transformations

$$\rho = \sqrt{x^2 + y^2} \quad \text{(A1)}$$

$$\phi = \arctan(y/x) \quad \text{(A2)}$$

$$z = z \quad \text{(A3)}$$

Unit Vectors

$$\hat{\rho} = \hat{x}Cos\phi + \hat{y}Sin\phi \quad \text{(A4)}$$

$$\hat{\phi} = \hat{y}Cos\phi - \hat{x}Sin\phi \quad \text{(A5)}$$

$$\hat{z} = \hat{z} \quad \text{(A6)}$$

Annex 2. PPF etch rates by O_2 plasma process

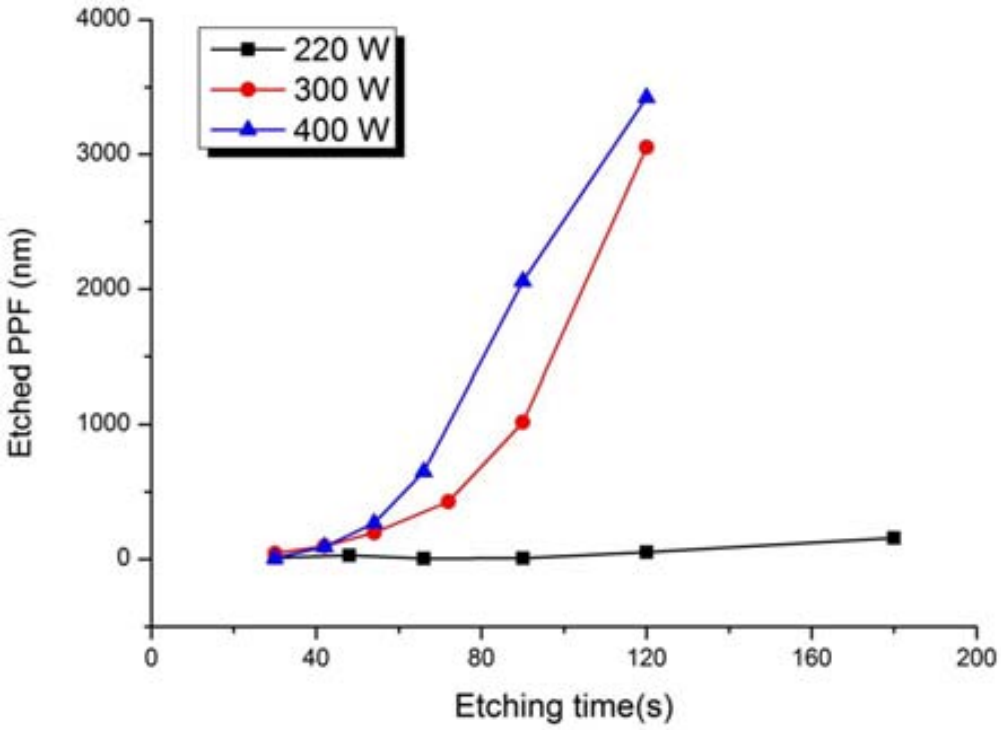

Figure 57. PPF etching speed after an O_2 plasma process.

Annex 3. Papers included in this thesis

1. *N. Uría, **D. Sánchez**, R. Mas, O. Sánchez, F.X. Muñoz, J. Mas, Effect of the cathode/anode ratio and the choice of cathode catalyst on the performance of microbial fuel cell transducers for the determination of microbial activity, Sensors and Actuators B: Chemical, 170 (2012) 88-94*

2. *R. Prehn, L. Abad, **D. Sánchez-Molas**, M. Duch, N. Sabaté, F. J. del Campo, F. X. Muñoz, and R. G. Compton, "Microfabrication and characterization of cylinder micropillar array electrodes," Journal of Electroanalytical Chemistry, vol. 662, pp. 361-370, 2011.*

3. ***D. Sánchez-Molas**, J. P. Esquivel, N. Sabaté, F. X. Muñoz, and F. J. del Campo, "High Aspect-Ratio, Fully Conducting Gold Micropillar Array Electrodes: Silicon Micromachining and Electrochemical Characterization," in The Journal of Physical Chemistry C, ed, 2012*

4. ***D. Sánchez-Molas**, J. Cases-Utrera, P. Godignon, and F. Javier del Campo, "Mercury detection at microfabricated pyrolyzed photoresist film (PPF) disk electrodes," Sensors and Actuators B: Chemical, vol. 186, pp. 293-299, 2013.*

5. *M. J. González-Guerrero, J. P. Esquivel, **D. Sánchez-Molas**, P. Godignon, F. X. Muñoz, F. J. del. Campo, F. Giroud, S. D. Minteer, and N. Sabate, "Membraneless Glucose/O2 Microfluidic Enzymatic Biofuel Cells using Pyrolyzed Photoresist Film Electrodes " Lab on a chip, 2013.*

Sensors and Actuators B 170 (2012) 88–94

Contents lists available at ScienceDirect

Sensors and Actuators B: Chemical

journal homepage: www.elsevier.com/locate/snb

Effect of the cathode/anode ratio and the choice of cathode catalyst on the performance of microbial fuel cell transducers for the determination of microbial activity

Naroa Uría [a,*], David Sánchez [b], Roser Mas [b], Olga Sánchez [a], Francesc Xavier Muñoz [b], Jordi Mas [a]

[a] Group of Environmental Microbiology, Universitat Autònoma de Barcelona, Bellaterra, Spain
[b] Centro Nacional de Microelectrónica (CNM-IMB) CSIC, Spain

ARTICLE INFO

Article history:
Received 30 September 2010
Received in revised form 1 February 2011
Accepted 12 February 2011
Available online 24 February 2011

Keywords:
Microbial fuel cell
Microbial activity
Biosensor

ABSTRACT

Microbial activity can be measured using sensors based on microbial fuel cell technology. In these sensors, microorganisms in contact with the anode generate a current proportional to their metabolic activity. Proper operation of such a device requires that activity at the anode is not impaired by the ability of the cathode to transfer current to the cathodic electron acceptor. Therefore, we have determined the minimum cathode to anode ratio required for unhindered performance of the microbial fuel cell. Our results indicate that for the same level of biological activity, the optimal cathode/anode ratios depend on the type of cathode being used. Thus, while carbon paper/ferricyanide cathodes require ratios of 4, platinum cathodes need much higher ratios of about 27. Cyclic voltammetry measurements indicate that platinum cathodes have a much slower dynamic behaviour than cathodes based on carbon paper/ferricyanide. While these results indicate that carbon paper/ferricyanide cathodes provide the most current for the same cathode area, extended experiments carried over a period of several days indicate a progressive degradation of fuel cell performance in cells using iron catalysts. Overall, our conclusion is that soluble iron-based catalysts provide much higher power output than solid phase platinum catalysts, but at the expense of a reduced life span which limits their use for applications requiring extended operation.

1. Introduction

During recent years, a number of different sensor types using impedance spectroscopy, fluorescence or optical density have been proposed for the detection and quantification of microbial biomass in liquid samples. In some instances, the models proposed have actually been commercialized. However, efficient systems for the quantification of bacterial activity have not yet been described.

Microbial fuel cells (MFCs) provide a viable transducing mechanism for the determination of microbial activity in liquid samples. In some specific instances, the principle has been used for specific applications such as detection of toxicity [1–3]. Utilization of MFCs as sensing devices requires however their ability to respond to changes in the level of biological activity present in the anode compartment. The problem is that power output, and therefore signal output of a MFC is also dependent on several other factors. Between them, the surface area of the proton exchange membrane (PEM) and the relative sizes of the anode and cathode seem to play an important role [4]. The power values obtained are usually normalized in order to make the efficiency of power production by different MFCs comparable. In many studies, this normalization is carried using the surface area of the anode, assuming that bacterial activity limits power output. However, recent reports demonstrating that tripling the surface area of the cathode increased power density by 22% [4,5] indicate otherwise.

Additionally, the choice of the cathode material is another factor to consider depending on the application [6]. For oxygen reduction different cathode materials have been proposed. Platinum is the best known [7]. However, due to its high cost [8], tendency to poisoning by the formation of a platinum oxide layer at the surface [6,9,10], and sensitivity to biological and chemical fouling [11,12], platinum based electrodes are not useful for all applications. For this reason, different and cheaper alternatives to noble metal catalyst have been studied such as pyrolysed iron (II) phthalocyanine (Pyr-FePc) and cobalt tetramethoxyphenylporphyrin (CoTMPP) applied on graphite cathodes [9,13].

Other materials such as carbon paper or graphite can also be used with a soluble catalyst which accelerates the poor oxygen reaction on these electrode materials. The couple ferric/ferrous iron is a good electron mediator for oxygen reduction for three reasons:

* Corresponding author at: Department of Genetics and Microbiology, Autonomous University of Barcelona, 08193 Bellaterra, Spain.
Tel.: +34 935 813 011, fax: +34 935 812 387.
E-mail address: naroa.uria@uab.cat (N. Uría).

0925-4005/$ – see front matter © 2011 Elsevier B.V. All rights reserved.
doi:10.1016/j.snb.2011.02.030

Journal of Electroanalytical Chemistry 662 (2011) 361–370

Contents lists available at SciVerse ScienceDirect

Journal of Electroanalytical Chemistry

journal homepage: www.elsevier.com/locate/jelechem

Microfabrication and characterization of cylinder micropillar array electrodes

Ricard Prehn [a], Llibertat Abad [a], David Sánchez-Molas [a], Marta Duch [a], Neus Sabaté [a], F. Javier del Campo [a,*], Francesc Xavier Muñoz [a], Richard G. Compton [b]

[a] Instituto de Microelectrónica de Barcelona, IMB-CNM (CSIC), Esfera UAB, Campus Universitat Autònoma de Barcelona, 08193 Bellaterra, Barcelona, Spain
[b] Department of Chemistry, Physical and Theoretical Chemistry Laboratory, Oxford University, South Parks Road, Oxford OX1 3QZ, United Kingdom

ARTICLE INFO

Article history:
Received 22 July 2011
Accepted 4 September 2011
Available online 22 September 2011

Keywords:
Microfabrication
Electrochemistry
Micropillar array electrodes
Diffusion domain approach
Microelectrodes

ABSTRACT

This work describes de fabrication, using standard microfabrication techniques, of cylindrical micropillar array electrodes. The work also describes the characterization of these electrodes using a combination of microscopy techniques, cyclic voltammetry and finite-element simulations based on the diffusion domain approach. The work shows that while micropillar array electrodes display currents consistent with the Randles-Ševčík equation at low scan rates, they afford enhanced voltammetric peak currents at higher scan rates. Not only this, but for certain micropillar geometries and densities, simulations predict that a voltammetric peak-to-peak separations below 57 mV due to thin-layer diffusion effects. The results presented in this article are in agreement with recent works by Compton and co-workers on porous and rough electrodes, and provide further evidence of the validity of the diffusion domain approach to predict and interpret mass transport controlled currents at microstructured electrodes.

1. Introduction

Advances in microfabrication have made photolithography-based processes available far beyond the realms of microelectronics. One important example is the fabrication of microelectrode arrays and microstructured electrodes, the latter of which are the subject of this work. This article describes the fabrication, using a combination of microfabrication techniques and electroplating, of cylinder micropillar arrays. The characterization of the latter has been performed using different microscopy techniques and cyclic voltammetry, and the voltammetric response has been simulated using commercial finite element software.

Three-dimensional electrochemical interfaces are very valuable in electroanalysis, fuel cell development, and electrophysiology. They are important because they provide a much larger surface area than planar electrodes, and this leads to higher sensitivities, higher current collections, and lower impedance. In certain electroanalytical applications, such as biosensors, using electrodes with a larger surface area means that more bioactive material can be immobilized on the electrode, which increases sensitivity and biosensor lifetime [1]. In adsorptive stripping analysis, where the analyte is pre-concentrated on the electrode surface [2], using electrodes of larger surface area facilitates the incorporation of more analyte, as shown in rough glassy carbon electrodes [3].

Fuel cells are another kind of electrochemical devices where electrodes with larger surface area provide benefits in terms of higher currents, higher power generation, or higher fuel consumption efficiencies [4]. In this sense, many works have recently appeared where the fabrication of micro- and nano-patterned electrodes is presented for energy generation and storage [4–7].

Last, 3D electrodes are also used in electrophysiology [8–11]. These works typically analyze the response of nervous cells [12–14] or tissues to certain stimuli, such as the addition of antibiotics [15], toxics [16], or neurotransmitters [17]. The fragile nature of these cells and tissues requires that nutrients be supplied to them under very well controlled conditions. Thus, planar microelectrodes, which are easy to manufacture, are unsuitable because they limit the access of nutrients considerably. On the other hand, porous electrodes and micropillar arrays a very attractive alternative because they allow the supply of nutrients to the cells while measurements are being made [18].

Cylindrical micropillar structures have found use in a range of different applications, such as lab on a chip components, such as microfluidic pumps [19], and separators [20,21], and sample preconcentrators and detectors [1]. Micropillars structures are also of importance in optics, where they enable the development of novel LEDs [22] and quantum dots [23].

Photolithography allows the design and fabrication of specific surface structures that make it easier to study the effects of surface structure on electrochemistry in a controlled and systematic way. The microcylinders used to make the electrodes in this study were grown by electrodeposition over gold macroelectrodes, using a template of lithographically patterned resist.

In addition to the microfabrication of microcylinder array electrodes, this work applies the diffusion domain approach [24,25] to

* Corresponding author. Tel.: +34 93 594 77 00x2406; fax: +34 93 580 14 96.
E-mail address: javier.delcampo@csic.es (F.J. del Campo).

1572-6657/$ - see front matter © 2011 Elsevier B.V. All rights reserved.
doi:10.1016/j.jelechem.2011.09.002

THE JOURNAL OF PHYSICAL CHEMISTRY C

Article

pubs.acs.org/JPCC

High Aspect-Ratio, Fully Conducting Gold Micropillar Array Electrodes: Silicon Micromachining and Electrochemical Characterization

David Sánchez-Molas, Juan Pablo Esquivel, Neus Sabaté, F. Xavier Muñoz, and F. Javier del Campo*

Instituto de Microelectrónica de Barcelona, Centro Nacional de Microelectrónica, IMB-CNM (CSIC), Esfera UAB, Campus Universitat Autònoma de Barcelona, 08193 Bellaterra, Barcelona, Spain

Supporting Information

ABSTRACT: In this paper we describe the design, fabrication, and characterization of cylindrical gold micropillar array electrodes. Micropillar array electrodes bring about several advantages compared to planar electrodes and microelectrode arrays, as they provide a much larger surface area than the latter devices. Micropillar array electrodes are closely related to porous electrodes, as suggested by the recent literature and as our experimental results show. We fabricated a number of different gold micropillar array structures using standard microfabrication techniques, particularly DRIE plasma etching, thermal oxidations, and gold metallization by dc sputtering. Experimental results were compared with simulations, and very good agreement was found. This served both to validate the diffusion domain approximation for these particular devices and also to deepen our understanding on the modes of mass transport controlling the current response of these devices. We found that planar diffusion dominates the response of these devices and that thin layer diffusion effects play a crucial role and are responsible for both displacing the position of the peaks and narrowing the peak-to-peak separation in cyclic voltammograms. These effects arise only as a result of the surface topology and should not be mistaken by catalytic effects.

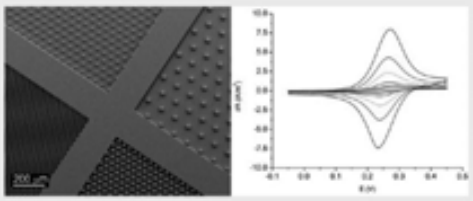

INTRODUCTION

The use of microfabrication techniques in electrochemistry has given birth to many new devices, such as microelectrodes,[1] nanoelectrodes and their arrays,[2−6] and an entire research area known as lab on a chip[7] that includes microreactors and miniaturized fuel cells.[8−11] Most of these devices have found application in the field of electroanalysis in the form of chemical sensors and biosensors[1] but also as tools for the study of fundamental phenomena at the micro- and nanoscale. Micro- and nano-fabrication techniques allow the production of micro- and nanoelectrode arrays, which are two-dimensional ensembles of a large number of small electrodes connected in parallel. Among the virtues of micro- and nanoelectrode arrays is the level of signal amplification provided compared to single micro- or nanoelectrodes, while keeping some of the mass transport characteristics of the individual units composing them. Thus, in the case of microelectrode arrays, the signals are comparable to those of macroelectrodes of the same size (as the array);[12] similarly, nanoelectrode arrays show current responses comparable to microelectrodes of the same surface area as that taken by the array.[2] When designing and constructing micro- and nanoelectrode arrays the goal is to take advantage of hemispherical diffusion to each component of the array for as long as possible before the diffusion layers of adjacent micro- or nanoelectrodes overlap, and therefore avoid that the current response becomes controlled by planar diffusion to the whole array.

Microelectrode arrays are inherently two-dimensional devices. Although this suffices for most applications, occasionally it is desirable to increase the active surface within a given area. This is so in the case of certain sensing applications in which the detection event depends heavily on the surface area available.[13,14] It is also the case in the development of new electrodes for fuel cells,[15,16] where a large power output is needed. This work aims to improve the efficiency of biofilm-based microbial fuel cells.[17−19] In these devices, the bacteria in a biofilm grown directly on an electrode are responsible for the generation of electricity, as they metabolize organic matter in a solution. Microbial fuel cells currently provide some of the lowest power densities (0.175 mA/cm^2) compared to methanol fuel cells (300 mA/cm^2).[20,21] This has relegated them to the position of an auxiliary process to lower the cost of more important processes such as water purification,[22,23] desalination,[24] or hydrogen production,[25,26] to name but three. As biofilms grow thicker, the areas closer to the electrode and further from the biofilm−solution interface become poorer in oxygen and nutrients, which leads to a decrease in the number of electrons that the bacteria in those regions can supply to the electrode. Therefore, to improve the power output of these devices, in addition to increasing the contact area between the biofilm and the electrode, it might be useful to probe

Received: May 31, 2012
Revised: July 27, 2012

dx.doi.org/10.1021/jp305339r | J. Phys. Chem. C XXXX, XXX, XXX−XXX

Sensors and Actuators B 186 (2013) 293–299

Contents lists available at SciVerse ScienceDirect

Sensors and Actuators B: Chemical

journal homepage: www.elsevier.com/locate/snb

Mercury detection at microfabricated pyrolyzed photoresist film (PPF) disk electrodes

David Sánchez-Molas, Joana Cases-Utrera, Philippe Godignon, F. Javier del Campo*

Instituto de Microelectrónica de Barcelona, IMB-CNM (CSIC), Esfera UAB, Campus Universitat Autónoma de Barcelona, 08193 Bellaterra, Barcelona, Spain

ARTICLE INFO

Article history:
Received 15 March 2013
Received in revised form 21 May 2013
Accepted 4 June 2013
Available online xxx

Keywords:
Pyrolyzed photoresist films
PPF
Disk electrodes
Passivation
Glassy carbon electrodes
Mercury detection

ABSTRACT

This work describes a method to passivate pyrolized photoresist films (PPF) to microfabricate electrodes suitable for electrochemical applications. The work describes the passivation process in detail, which entails pre-treating the PPF structures with mild ammonia plasma followed by silanization with SiH_4 to promote the adhesion of the passivation layer. The working condition of these electrodes is demonstrated by the detection of mercury in aqueous solutions (pH = 1.5) down to 2 ppb. We discuss possible ways to improve the passivation of PPF that will lead to more complex structures and devices made in this material. The dynamic range of the method described here is already analytically useful, but we suggest ways to shorten the time of analysis and push the detection limit below 1 ppb using PPF electrodes.

1. Introduction

Building on our previous experience in the fabrication of pyrolyzed photoresist films (PPF) [1,2], we present in this work the wafer-level fabrication of PPF disk electrodes with special emphasis in a new route to passivate PPF structures consisting of a mixed layer of silicon oxide and silicon nitride [3], and the subsequent patterning of this passivation layer by means of additional lithographic and etching steps.

PPF is an amorphous carbon material closely related to glassy carbon [4], although it is easier and less costly to produce [5,6]. PPF emerged as an interesting material for use in the manufacture of integrated circuits (IC) because its precursor photoresist could be easily patterned by lithography, and because its electrical properties can be controlled by the synthetic conditions [7–9]. Ten years later, Whitesides demonstrated the fabrication of carbon microstructures using polymeric precursors and PDMS micro-molds for application in microelectromechanical systems (MEMS) [10,11]. Around the same time, Kinoshita published the first electrochemical study on PPF electrodes [12]. Those same workers published a series of works describing electrochemical response of regular interdigitated PPF electrodes which bands were 50 μm wide and 500 μm long. Much smaller interdigitated structures on PPF by direct lithography have recently been reported by Madou and Shin, who have described the fabrication of nanobands that are 300 nm wide separated by a gap less than 2 μm [13]. Already in the 2000s, Madou and McCreery published a series of works on the electroanalytical properties of PPF electrodes [14,15].

In general PPF is synthesized either from positive or negative tone resists, although the pyrolysis of composite materials has recently shown to be feasible too [16]. Positive-tone, phenol-based resins yield more conducting PPF [8], but negative tone, epoxy-based resins, such as SU-8 allow the fabrication of thicker PPF, and are better suited for the construction of complex 3D structures [17]. Burckel et al. have recently described the fabrication of 3D structures using rapid thermal processes [18], and also have described the conversion of PPF 3D structures into graphene [19].

The passivation of PPF is a difficult task for three reasons. First, because RTP synthesized PPF structures are much more weakly bound to the silicon wafer than the original photoresist coating [20]. This requires careful wafer handling throughout the process, but particularly during those operations involving immersion in solvents, such as during resist development in lithography, or during rinsing steps. Second, because the smoothness of the PPF surface greatly hampers the adhesion of the passivation layer, making it necessary to pre-treat the surface and, third, because PPF is a low density material that is easily etched by a range of plasmas used in common reactive ion etching (RIE) processes [21].

Except for a few works [22,23] where an SU-8 passivation is used to define the active area of an interdigitated microband array and its contacts, and the recent work of Park et al. describing a SiO_2 passivation of PPF [24], the fact is that the connections of most

* Corresponding author. Tel.: +93 594 77 00x2406; fax: +93 580 14 96.
E-mail address: javier.delcampo@csic.es (F. Javier del Campo).

0925-4005/$ – see front matter © 2013 Elsevier B.V. All rights reserved.
http://dx.doi.org/10.1016/j.snb.2013.06.017

Lab on a Chip

RSC Publishing

PAPER

View Article Online
View Journal | View Issue

Membraneless glucose/O_2 microfluidic enzymatic biofuel cell using pyrolyzed photoresist film electrodes†

Cite this: *Lab Chip*, 2013, **13**, 2972

María José González-Guerrero,[a] Juan Pablo Esquivel,[a] David Sánchez-Molas,[a] Philippe Godignon,[a] Francesc Xavier Muñoz,[a] F. Javier del Campo,*[a] Fabien Giroud,[b] Shelley D. Minteer*[b] and Neus Sabaté*[a]

Biofuel cells typically yield lower power and are more difficult to fabricate than conventional fuel cells using inorganic catalysts. This work presents a glucose/O_2 microfluidic biofuel cell (MBFC) featuring pyrolyzed photoresist film (PPF) electrodes made on silicon wafers using a rapid thermal process, and subsequently encapsulated by rapid prototyping techniques into a double-Y-shaped microchannel made entirely of plastic. A ferrocenium-based polyethyleneimine polymer linked to glucose oxidase (GOx/Fc-C_6-LPEI) was used in the anode, while the cathode contained a mixture of laccase, anthracene-modified multi-walled carbon nanotubes, and tetrabutylammonium bromide-modified Nafion (MWCNTs/laccase/TBAB-Nafion). The cell performance was studied under different flow-rates, obtaining a maximum open circuit voltage of 0.54 ± 0.04 V and a maximum current density of 290 ± 28 μA cm^{-2} at room temperature under a flow rate of 70 μL min^{-1} representing a maximum power density of 64 ± 5 μW cm^{-2}. Although there is room for improvement, this is the best performance reported to date for a bioelectrode-based microfluidic enzymatic biofuel cell, and its materials and fabrication are amenable to mass production.

Received 8th March 2013,
Accepted 25th April 2013

DOI: 10.1039/c3lc50319d

www.rsc.org/loc

Introduction

Microfluidic fuel cells are a type of fuel cell where, due to the properties of laminar flow, fuel and oxidant streams flow in parallel without mixing. This avoids the need for a separation membrane (typically Nafion), it reduces internal ohmic losses,[1] and allows for different pHs at the anolyte and catholyte with little reagent crossover issues.[2,3] Other factors affecting the fuel cell's performance in addition to architecture are the catalysts and electrode materials, and the fuel used.[1,4]

Enzymatic fuel cells are promising future alternative sources of sustainable electrical energy under mild conditions, in which enzymes catalyze the transformation of chemicals into electrons, CO_2 and/or oxidized fuel by-products and water.[5–8] More specifically, glucose biofuel cells have been studied and developed for nearly 50 years.[9] In these fuel cells, glucose is the fuel oxidised at the anode while oxygen is reduced at the cathode. Glucose is bio-catalytically oxidized to gluconolactone by the enzyme glucose oxidase (GOx) or glucose dehydrogenase (GDH), and oxygen is reduced to water at the cathode by enzymes such as laccase and bilirubin oxidase.[10,11]

Glucose is a common energy source for all living organisms, making it possible to incorporate glucose-based devices for *in vivo* applications without the need of an external fuel feeding system.[12] This ability to work under physiological conditions compensates for their lower power output compared to fuel cells using inorganic catalysts, and it makes them the subject of active research in the area of implantable devices.

The two prevailing challenges of enzyme-based systems are short enzyme lifetimes, and their usually poor electron transfer rates to solid electrodes.[13,14] Enzyme lifetime may be increased if they are adequately immobilized on the electrode surface,[15–18] and although immobilized enzymes tend to display lower activity than in solution, a fuel cell with glucose oxidase and laccase electrodes was recently reported to yield power densities as high as 1 mW cm^{-2}.[19]

Different approaches exist to improve electron transfer between enzymes and electrodes, most of which rely on different forms of redox mediators, and more recently on the use of anthracene-modified carbon nanotubes for laccase enzymes.[11,14,20,21] Out of the conductive and functionalized materials examined for use in bioelectrodes,[13,20] the most favourable interfaces for biomolecular electron transfer are carbon-based materials. The use of carbon as an electrode material is widespread due to its low cost, large potential

[a]Instituto de Microelectrónica de Barcelona, IMB-CNM (CSIC), Campus de la Universidad Autónoma de Barcelona (Edifico UAB), 08193-Bellaterra, Barcelona, Spain. E-mail: javier.delcampo@csic.es; neus.sabate@imb-cnm.csic.es; Fax: +34 93 5801496; Tel: +34 93 5947700
[b]Departments of Chemistry and Materials Science and Engineering, University of Utah, 315 S 1400 E Rm 2020, Salt Lake City, UT 84112, USA. E-mail: minteer@chem.utah.edu; Fax: (801) 581-8433; Tel: (801) 587-8325

† Electronic supplementary information (ESI) available. See DOI: 10.1039/c3lc50319d

Bibliography

[1] A. J. Bard and L. R. Faulkner, *Electrochemical Methods. Fundamentals and Applications*, Second ed.: John Wiley and Sons, inc, 2000.

[2] A. C. Fisher, *Electrode Dynamics* vol. 34: Oxford Chemistry Primers, 1996.

[3] R. G. Compton and C. E. Banks, *Understanding Voltammetry*: Imperial College Press, 2011.

[4] J. Albery, *Electrode Kinetics*: Clarendon, 1975.

[5] C. Amatore, O. V. Klymenko, and I. Svir, "Importance of correct prediction of initial concentrations in voltammetric scans: contrasting roles of thermodynamics, kinetics, and natural convection," *Anal Chem,* vol. 84, pp. 2792-8, Mar 20 2012.

[6] C. Amatore, C. Pebay, L. Thouin, A. Wang, and J.-S. Warkocz, "Difference between Ultramicroelectrodes and Microelectrodes: Influence of Natural Convection," *Analytical Chemistry,* vol. 82, pp. 6933-6939, 2010.

[7] C. Amatore, C. Pebay, L. Thouin, and A. Wang, "Cyclic voltammetry at microelectrodes. Influence of natural convection on diffusion layers as characterized by in situ mapping of concentration profiles," *Electrochemistry Communications,* vol. 11, pp. 1269-1272, 2009.

[8] "Potentiostat Fundamentals," *Gamy Instruments. Application note,* 2010.

[9] "Basic overview of the working principle of a potentiostat/galvanostat (PGSTAT) – Electrochemical cell setup," *Metrohm. Autolab Application Note EC08,* 2011.

[10] D. Linden and T. B. Reddy, *Handbook of Batteries*, 3 ed.: Mc Graw-Hill, 2002.

[11] L. Carrette, K. A. Friedrich, and U. Stimming, "Fuel Cells: Principles, Types, Fuels and Applications," *ChemPhysChem,* vol. 1, pp. 162-193, 2000.

[12] J. P. Esquivel, N. Sabaté, A. Tarancón, N. Torres-Herrero, D. Dávila, J. Santander, I. Gràcia, and C. Cané, "Hybrid polymer electrolyte membrane for silicon-based micro fuel cells integration," *Journal of Micromechanics and Microengineering,* vol. 19, p. 065006, 2009.

[13] R. O'Hayre, S.-W. Cha, W. Colella, and F. B. Prinz, *Fuel Cell Fundamentals*: Wiley, 2006.

[14] T. Pichonat and B. Gauthier-Manuel, "Recent developments in MEMS-based miniature fuel cells," *Microsystem Technologies,* vol. 13, pp. 1671-1678, 2007.

[15] S. Numthuam, T. Kakegawa, T. Anada, A. Khademhosseini, H. Suzuki, and J. Fukuda, "Synergistic effects of micro/nano modifications on electrodes for microfluidic electrochemical ELISA," *Sensors and Actuators B: Chemical,* vol. 156, pp. 637-644, Aug 01 2011.

[16] M. W. Roberts, "Birth of the catalytic concept (1800-1900)," *Catalysis Letters,* vol. 67, pp. 1-4, 2000.

[17] B. E. Logan, B. Hamelers, R. Rozendal, U. Schröder, J. Keller, S. Freguia, P. Aelterman, W. Verstraete, and K. Rabaey, "Microbial Fuel Cells: Methodology and Technology," *American Chemical Society,* vol. 40, pp. 5181-5192, 2006.

[18] B. E. Logan, *Microbial Fuel Cells*: Wiley, 2008.

[19] B. E. Logan, "Exoelectrogenic bacteria that power microbial fuel cells," *Nature,* vol. 7, pp. 375-381, 2009.

[20] U. Schroder, "Anodic electron transfer mechanisms in microbial fuel cells and their energy efficiency," *Phys Chem Chem Phys,* vol. 9, pp. 2619-29, Jun 7 2007.

[21] K. M. Leung, G. Wanger, Q. Guo, Y. Gorby, G. Southam, W. M. Lau, and J. Yang, "Bacterial nanowires: conductive as silicon, soft as polymer," *Soft Matter,* vol. 7, p. 6617, 2011.

[22] T. Boesen and L. P. Nielsen, "Molecular dissection of bacterial nanowires," *MBio,* vol. 4, pp. e00270-13, 2013.

[23] K. Rabaey, N. Boon, S. D. Siciliano, M. Verhaege, and W. Verstraete, "Biofuel cells select for microbial consortia that self-mediate electron transfer," *Appl Environ Microbiol,* vol. 70, pp. 5373-82, Sep 2004.

[24] K. Rabaey and R. A. Rozendal, "Microbial electrosynthesis - revisiting the electrical route for microbial production," *Nat Rev Microbiol,* vol. 8, pp. 706-16, Oct 2010.

[25] S. Choi and J. Chae, "Optimal biofilm formation and power generation in a micro-sized microbial fuel cell (MFC)," *Sensors and Actuators A: Physical,* 2012.

[26] K. Dong, B. Jia, C. Yu, W. Dong, F. Du, and H. Liu, "Microbial fuel cell as power supply for implantable medical devices: a novel configuration design for simulating colonic environment," *Biosensors & bioelectronics,* vol. 41, pp. 916-9, Mar 15 2013.

[27] M. C. Hatzell, Y. Kim, and B. E. Logan, "Powering microbial electrolysis cells by capacitor circuits charged using microbial fuel cell," *Journal of Power Sources,* vol. 229, pp. 198-202, 2013.

[28] R. A. Timmers, D. P. B. T. B. Strik, H. V. M. Hamelers, and C. J. N. Buisman, "Electricity generation by a novel design tubular plant microbial fuel cell," *Biomass and Bioenergy,* 2013.

[29] D. Dávila, J. P. Esquivel, N. Sabaté, and J. Mas, "Silicon-based microfabricated microbial fuel cell toxicity sensor," *Biosensors & Bioelectronics,* vol. 26, pp. 2426-2430, 2011.

[30] N. E. Stein, K. J. Keesman, H. V. M. Hamelers, and G. v. Straten, "Kinetic models for detection of toxicity in a microbial fuel cell based biosensor," *Biosensors & Bioelectronics,* vol. 26, pp. 3115-3120, 2011.

[31] N. E. Stein, H. V. M. Hamelers, and C. N. J. Buisman, "The effect of different control mechanisms on the sensitivity and recovery time of a microbial fuel cell based biosensor," *Sensors and Actuators B: Chemical,* vol. 171-172, pp. 816-821, 2012.

[32] N. Uría, D. Sánchez, R. Mas, O. Sánchez, F. X. Muñoz, and J. Mas, "Effect of the cathode/anode ratio and the choice of cathode catalyst on the performance of

microbial fuel cell transducers for the determination of microbial activity," *Sensors and Actuators B: Chemical,* vol. 170, pp. 88-94, 2012.

[33] Z. Du, H. Li, and T. Gu, "A state of the art review on microbial fuel cells: A promising technology for wastewater treatment and bioenergy," *Biotechnology advances,* vol. 25, pp. 464-82, Sep-Oct 2007.

[34] S. E. Oh and B. E. Logan, "Hydrogen and electricity production from a food processing wastewater using fermentation and microbial fuel cell technologies," *Water research,* vol. 39, pp. 4673-82, Nov 2005.

[35] M. Mehanna, P. Kiely, D. Call, and B. Logan, "Microbial Electrodialysis Cell for Simultaneous Water Desalination and Hydrogen Gas Production," *Environmental Science Technlogy,* vol. 44, pp. 9578–9583, 2010.

[36] S. Cheng and B. E. Logan, "High hydrogen production rate of microbial electrolysis cell (MEC) with reduced electrode spacing," *Bioresource technology,* vol. 102, pp. 3571-4, Feb 2011.

[37] S. J. Sarma, S. K. Brar, E. B. Sydney, Y. Le Bihan, G. Buelna, and C. R. Soccol, "Microbial hydrogen production by bioconversion of crude glycerol: A review," *International Journal of Hydrogen Energy,* vol. 37, pp. 6473-6490, 2012.

[38] S. A. Campbell, *The science and engineering of microelectronic fabrication*: Oxford University Press, 2001.

[39] W. Whyte, *Cleanroom Technology: Fundamentals of design, testing and operation*: John Wiley & Sons, 2001.

[40] H. Xiao, *Introduction to Semiconductor Manufacturing Technology*: Prentice Hall, 2001.

[41] R. C. Jaeger, *Introduction to microelectronic fabrication* vol. V: Prentice Hall, 2002.

[42] R. Doering and Y. Nishi, *Handbook of Semiconductor Manufacturing Technology*: CRC Press, 2008.

[43] M. Madou, *Fundamentals of Microfabrication and Nanotechnology: Manufacturing Techniques for Microfabrication and Nanotechnology*, Third ed. vol. 2. Boca Raton: Taylor & Francis Group, 2012.

[44] M. J. Madou, *Fundamentals of Microfabrication: The Science of Miniaturization, Second Edition*, Second ed.: CRC Press, 2002.

[45] M. J. Hart and A. G. R. Evans, "Rapid thermal processing in semiconductor technology," *Semiconductor Science and Technology,* vol. 3, pp. 421-436, 1988.

[46] A. T. FIORY, "Recent Developments in Rapid Thermal Processing," *Journal of Electronic Materials,* vol. 31, pp. 981-987, 2002.

[47] Y. Lee, W. Oh, V. A. Dao, S. Q. Hussain, and J. Yi, "Ultrathin Oxide Passivation Layer by Rapid Thermal Oxidation for the Silicon Heterojunction Solar Cell Applications," *International Journal of Photoenergy,* vol. 2012, pp. 1-5, 2012.

[48] F. Roozeboom, "Rapid thermal processing systems: A review with emphasis on temperature control," *Journal of Vacuum Science & Technology B: Microelectronics and Nanometer Structures,* vol. 8, p. 1249, 1990.

[49] S. M. Rossnagel, J. J. Cuomo, and W. D. Westwood, *Handbook of Plasma Processing Technology. Fundamentals, Etching, Deposition and Surface Interactions* Noyes Publications, 1990.

[50] B. Wu, A. Kumar, and S. Pamarthy, "High aspect ratio silicon etch: A review," *Journal of applied physics,* vol. 108, pp. 1-20, 2010.

[51] K. Wasa and S. Hayakawa, *Handbook of Sputter Deposition Technology. Principles, Technology and Applications*: Noyes Publications, 1992.

[52] R. A. Power and S. M. Rossnagel, *PVD for Microelectronics: Sputter deposition applied to semiconductor manufacturing* vol. 26: Academic Press, 1999.

[53] M. Schlesinger and M. Paunovic, *Modern Electroplating*: Wiley, 2010.

[54] N. Kanani, *Electroplating: Basic Principles, Processes and Practice* Elsevier, 2005.

[55] M. Paunovic and M. Schlesinger, *Fundamentals of Electrochemical Deposition*: Wiley, 2006.

[56] J. W. Dini, *Electrodeposition: The Materials Science of Coatings and Substrates* William Andrew, 1994.

[57] K. A. Reinhardt and W. Kern, *Handbook of Silicon Wafer Cleaning Technology. Materials Science and Process Technology Series* William Andrew, 2008.

[58] G. Strang and G. Fix, *An Analysis of the Finite Element Method*: Wellesley-Cambridge, 2008.

[59] O. C. Zienkiewicz, R. L. Taylor, and J. Z. Zhu, *The Finite Element Method: Its Basis and Fundamentals*: Butterworth-Heinemann, 2005.

[60] J. Reddy, *An Introduction to the Finite Element Method* McGraw-Hill, 2005.

[61] R. W. Pryor, *Multiphysics modelling using COMSOL 4. A first principles approach*: Mercury learning and information, 2012.

[62] I. J. Cutress, E. J. F. Dickinson, and R. G. Compton, "Analysis of commercial general engineering finite element software in electrochemical simulations," *Journal of Electroanalytical Chemistry,* vol. 638, pp. 76-83, 2010.

[63] A. Gebhardt, *Rapid Prototyping*: Hanser Gardner, 2003.

[64] C. K. Chua, K. F. Leong, and C. S. Lim, *Rapid Prototyping: Principles and Applications*: World Scientific Publishing Company, 2010.

[65] F. W. Liou, *Rapid Prototyping and Engineering Applications: A Toolbox for Prototype Development* CRC Press, 2007.

[66] R. I. Noorani, *Rapid Prototyping: Principles and Applications*: Wiley, 2005.

[67] I. Gibson, D. W. Rosen, and B. Stucker, *Additive Manufacturing Technologies: Rapid Prototyping to Direct Digital Manufacturing*: Springer, 2009.

[68] M. Rahman, A. B. M. A. Asad, T. Masaki, T. Saleh, Y. S. Wong, and A. Senthil Kumar, "A multiprocess machine tool for compound micromachining," *International Journal of Machine Tools and Manufacture,* vol. 50, pp. 344-356, 2010.

[69] N. Zarif Karimi, H. Heidary, G. Minak, and M. Ahmadi, "Effect of the drilling process on the compression behavior of glass/epoxy laminates," *Composite Structures,* vol. 98, pp. 59-68, 2013.

[70] D. A. Bartholomeusz, R. W. Boutté, and J. D. Andrade, "Xurography: Rapid Prototyping of Microstructures Using a Cutting Plotter," *JOURNAL OF MICROELECTROMECHANICAL SYSTEMS,* vol. 14, pp. 1364-1374, 2005.

[71] M. Focke, D. Kosse, C. Muller, H. Reinecke, R. Zengerle, and F. von Stetten, "Lab-on-a-Foil: microfluidics on thin and flexible films," *Lab on a chip,* vol. 10, pp. 1365-86, Jun 7 2010.

[72] J. Do, J. Y. Zhang, and C. M. Klapperich, "Maskless writing of microfluidics: Rapid prototyping of 3D microfluidics using scratch on a polymer substrate," *Robotics and Computer-Integrated Manufacturing,* vol. 27, pp. 245-248, 2011.

[73] A. Overby, *CNC Machining Handbook. Building, programming and implementation*: Mc Graw Hill, 2011.

[74] D. Wilson, "GX-24 Cutter Blade Knowledge," ed, 2011, pp. 1-9.

[75] O. Ordeig, F. J. Del Campo, F. J. Munoz, C. E. Banks, and R. G. Compton, "Electroanalysis Utilising Amperometric Microdisc Electrode Arrays," *Electroanalysis,* vol. 19, pp. 1973-1986, 2007.

[76] D. W. M. Arrigan, "Nanoelectrodes, nanoelectrode arrays and their applications," *Analyst,* vol. 129, p. 1157, 2004.

[77] N. Godino, X. Borrisé, F. J. Munoz, F. J. Del Campo, and R. G. Compton, "Mass transport to nanoelectrode arrays and limitations of the diffusion domain approach: theory and experiment.," *The Journal of Physical Chemistry C,* vol. 113, pp. 11119-11125, 2009.

[78] S. G. Lemay, D. M. van den Broek, A. J. Storm, D. Krapf, R. M. M. Smeets, H. A. Heering, and C. Dekker, "Lithographically Fabricated Nanopore-Based Electrodes for Electrochemistry," *Analytical Chemistry,* vol. 77, pp. 1911-1915, Apr 2005.

[79] P. Sun and M. V. Mirkin, "Kinetics of Electron-Transfer Reactions at Nanoelectrodes," *Analytical Chemistry,* vol. 78, pp. 6526-6534, Sep 2006.

[80] C. G. Zoski, N. Yang, P. He, L. Berdondini, and M. Koudelka-Hep, "Addressable Nanoelectrode Membrane Arrays: Fabrication and Steady-State Behavior," *Analytical Chemistry,* vol. 79, pp. 1474-1484, Mar 2007.

[81] A. Arora, G. Simone, G. B. Salieb-Beugelaar, J. T. Kim, and A. Manz, "Latest Developments in Micro Total Analysis Systems," *Analytical Chemistry,* vol. 82, pp. 4830-4847, Jul 15 2010.

[82] J. P. Esquivel, M. Castellarnau, T. Senn, B. Löchel, J. Samitier, and N. Sabaté, "Fuel cell-powered microfluidic platform for lab-on-a-chip applications," *Lab on a chip,* vol. 12, pp. 74-79, 2012.

[83] N. Godino, F. J. d. Campo, F. X. Muñoz, M. F. Hansen, J. P. Kutter, and D. Snakenborg, "Integration of a zero dead-volume PDMS rotary switch valve in a miniaturised (bio)electroanalytical system," *Lab on a chip,* vol. 10, pp. 1841-1847, 2010.

[84] N. Godino, D. Snakenborg, J. P. Kutter, J. Emnéus, M. F. Hansen, F. X. Muñoz, and F. J. d. Campo, "Construction and characterisation of a modular microfluidic system:

coupling magnetic capture and electrochemical detection " *Microfluidics and Nanofluidics,* vol. 8, pp. 393-402, 2010.

[85] O. Ordeig, C. E. Banks, J. del Campo, F. X. Muñoz, and R. G. Compton, "Trace Detection of Mercury(II) Using Gold Ultra-Microelectrode Arrays," *Electroanalysis,* vol. 18, pp. 573-578, 2006.

[86] I. J. Cutress, E. J. F. Dickinson, and R. G. Compton, "Analysis of commercial general engineering finite element software in electrochemical simulations," *Journal of electroanalytical chemistry and interfacial electrochemistry,* vol. 638, pp. 76-83, Feb 01 2010.

[87] C. Amatore, J. SAVEANT, and D. Tessier, "Charge transfer at partially blocked surfaces:: A model for the case of microscopic active and inactive sites," *Journal of electroanalytical chemistry and interfacial electrochemistry,* vol. 147, pp. 39-51, 1983.

[88] T. J. Davies and R. G. Compton, "The cyclic and linear sweep voltammetry of regular and random arrays of microdisc electrodes: Theory," *Journal of Electroanalytical Chemistry,* vol. 585, pp. 63-82, 2005.

[89] I. Streeter, N. Fietkau, F. J. Del Campo, R. Mas, F. J. Munoz, and R. G. Compton, "Voltammetry at regularly interdigitated microband electrode arrays: Theory and experiment," *The Journal of Physical Chemistry C,* vol. 111, pp. 12058-12066, 2007.

[90] F. G. Chevallier, T. J. Davies, O. V. Klymenko, L. Jiang, T. G. J. Jones, and R. G. Compton, "Numerical simulation of partially blocked electrodes under cyclic voltammetry conditions: influence of the block unit geometry on the global electrochemical properties," *Journal of Electroanalytical Chemistry,* vol. 577, pp. 211-221, 2005.

[91] F. G. Chevallier, T. J. Davies, O. V. Klymenko, L. Jiang, T. G. J. Jones, and R. G. Compton, "Influence of the block geometry on the voltammetric response of partially blocked electrodes: Application to interfacial liquid–liquid kinetics of aqueous vitamin B12S with random arrays of femtolitre microdroplets of dibromocyclohexane," *Journal of Electroanalytical Chemistry,* vol. 580, pp. 265-274, 2005.

[92] D. Menshykaua, F. J. Del Campo, F. J. Munoz, and R. G. Compton, "Current collection efficiency of micro- and nano- ring-recessed disk electrodes and arrays of these electrodes," *Sensors and Actuators B: Chemical,* vol. 138, pp. 362-367, 2009.

[93] E. J. F. Dickinson, I. Streeter, and R. G. Compton, "Theory of Chronoamperometry at Cylindrical Microelectrodes and Their Arrays," *Journal of Physical Chemistry C,* vol. 112, pp. 11637-11644, Aug 07 2008.

[94] M. C. Henstridge and R. G. Compton, "Mass Transport to micro- and nanoelectrodes and their arrays: a review," *The Chemical Record,* vol. 12, pp. 63-71, Dec 06 2011.

[95] M. C. Henstridge, E. J. F. Dickinson, M. Aslanoglu, C. Batchelor-McAuley, and R. G. Compton, "Voltammetric selectivity conferred by the modification of electrodes using conductive porous layers or films: The oxidation of dopamine on glassy carbon

electrodes modified with multiwalled carbon nanotubes," *Sensors and Actuators B: Chemical,* vol. 145, pp. 417-427, Apr 04 2010.

[96] R. G. Compton, C. Batchelor-McAuley, and E. J. F. Dickinson, *Understanding Voltammetry: Problems and Solutions*. London: Imperial College Press, 2012.

[97] F. J. d. Campo, P. Godignon, L. Aldous, E. Pausas, M. Sarrión, M. Zabala, R. Prehn, and R. G. Compton, "Fabrication of PPF Electrodes by a Rapid Thermal Process," *Journal of The Electrochemical Society,* vol. 158, pp. H63-H68, 2011.

[98] M. J. González-Guerrero, J. P. Esquivel, D. Sánchez-Molas, P. Godignon, F. X. Muñoz, F. J. d. Campo, F. Giroud, S. D. Minteer, and N. Sabate, "Membraneless Glucose/O2 Microfluidic Enzymatic Biofuel Cells using Pyrolyzed Photoresist Film Electrodes " *Lab on a chip,* p. 10.1039/c3lc50319d, 2013.

[99] O. Ordeig, J. del Campo, F. X. Muñoz, C. E. Banks, and R. G. Compton, "Electroanalysis Utilizing Amperometric Microdisk Electrode Arrays," *Electroanalysis,* vol. 19, pp. 1973-1986, 2007.

[100] R. L. McCreery, "Advanced carbon electrode materials for molecular electrochemistry," *Chemical Reviews,* vol. 108, pp. 2646-2687, 2008.

[101] C. Fairman, S. S. C. Yu, G. Liu, A. J. Downard, D. B. Hibbert, and J. J. Gooding, "Exploration of variables in the fabrication of pyrolysed photoresist," *Journal of Solid State Electrochemistry,* vol. 12, pp. 1357-1365, 2008.

[102] É. N. Oiye, J. F. d. Andrade, V. R. Balbo, A. L. d. Santos, and M. F. d. Oliveira, "Development of an Alternative Route for Production of Glassy Polymeric Carbon Electrodes in Laboratorial Scale," presented at the Macromolecular Symposia, 2011.

[103] A. Lyons, C. Wilkins, and M. Robbins, "Thin pinhole-free carbon films," *Thin Solid Films,* vol. 103, pp. 333–341, 1983.

[104] A. M. Lyons, "Photodefinable carbon films electrical properties," *Journal of Non-Crystalline Solids,* pp. 99-109, 1985.

[105] A. M. Lyons, L. P. Hale, and C. W. W. Jr, "Photodefinable carbon films control of image quality," *Journal of Vacuum Science and Technology. B,* vol. 3, pp. 447-452, 1984.

[106] O. J. A. Schueller, S. T. Brittain, and G. M. Whitesides, "Fabrication of glassy carbon microstructures by pyrolysis of microfabricated polymeric precursors," *Advanced Materials,* vol. 9, pp. 477-480, 1997.

[107] O. J. A. Schueller, S. T. Brittain, and G. W. Whitesides, "Fabrication of glassy carbon microestructures by soft lithography," *Sensors and Actuators A: Physical,* vol. A72, pp. 125-139, 1999.

[108] J. Kim, X. Song, K. Kinoshita, M. Madou, and R. White, "Electrochemical studies of carbon films from pyrolyzed photoresist," *Journal of the Electrochemical Society,* vol. 145, pp. 2314-2319, 1998.

[109] J. I. Heo, D. S. Shim, G. T. Teixidor, S. Oh, M. J. Madou, and H. Shin, "Carbon Interdigitated Array Nanoelectrodes for Electrochemical Applications," *Carbon*

Interdigitated Array Nanoelectrodes for Electrochemical Applications, vol. 3, pp. J76-J80, 2011.

[110] S. Ranganathan and R. L. McCreery, "Electroanalytical performance of carbon films with near-atomic flatness," *Analytical Chemistry,* vol. 73, pp. 893-900, 2001.

[111] S. Ranganathan, R. McCreery, S. M. Majji, and M. Madou, "Photoresist-Derived Carbon for Microelectromechanical Systems and Electrochemical Applications," *Journal of the Electrochemical Society,* vol. 147, pp. 277-282, 2000.

[112] A. Akazawa, K. Okamoto, A. Syunori, and S. Konishi, "Various carbon composite pyrolyzed polymers and their electrical characterization," presented at the 7th IEEE International Conference on Nano/Micro Engineered and Molecular Systems(NEMS), 2012.

[113] C. Wang, L. Taherabadi, G. Jia, M. Madou, Y. Yeh, and B. Dunn, "C-MEMS for the manufacture of 3D microbatteries," *Electrochemical and Solid-State Letters,* vol. 7, 2004.

[114] E. D. Spoerke, R. Polsky, D. B. Burckel, D. R. Wheeler, and B. C. Bunker, "Rapid thermal pyrolysis of interferometrically patterned resist," *Carbon,* vol. 50, pp. 2894–2898., 2012.

[115] X. Xiao, T. E. Beechem, M. T. Brumbach, T. N. Lambert, D. J. Davis, J. R. Michael, C. M. Washburn, J. Wang, S. M. Brozik, D. R. Wheeler, D. B. Burckel, and R. Polsky, "Lithographically Defined Three-Dimensional Graphene Structures," *ACS Nano,* vol. 6, pp. 3573–3579, 2012.

[116] R. Kostecki, X. Song, and K. Kinoshita, "Fabrication of interdigitated carbon structures by laser pyrolysis of photoresist," *Electrochemical and Solid-State Letters,* vol. 5, 2002.

[117] R. Polsky, C. M. Washburn, G. Montano, H. Liu, T. L. Edwards, D. M. Lopez, J. C. Harper, S. M. Brozik, and D. R. Wheeler, "Reactive ion etching of gold-nanoparticle-modified pyrolyzed photoresist films," *Small,* vol. 5, pp. 2510-3, Nov 2009.

[118] J. I. Heo, D. S. Shim, G. T. Teixidor, S. Oh, M. J. Madou, and H. Shin, "Carbon Interdigitated Array Nanoelectrodes for Electrochemical Applications," *Journal of the Electrochemical Society,* vol. 158, p. J76, 2011.

[119] A. J. Gross and A. J. Downard, "Regeneration of pyrolyzed photoresist film by heat treatment," *Analytical Chemistry,* vol. 83, pp. 2397-402, Mar 15 2011.

[120] S. Park, P. Dong-Won, C.-S. Yang, K.-R. Kim, J.-H. Kwak, H.-M. So, C. W. Ahn, B. S. Kim, H. Chang, and J.-O. Lee, "Vertically Aligned Carbon Nanotube Electrodes Directly Grown on a Glassy Carbon Electrode," *ACS Nano,* vol. 5, pp. 7061–7068, 2011.

[121] WHO. http://www.who.int/water_sanitation_health/dwq/chemicals/mercury/en/.

[122] O. Abollino, A. Giacomino, M. Malandrino, G. Piscionieri, and E. Mentasti, "Determination of Mercury by Anodic Stripping Voltammetry with a Gold Nanoparticle-Modified Glassy Carbon Electrode," *Electroanalysis,* vol. 20, pp. 75-83, 2007.

[123] X. C. Fu, J. Wu, L. Nie, C. G. Xie, J. H. Liu, and X. J. Huang, "Electropolymerized surface ion imprinting films on a gold nanoparticles/single-wall carbon nanotube nanohybrids modified glassy carbon electrode for electrochemical detection of trace mercury(II) in water," *Analytica Chimica Acta,* vol. 720, pp. 29-37, 2012.

[124] T. Z. J. Gong, D. Song, L. Zhang, and X. Hu, "Stripping Voltammetric Detection of Mercury(II) Based on a Bimetallic Au−Pt Inorgani−Organic Hybrid Nanocomposite Modified Glassy Carbon Electrode," *Analytical Chemistry,* vol. 82, pp. 567-573, 2010.

[125] T. Hezard, K. Fajerwerg, D. Evrard, V. Colliere, P. Behra, and P. Gros, "Influence of the gold nanoparticles electrodeposition method on Hg(II) trace electrochemical detection," *Electrochim. Acta,* vol. 73, pp. 15-22, // 2012.

[126] J. Švarc-Gajić, Z. Suturović, N. Marjanović, and S. Kravić, "Determination of Mercury by Chronopotentiometric Stripping Analysis Using Glassy Carbon Vessel as a Working Electrode," *Electroanalysis,* vol. 18, pp. 513-516, 2006.

[127] J. Gong, T. Zhou, D. Song, and L. Zhang, "Monodispersed Au nanoparticles decorated graphene as an enhanced sensing platform for ultrasensitive stripping voltammetric detection of mercury(II)," *Sensors and Actuators B: Chemical,* vol. 150, pp. 491-497, 2010.

[128] . *United States Environmental Protection Agency (USEPA)* Available: http://www.epa.gov/osw/hazard/testmethods/sw846/pdfs/7472.pdf

[129] "Mathematical model for microbial fuel cells with anodic biofilms and anaerobic digestion."

[130] I. Streeter and R. G. Compton, "Numerical simulation of the limiting current for the CE mechanism at a microdisc electrode," *Journal of Electroanalytical Chemistry,* vol. 615, pp. 154-158, 2008.

[131] C. Wang and M. Madou, "From MEMS to NEMS with carbon," *Biosensors & bioelectronics,* vol. 20, pp. 2181-7, Apr 15 2005.

[132] G. He, Y. Gu, S. He, U. Schroder, S. Chen, and H. Hou, "Effect of fiber diameter on the behavior of biofilm and anodic performance of fiber electrodes in microbial fuel cells," *Bioresource technology,* vol. 102, pp. 10763-6, Nov 2011.

[133] X. Han, K. Malladi, W. Chunlei, and M. Madou, "Carbon microstructures for glucose biosensor," 2006, pp. 248-251.

[134] J. A. Lee, S. Hwang, J. Kwak, S. I. Park, S. S. Lee, and K.-C. Lee, "An electrochemical impedance biosensor with aptamer-modified pyrolyzed carbon electrode for label-free protein detection," *Sensors and Actuators B: Chemical,* vol. 129, pp. 372-379, 2008.

[135] A. Singh, J. Jayaram, M. Madou, and S. Akbar, "Pyrolysis of negative photoresists to fabricate carbon structures for microelectromechanical systems and electrochemical applications," *Journal of the Electrochemical Society,* vol. 149, 2002.

[136] H. Xu, K. Malladi, C. Wang, L. Kulinsky, M. Song, and M. Madou, "Carbon post-microarrays for glucose sensors," *Biosensors and Bioelectronics,* vol. 23, pp. 1637-1644, 2008.

[137] A. J. Downard, "Electrochemically assisted covalent modification of carbon electrodes," *Electroanalysis,* vol. 12, pp. 1085-1096, 2000.

[138] A. F. Ghenciu, "Review of fuel processing catalysts for hydrogen production in PEM fuel cell systems," *Current Opinion in Solid State and Materials Science,* vol. 6, pp. 389–399, 2002.

[139] H. P. BENNETT and J. L. STIRLING, "Anodic Reactions in Microbial Fuel Cells," *Biotechnology and Bioengineering,* vol. 25, pp. 559-568, 1983.

[140] B. E. Logan and J. M. Regan, "Electricity-producing bacterial communities in microbial fuel cells," *Trends in microbiology,* vol. 14, pp. 512-8, Dec 2006.

[141] S. B. Velasquez-Orta, I. M. Head, T. P. Curtis, K. Scott, J. R. Lloyd, and H. von Canstein, "The effect of flavin electron shuttles in microbial fuel cells current production," *Appl Microbiol Biotechnol,* vol. 85, pp. 1373-81, Feb 2010.

[142] K. C. Wrighton, J. C. Thrash, R. A. Melnyk, J. P. Bigi, K. G. Byrne-Bailey, J. P. Remis, D. Schichnes, M. Auer, C. J. Chang, and J. D. Coates, "Evidence for direct electron transfer by a gram-positive bacterium isolated from a microbial fuel cell," *Appl Environ Microbiol,* vol. 77, pp. 7633-9, Nov 2011.

[143] K. Nishio, R. Nakamura, X. Lin, T. Konno, K. Ishihara, S. Nakanishi, and K. Hashimoto, "Extracellular Electron Transfer across Bacterial Cell Membranes via a Cytocompatible Redox-Active Polymer," *ChemPhysChem,* Apr 29 2013.

[144] B. Min, J. Kim, S. Oh, J. M. Regan, and B. E. Logan, "Electricity generation from swine wastewater using microbial fuel cells," *Water research,* vol. 39, pp. 4961-8, Dec 2005.

[145] K. Rabaey and W. Verstraete, "Microbial fuel cells: novel biotechnology for energy generation," *Trends Biotechnol,* vol. 23, pp. 291-8, Jun 2005.

[146] B. E. LOGAN and J. M. REGAN, "Microbial Challenges and Fuel Cells - Applications," *Environmental Science & Te chnology,* pp. 5172-5180, 2006.

[147] D. Davila, J. P. Esquivel, N. Sabate, and J. Mas, "Silicon-based microfabricated microbial fuel cell toxicity sensor," *Biosensors & bioelectronics,* vol. 26, pp. 2426-30, Jan 15 2011.

[148] A. Han, H. Hou, L. Li, H. S. Kim, and P. de Figueiredo, "Microfabricated devices in microbial bioenergy sciences," *Trends Biotechnol,* vol. 31, pp. 225-32, Apr 2013.

[149] J. Yang, S. Ghobadian, P. J. Goodrich, R. Montazami, and N. Hashemi, "Miniaturized biological and electrochemical fuel cells: challenges and applications," *Phys Chem Chem Phys,* Mar 18 2013.

[150] O. Lefebvre, Z. Tan, Y. Shen, and H. Y. Ng, "Optimization of a microbial fuel cell for wastewater treatment using recycled scrap metals as a cost-effective cathode material," *Bioresource technology,* vol. 127, pp. 158-64, Jan 2013.

[151] H. L. I. U, S. GROT, and B. E. LOGAN, "Electrochemically Assisted Microbial Production of Hydrogen from Acetate," *Environmental Science & Te chnology,* vol. 39, pp. 4317-4320, 2005.

[152] D. Dávila, J. P. Esquivel, N. Vigués, O. Sánchez, L. Garrido, N. Tomás, N. Sabaté, F. J. d. Campo, F. J. Muñoz, and J. Mas, "Development and Optimization of Microbial Fuel Cells," *Journal of New Materials for Electrochemical Systems,* vol. 11, pp. 99-103, 2008.

[153] H. Y. Wang, A. Bernarda, C. Y. Huang, D. J. Lee, and J. S. Chang, "Micro-sized microbial fuel cell: a mini-review," *Bioresource technology,* vol. 102, pp. 235-43, Jan 2011.

[154] Y. FAN, E. HARBROUGH, and H. LIU, "Quantification of the Internal Resistance Distribution of Microbial Fuel Cells," *Environmental Science Technlogy,* vol. 42, pp. 8101-8107, 2008.

[155] S. Chen, G. He, Q. Liu, F. Harnisch, Y. Zhou, Y. Chen, M. Hanif, S. Wang, X. Peng, H. Hou, and U. Schröder, "Layered corrugated electrode macrostructures boost microbial bioelectrocatalysis," *Energy & Environmental Science,* vol. 5, p. 9769, 2012.

[156] Y. Liu, H. Kim, R. Franklin, and D. R. Bond, "Gold line array electrodes increase substrate affinity and current density of electricity-producing G. sulfurreducens biofilms," *Energy & Environmental Science,* vol. 3, p. 1782, 2010.

[157] J. Wei, P. Liang, and X. Huang, "Recent progress in electrodes for microbial fuel cells," *Bioresource technology,* vol. 102, pp. 9335-44, Oct 2011.

[158] J. R. KIM, S. CHENG, S.-E. OH, and B. E. LOGAN, "Power Generation Using Different Cation, Anion, and Ultrafiltration Membranes in Microbial Fuel Cells," *Energy & Environmental Science,* vol. 41, pp. 1004-1009, 2007.

[159] E. Mahendiravarman and D. Sangeetha, "Increased microbial fuel cell performance using quaternized poly ether ether ketone anionic membrane electrolyte for electricity generation," *International Journal of Hydrogen Energy,* vol. 38, pp. 2471-2479, 2013.

[160] B. E. Logan, "Scaling up microbial fuel cells and other bioelectrochemical systems," *Appl Microbiol Biotechnol,* vol. 85, pp. 1665-71, Feb 2010.

[161] H. Ren, H.-S. Lee, and J. Chae, "Miniaturizing microbial fuel cells for potential portable power sources: promises and challenges," *Microfluidics and Nanofluidics,* 2012.

[162] K. Aoki and J. Osteryoung, "Diffusion-controlled current at the stationary finite disk electrode," *Journal of Electroanalytical Chemistry,* pp. 19--35, 1981.

[163] B. A. Brookes, D. J. Gavaghan, and R. G. Compton, "Microring Electrodes: A Computational Study of Transport-Limited Processes," *The Journal of Physical Chemistry B,* pp. 4886-4896, 2002.

[164] F. G. Chevallier, N. Fietkau, J. del Campo, R. Mas, F. X. Muñoz, L. Jiang, T. G. J. Jones, and R. G. Compton, "Experimental cyclic voltammetry at partially blocked electrodes: Elevated cylindrical blocks," *Journal of Electroanalytical Chemistry,* vol. 596, pp. 25-32, 2006.

[165] E. Dickinson, I. Streeter, and R. Compton, "Theory of chronoamperometry at cylindrical microelectrodes and their arrays," *Journal Of Physical Chemistry C,* vol. 112, pp. 11637-11644, 2008.

[166] M. Fleischman and S. Pons, "The behaviour of microdisk and microring electrodes," *Journal of Electroanalytical Chemistry,* pp. 107-115, 1987.

[167] O. Ordeig, C. E. Banks, T. J. Davies, J. del Campo, R. Mas, F. X. Munoz, and R. G. Compton, "Regular arrays of microdisc electrodes: simulation quantifies the fraction of 'dead' electrodes," *Analyst,* vol. 131, pp. 440-445, 2006.

[168] D. Britz, O. Østerby, and J. Strutwolf, "Reference values of the chronoamperometric response at cylindrical and capped cylindrical electrodes," *Electrochimica Acta,* vol. 55, pp. 5629-5635, 2010.

[169] D. Sánchez-Molas, J. P. Esquivel, N. Sabaté, F. X. Muñoz, and F. J. del Campo, "High Aspect-Ratio, Fully Conducting Gold Micropillar Array Electrodes: Silicon Micromachining and Electrochemical Characterization," in *The Journal of Physical Chemistry C*, ed, 2012.

[170] I. Streeter, N. Fietkau, J. d. Campo, R. Mas, F. X. Muñoz, and R. G. Compton, "Voltammetry at Regular Microband Electrode Arrays: Theory and Experiment," *The Journal of Physical Chemistry C,* pp. 12058-12066, 2007.

[171] R. Prehn, L. Abad, D. Sánchez-Molas, M. Duch, N. Sabaté, F. J. del Campo, F. X. Muñoz, and R. G. Compton, "Microfabrication and characterization of cylinder micropillar array electrodes," *Journal of Electroanalytical Chemistry,* vol. 662, pp. 361-370, 2011.

[172] P. Abgrall, V. Conedera, H. Camon, A. M. Gue, and N. T. Nguyen, "SU-8 as a structural material for labs-on-chips and microelectromechanical systems," *Electrophoresis,* vol. 28, pp. 4539-51, Dec 2007.

[173] P. Abgrall and A. M. Gué, "Lab-on-chip technologies: making a microfluidic network and coupling it into a complete microsystem—a review," *Journal of Micromechanics and Microengineering,* vol. 17, pp. R15-R49, 2007.

[174] A. A. Bhagat, P. Jothimuthu, and I. Papautsky, "Photodefinable polydimethylsiloxane (PDMS) for rapid lab-on-a-chip prototyping," *Lab on a chip,* vol. 7, pp. 1192-7, Sep 2007.

[175] H. Yu, O. Balogun, B. Li, T. W. Murray, and X. Zhang, "Fabrication of three-dimensional microstructures based on singled-layered SU-8 for lab-on-chip applications," *Sensors and Actuators A: Physical,* vol. 127, pp. 228-234, 2006.

[176] K. E. Herold and A. Rasooly, *Lab-on-a-chip technology: Biomolecular separation and analysis* vol. 2: Caister Academy Press, 2009.

[177] P. J. Kitson, M. H. Rosnes, V. Sans, V. Dragone, and L. Cronin, "Configurable 3D-Printed millifluidic and microfluidic 'lab on a chip' reactionware devices," *Lab on a chip,* vol. 12, pp. 3267-3271, 2012.

[178] V. Dragone, V. Sans, M. H. Rosnes, P. J. Kitson, and L. Cronin, "3D-printed devices for continuous-flow organic chemistry," *Journal of Organic Chemistry,* vol. 9, pp. 951-959, 2013.

[179] K. B. Anderson, S. Y. Lockwood, R. S. Martin, and D. M. Spence, "A 3D Printed Fluidic Device that Enables Integrated Features," *Analytical chemistry,* vol. 85, pp. 5622-5626, 2103.

[180] H. Hou, L. Li, C. Ü. Ceylan, A. Haynes, J. Cope, H. H. Wilkinson, C. Erbay, P. d. Figueiredo, and A. Han, "A microfluidic microbial fuel cell array that supports long-term multiplexed analyses of electricigens.," *Lab on a chip,* vol. 12, pp. 4151-4159, 2012.

[181] W. Guo, Y. Pi, H. Song, W. Tang, and J. Sun, "Layer-by-layer assembled gold nanoparticles modified anode and its application in microbial fuel cells," *Colloids and Surfaces A: Physicochemical and Engineering Aspects,* vol. 415, pp. 105-111, 2012.

[182] Y. P. Chen, Y. Zhao, K. Q. Qiu, J. Chu, R. Lu, M. Sun, X. W. Liu, G. P. Sheng, H. Q. Yu, J. Chen, W. J. Li, G. Liu, Y. C. Tian, and Y. Xiong, "An innovative miniature microbial fuel cell fabricated using photolithography," *Biosensors & bioelectronics,* vol. 26, pp. 2841-6, Feb 15 2011.

[183] S. Choi, H. S. Lee, Y. Yang, P. Parameswaran, C. I. Torres, B. E. Rittmann, and J. Chae, "A μL-scale micromachined microbial fuel cell having high power density," *Lab on a chip,* vol. 11, pp. 1110-7, Mar 21 2011.

[184] M. Sun, F. Zhang, Z.-H. Tong, G.-P. Sheng, Y.-Z. Chen, Y. Zhao, Y.-P. Chen, S.-Y. Zhou, G. Liu, Y.-C. Tian, and H.-Q. Yu, "A gold-sputtered carbon paper as an anode for improved electricity generation from a microbial fuel cell inoculated with Shewanella oneidensis MR-1," *Biosensors & bioelectronics,* vol. 26, pp. 338-343, 2010.

[185] B. R. RINGEISEN, E. HENDERSON, P. K. WU, J. PIETRON, R. RAY, B. LITTLE, J. C. BIFFINGER, and J. M. J.-. MEEHAN, "High Power Density from a Miniature Microbial Fuel Cell Using Shewanella oneidensis DSP10," *Environmental Science Technlogy,* vol. 40, pp. 2629-2634, 2006.

[186] S. E. Oh, J. R. Kim, J. H. Joo, and B. E. Logan, "Effects of applied voltages and dissolved oxygen on sustained power generation by microbial fuel cells," *Water science and research,* vol. 5, pp. 1311-1317, 2009.

[187] A. Abbaspour and M. A. Kamyabi, "Electrochemical formation of Prussian blue films with a single ferricyanide solution on gold electrode," *Journal of Electroanalytical Chemistry,* vol. 584, pp. 117-123, 2005.

[188] C. Yang, C.-H. Wang, J.-S. Wu, and X. Xia, "Mechanism investigation of Prussian blue electrochemically deposited from a solution containing single component of ferricyanide," *Electrochimica Acta,* vol. 51, pp. 4019-4023, 2006.

[189] D. Zhang, K. Wang, D. Sun, X. Xia, and H. Chen, "Potentiodynamic deposition of Prussian blue from a solution containing single component of ferricyanide and its mechanism investigation," *Journal of Solid State Electrochemistry,* vol. 7, pp. 561-566, 2003.

[190] M. C. Henstridge, E. J. F. Dickinson, and R. G. Compton, "Mass Transport to and within Porous Electrodes. Linear Sweep Voltammetry and the Effects of Pore Size: The Prediction of Double Peaks for a Single Electrode Process," *Russian Journal of Electrochemistry,* vol. 48, pp. 629-635, 2012.

[191] K. Venkateswaran, D. P. Moser, M. E. Dollhopf, D. P. Lies, D. A. Saffarini, B. J. MacGregor, D. B. Ringelberg, D. C. White, M. Nishijima, H. Sano, J. Burghardt, E. Stackebrandt, and K. H. Nealson, "Polyphasic taxonomy of the genus Shewanella and description of Shewanella oneidensis sp. now," *International Journal of Systematic Bacteriology,* pp. 705-724, 1999.

[192] K. Fricke, F. Harnisch, and U. Schröder, "On the use of cyclic voltammetry for the study of anodic electron transfer in microbial fuel cells," *Energy & Environmental Science* pp. 144-147, 2008.